

Experimental Investigation and Numerical Modeling of Fiber Reinforced Concrete Beams for Different Failure Modes

Submitted to the Graduate School of Natural and Applied Sciences
in partial fulfillment of the requirements for the degree of

Master of Science

in Civil Engineering

by

Marwan AL SAMAN

ORCID 0000-0002-2536-5140

Thesis Advisor: Assist Prof. Dr. Mehmet Alper ÇANKAYA

July 2023

This is to certify that we have read the thesis **Experimental Investigation and Numerical Modeling of Fiber Reinforced Concrete Beams for Different Failure Modes** submitted by **Marwan AL SAMAN**, and it has been judged to be successful, in scope and in quality, at the defense exam and accepted by our jury as a MASTER'S THESIS.

APPROVED BY:

Advisor: **Assist. Prof. Dr. M. Alper ÇANKAYA**
İzmir Kâtip Çelebi University

Committee Members:

Assoc. Prof. Dr. Mutlu SEÇER
İzmir Kâtip Çelebi University

Assist. Prof. Dr. Selçuk SAATCI
Izmir Institute of Technology

Date of Defense: July 10, 2023

Declaration of Authorship

I, **Marwan AL SAMAN**, declare that this thesis titled **Experimental Investigation and Numerical Modeling of Fiber Reinforced Concrete Beams for Different Failure Modes** and the work presented in it are my own. I confirm that:

- This work was done wholly or mainly while in candidature for the Master's degree at this university.
- Where any part of this thesis has previously been submitted for a degree or any other qualification at this university or any other institution, this has been clearly stated.
- Where I have consulted the published work of others, this is always clearly attributed.
- Where I have quoted from the work of others, the source is always given. This thesis is entirely my own work, with the exception of such quotations.
- I have acknowledged all major sources of assistance.
- Where the thesis is based on work done by myself jointly with others, I have made clear exactly what was done by others and what I have contributed myself.

Date: 10.07.2023

Experimental Investigation and Numerical Modeling of Fiber Reinforced Concrete Beams for Different Failure Modes

Abstract

This study mainly aims to assess the efficiency of implementation of Concrete Damaged Plasticity model and Modified Compression Field Theory formulations into the nonlinear finite element method. The investigation was carried out on two groups of beams in order to cover a wide range of geometry, amount of steel fibers used, concrete strength, and tensile reinforcement ratio. Beams of the first group were taken from the literature and the second group beams were designed, constructed, and tested at the İzmir Katip Çelebi University Structural Mechanics Laboratory. Basically, the groups were separated considering the behavior being either critical in flexure or shear. The first group consisted of five beam specimens, three including steel fibers and two w/o fibers. This group was designed to fail from flexure. On the other hand, the second group of beams were designed to fail from brittle shear when did not contain fiber or stirrups. An investigation and analyze was made on the load-deflection behavior, ductility and crack patterns for the conducted experimental and numerical work. According to the findings, the CDP model and MCFT formulations were generally capable of determining of the behavior of the beams critical in flexure while MCFT formulations provided limited accuracy to capture the shear-critical beam behavior.

Keywords: Damage-Plasticity model, MCFT formulations, Nonlinear Finite Element Analysis, Steel Fiber Reinforced Concrete Beams, Bending, Shear and Flexure Critic Designs

Farklı Göçme Modlarına Sahip Lifli Betonarme Kirişlerin Deneysel İncelenmesi ve Sayısal Modellenmesi

ÖZ

Bu çalışma temel olarak, Beton Plastikleşme Hasar modelinin (ing. Concrete Damaged Plasticity CDP) ve Değiştirilmiş Basınç Alanları Teorisi (ing. Modified Compression Field Theory, MCFT) formülasyonlarının doğrusal olmayan sonlu elemanlar yöntemine uygulanmasının etkinliğini değerlendirmeyi amaçlamaktadır. Farklı boyutlar, kullanılan çelik lif miktarı, beton dayanımı ve çekme donatısı oranı gibi geniş ölçekli değişkenleri kapsayan iki kiriş grubu üzerinde incelemeler gerçekleştirilmiştir. Birinci grup kirişler literatürden alınmış, ikinci grup kirişler ise İzmir Katip Çelebi Üniversitesi Yapı Mekaniği Laboratuvarında tasarlanmış, imal ve test edilmiştir. Temel olarak gruplar, kirişlerin eğilmede veya kesmede kritik davranışa yol açacak tasarımlara sahip olmasına göre ayrılmıştır. Birinci grup, üçü çelik lifli ve ikisi lifsiz olmak üzere beş kiriş numunesinden oluşmuştur. Bu grup eğilmeye bağlı bir göçme tipine neden olacak şekilde tasarlanmıştır. İkinci grup kirişler ise, lif veya etriye içermediklerinde gevrek kesmeden kırılacak şekilde tasarlanmıştır. Yapılan deneysel ve sayısal çalışmalar yük-deplasman davranışı, süneklik ve hasar durumları bağlamında incelenmiş ve değerlendirilmiştir. Elde edilen sonuçlara göre, CDP modeli ve MCFT formülasyonu genel olarak eğilmede kritik kirişlerin davranışını belirlemede başarılı olurken, MCFT formülasyonu kesmede kritik olan kiriş davranışını yakalamada yeterli başarıyı gösterememiştir.

Anahtar Kelimeler: Beton plastikleşme hasar modeli, Değiştirilmiş basınç alanları teorisi, Doğrusal olmayan sonlu elemanlar analizi, Eğilme, Çelik lifli betonarme kiriş, Kesme ve eğilme kritik tasarım

Acknowledgment

This study was financially assisted by the Scientific Research Division of İzmir Katip Çelebi University with the grant number of 2023-TYL-FEBE-0001. I would like to express my deepest gratitude for the support provided. In addition, I also would like to express my gratitude to the Civil Engineering Department of İzmir Katip Çelebi University (IKCU), the thesis study could not turn into reality without its laboratory infrastructure.

I would like to acknowledge and give my warmest thanks to my supervisor Dr. M. Alper ÇANKAYA who made this work possible with his knowledge and guidance. I owe my thanks to the thesis defense committee members Dr. Mutlu SEÇER and Dr. Selçuk SAATCI for their brilliant comments and suggestions.

Lastly, I would like to give my special thanks to my family who have given me the opportunity of an education abroad and support throughout my life.

Table of Contents

Declaration of Authorship.....	ii
Abstract.....	iii
Öz	iv
Acknowledgment	v
List of Figures	x
List of Tables	xiii
List of Abbreviations	xiv
1 Introduction	1
1.1 General.....	1
1.2 Literature Review.....	3
1.3 Objective and Scope	9
1.4 Organization.....	10
2 Finite Element Modelling.....	11
2.1 Introduction.....	11
2.2 Numerical Methods.....	11
2.2.1 The Modified Compression Field Theory (MCTF).....	11
2.2.1.1 Assumptions	12
2.2.1.2 The Relationships of Compatibility	12
2.2.1.3 Equilibrium Conditions	14
2.2.1.4 Constitutive Relations	15
2.2.2 Concrete Damaged Plasticity (CDP) Model.....	17
2.2.2.1 Compressive behavior	18

2.2.2.2	Tension Stiffening	19
2.2.2.2.1	Post-failure stress-strain relationships	19
2.2.2.2.2	Fracture energy cracking criterion	20
2.2.2.3	Concrete plasticity	21
2.2.2.3.1	Yield Function	22
2.3	Development of Finite Element Model in VecTor2	24
2.4	Development of Finite Element Model in ABAQUS	26
2.4.1	Reinforced Concrete Beams	26
2.4.2	Modeling the Compressive Response of Concrete.....	27
2.4.2.1	Concrete in the Selected Study.....	27
2.4.2.2	Concrete in the Conducted Laboratory Work	28
2.4.3	Modeling the Tensile Response of Concrete.....	31
2.4.4	Support and Load Plates	33
2.4.5	Steel reinforcement rebars	34
3	Validation of FE model on Flexure Critic Beams Using Literature	37
3.1	Introduction.....	37
3.2	Preparation of Test Specimens.....	37
3.3.	Experiments	39
3.4	Results and Discussion	40
3.4.1	Predicted Response using Plasticity Analysis (ABAQUS)	40
3.4.1.1	Parametric Study	40
3.4.1.1.1	Contact Type.....	40
3.4.1.1.2	Tension Stiffening Models.....	42
3.4.1.1.3	Mesh Sensitivity.....	43
3.4.1.2	Load-Deflection Relationship	45
3.4.1.3	Crack pattern	49
3.4.1.4	Ductility.....	51

3.4.2	Predicted Response using MCTF Analysis (VecTor2)	52
3.4.2.1	Load-Deflection Relationship	52
3.4.2.2	Crack pattern	56
3.4.2.3	Ductility	57
3.4.3	Comparison of Results.....	58
3.4.3.1	Load-Deflection Relationship	58
4	Validation of FE models on Shear Critic Beams: An Experimental Work ..	62
4.1	Introduction.....	62
4.2	The Experimental Setup.....	62
4.3	Production of Test Specimens	63
4.4	Materials	64
4.5	Results and Discussion	66
4.5.1	Experimental Load-Deflection Relationship	66
4.5.2	Predicted Response Using Plasticity Analysis (ABAQUS)	67
4.5.2.1	Load-Deflection Relationship	67
4.5.2.2	Crack Patterns.....	70
4.5.2.3	Ductility.....	71
4.5.3	Predicted Response Using MCTF Analysis (VecTor2)	72
4.5.3.1	Load-Deflection Relationship	72
4.5.3.2	Crack Patterns.....	75
4.5.3.3	Ductility.....	77
4.5.4	Comparison of Results.....	77
4.5.4.1	Load-Deflection Relationship	77
5	Conclusion.....	80
	References	82
	Appendices	87

Appendix A Tabularization of Numerically Calculated and Experimentally Obtained Load, Deflection and Error Data	88
Appendix B Technical Specification of Data Acquisition Device and Instrumentations	93
Appendix C Reinforcement Preparation, Concrete Pouring and Material Testing Photos from the Conducted Experimental Study	99
Curriculum Vitae	103

List of Figures

Figure 1.1	(a) Failure modes and crack patterns of concrete slab without fiber (b) and with fiber [4].....	1
Figure 1.2	The crack pattern of beam specimens without fiber (a) and with fiber (b) [4]	2
Figure 1.3	The experimental load-displacement relationships with C30 class of concrete [10].....	2
Figure 1.4	Load-displacement response of concrete beams with and without fibers [12]	3
Figure 1.5	The load-displacement curves of experimental and numerical study [13]	5
Figure 1.6	Procedure for placing the UHPC [18]	7
Figure 2.1	Average concrete strains due to average stress-strain response of concrete [25]	13
Figure 2.2	Mohr's circle for average strains [23]	13
Figure 2.3	Free body diagram of reinforced concrete element [25]	14
Figure 2.4	Mohr's circle for average concrete stresses [23].....	15
Figure 2.5	Compressive stress-inelastic strain curve [28]	18
Figure 2.6	Cracking strain used for definition of tension stiffening data [28]	20
Figure 2.7	Post-failure stress versus displacement curve [28].....	20
Figure 2.8	Yield surfaces in the deviatoric plane showing various K_c values [28]	23
Figure 2.9	Yield surface in plane stress [28]	23
Figure 2.10	FE model of (a) reinforced concrete beam with stirrups (b) and fibrous concrete without stirrups	26
Figure 2.11	(Left) Solid element with reduced integration point, (Right) 3D Solid concrete beam part.....	27
Figure 2.12	Compression behavior of plain concrete (taken from [15])	28
Figure 2.13	Compression behavior of concrete with fiber (taken from [15])	28

Figure 2.14 Analytically calculated compressive behavior of confined plain concrete	29
Figure 2.15 Analytically calculated compression behavior of fibrous concrete.....	30
Figure 2.16 Calculated tensile behavior of plain concrete using [35]	32
Figure 2.17 Calculated tensile response of concrete with hooked-end fibers using [21]	33
Figure 2.18 The FE model of the beam with two loading plates at top.....	34
Figure 2.19 (a) 3D two node linear beam elements, (b) and steel reinforcement part	35
Figure 2.20 (a) The true and engineering model of steel reinforcements with a yield strength of 490 MPa, (b) and true plastic stress-strain curve	36
Figure 3.1 Specimen geometry and reinforcement details [15].....	38
Figure 3.2 Four point bending structural test set up [15].....	40
Figure 3.3 Comparison of load-deflection response of small SFRC beam with different contact types	41
Figure 3.4 Calculated tensile behavior of fibrous concrete using SDEM and FIB Model Code 2010	42
Figure 3.5 Comparison of load-deflection response of small SFRC beam with different tension stiffening models.....	43
Figure 3.6 Comparison of load-deflection response of small SFRC beam with different mesh sizes	44
Figure 3.7 Load-mid span deflection curve for S-SF	46
Figure 3.8 Load-mid span deflection curve for M-SF	47
Figure 3.9 Load-mid span deflection curve for L-SF	47
Figure 3.10 Load-mid span deflection curve for S-N.....	48
Figure 3.11 Load-mid span deflection curve for L-N.....	48
Figure 3.12 The top view of the small beam illustrates the concrete crushes at the outermost layer	49
Figure 3.13 Cracking patterns at failure	50
Figure 3.14 Load-mid span deflection curve for S-SF beam.....	53
Figure 3.15 Load-mid span deflection curve for M-SF beam	54
Figure 3.16 Load-mid span deflection curve for L-SF beam	54
Figure 3.17 Load-mid span deflection curve for S-N.....	55

Figure 3.18	Load-mid span deflection curve for L-N beam.....	55
Figure 3.19	Cracking patterns at failure	56
Figure 3.20	Comparison of Load-mid span deflection curves for S-SF.....	59
Figure 3.21	Comparison of Load-mid span deflection curves for M-SF.....	59
Figure 3.22	Comparison of Load-mid span deflection curves for L-SF.....	60
Figure 3.23	Comparison of Load-mid span deflection curves for S-N	60
Figure 3.24	Comparison of Load-mid span deflection curves for L-N	61
Figure 4.1	Beam specimen and the sensors ready for test.....	63
Figure 4.2	Detailing of B1, B2, B3 and B4 beams	64
Figure 4.3	The load-displacement curve of the beam samples.....	66
Figure 4.4	Load-displacement curve of B1 specimen	68
Figure 4.5	Load-displacement curve of B2 specimen	68
Figure 4.6	Load-displacement curve of B3 specimen	69
Figure 4.7	Load-displacement curve of B4 specimen	69
Figure 4.8	Experimentally obtained crack patterns and numerically captured damages.....	70
Figure 4.9	Load-displacement curve of specimen B1	73
Figure 4.10	Load-displacement curve of specimen B2	73
Figure 4.11	Load-displacement curve of specimen B3	74
Figure 4.12	Load-displacement curve of specimen B4	74
Figure 4.13	Experimentally and numerically obtained crack patterns of plain and fibrous concrete beams.....	75
Figure 4.14	Comparison of Load-mid span deflection curves for B1	78
Figure 4.15	Comparison of Load-mid span deflection curves for B2	78
Figure 4.16	Comparison of Load-mid span deflection curves for B3	79
Figure 4.17	Comparison of Load-mid span deflection curves for B4	79

List of Tables

Table 2.1	The Parameters of Plasticity	24
Table 2.2	The models used to define the response of plain and fibrous concrete.	25
Table 2.3	The models were used to define the response of steel reinforcement ...	25
Table 2.4	The average crack spacing of fibrous beam specimens	25
Table 3.1	Dimensions of test specimens	38
Table 3.2	The details and properties of steel reinforcing	39
Table 3.3	Properties of hooked steel fibers	39
Table 3.4	The effect of contact type on the FE analysis results	41
Table 3.5	The computed fracture energies	43
Table 3.6	The effect of mesh size on the result of the SFRC beam	44
Table 3.7	Ductility Indices of the HSC and SFRC beams	52
Table 3.8	Ductility Indices of the HSC and SFRC beams	58
Table 4.1	The average compressive and tensile strength of concrete used in beams	65
Table 4.2	The types of fiber additives used in the beams	65
Table 4.3	Experimental and numerical ductility Indices of the beams	72
Table 4.4	Calculated ductility indices of the beams.....	77

List of Abbreviations

ACI	American Concrete Institute
CDP	Concrete Damaged Plasticity
CFT	Compression Field Theory
DEM	Diverse Embedment Model
FE	Finite Element
FRC	Fiber Reinforced Concrete
HSC	High Strength Concrete
LPT	Linear Position Transducer
MCTF	Modified Compression Field Theory
NLFE	Non-Linear Finite Element
PP	Polypropylene
RC	Reinforced Concrete
SDEM	Simplified Diverse Embedment Model
SFRC	Steel Fiber Reinforced Concrete
TBEC	Turkish Building Earthquake Code
UHPC	Ultra High-Performance Concrete
UHPRC	Ultra High-Performance Fiber Reinforced Concrete
UTM	Universal Testing Machine

Chapter 1

Introduction

1.1 General

In the last 50 years fiber reinforced concrete has been used in a variety of non-structural members such as industrial floor slabs and concrete pavements. A steel fiber is a reinforcing element which have a discrete and discontinued property [1]. Usage of steel fibers in concrete mixtures started more than 40 years ago. This material basically provides bridging mechanism between the cracks on the concrete [2] which is shifting the response from quasi-brittle to ductile [3] by sustaining the tensile loads [4] in the post cracking region. Moreover, it also increased the number of cracks [5], [6] (Figure 1.1), provided a resistance to crack propagation [4] (Figure 1.2), and reduced the crack spacing and width [4], [5], [6], [7], [8], [9]. Consequently, the cracking behavior is improved.

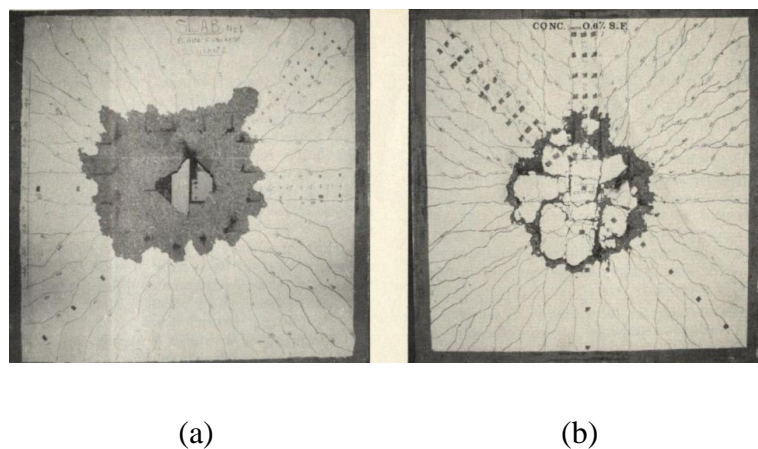
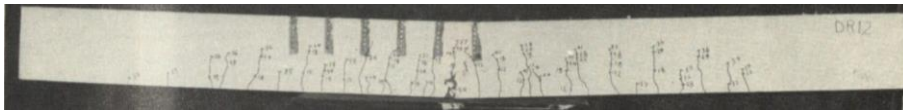


Figure 1.1: (a) Failure modes and crack patterns of concrete slab without fiber (b) and with fiber [4]



(a)



(b)

Figure 1.2: The crack pattern of beam specimens without fiber (a) and with fiber (b) [4]

In the literature, the load carrying capacity was reported to be increased by 12 to 23% for various volumetric ratios of steel fiber additive [6] and the fibrous concrete exhibited an improvement in flexural toughness (energy absorption capacity) depending on increased deflection capacity [10], [11] as illustrated in Figure 1.3.

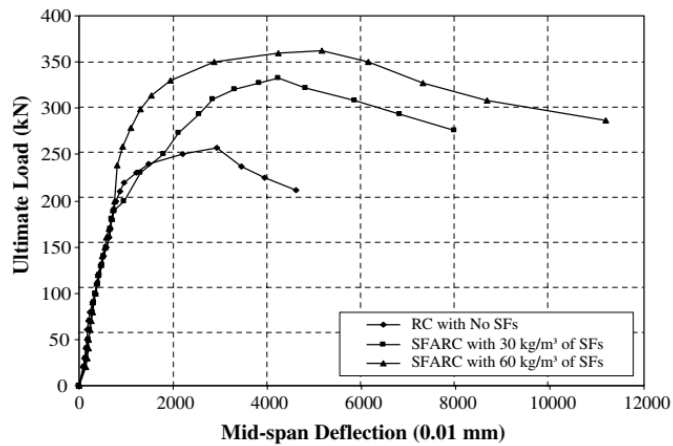


Figure 1.3: The experimental load-displacement relationships with C30 class of concrete [10]

1.2 Literature Review

Numerous experimental and numerical studies have been undertaken to examine the flexural performance of steel fiber reinforced concrete in the literature. A summary of notable studies conducted in this area is provided below:

Çankaya and Akan (2023) [12] conducted both experimental and numerical investigations to observe how the inclusion of steel and PP fibers affects the bending behavior of RC beam elements. They produced eight RC beam specimens divided into two groups and subjected them to three-point bending tests with monotonically increasing loads. The beams were designed to have different tensile reinforcement ratios (0.86% and 1.30%), resulting in either flexural or shear critical sections. Among the specimens, three were selected as control samples without any fibers, while the remaining specimens included varying volumes (0%, 0.5%, and 1.0%) of steel or PP fibers. The experimental findings revealed that the existence of 0.5% fibers in densely reinforced beams enhanced shear strength and allowed the full utilization of flexural capacity. Whereas usage of 1% fiber increased the load carrying capacity by 10% as illustrated in Figure 1.4. The existence of PP fiber caused an increase in ductility as against steel fibers. Afterwards, once the experimental study was completed, the numerical study followed using nonlinear finite element method based on the modified compression field theory. The prediction of load-deflection response of steel fiber was in good agreement compared to the experimental response/results.

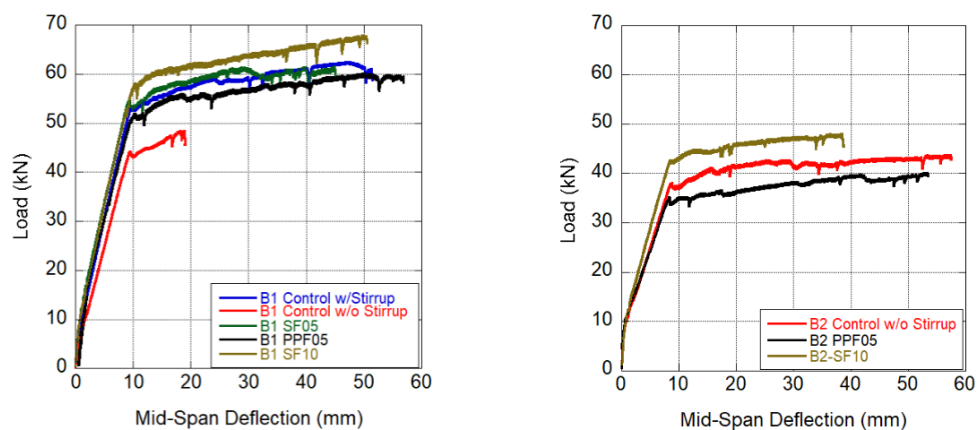


Figure 1.4: Load-displacement response of concrete beams with and without fibers [12]

Singh et al. (2017) [13] conducted a comprehensive study, combining experimental and numerical approaches, to examine the flexural behavior of beams made of ultra-high-performance fiber reinforced concrete (UHPFRC). The study involved testing four large-scale beams with varying cross sections and spans under both four- and three-point bending. The concrete used had a compressive strength of 140 MPa and a tensile strength of 5.8 MPa. To enhance the properties of the concrete, steel fibers were added with a volumetric fraction of 2.25% and an aspect ratio of 64. In the numerical analysis, the researchers utilized the ABAQUS non-linear finite element code and incorporated the concrete damaged plasticity (CDP) model to simulate the material behavior of UHPFRC in the finite element analysis. Material tests were conducted on the UHPFRC to determine its properties, which were essential inputs for the CDP model. The numerical results were then validated against the findings from the experimental study. In the numerical model, the concrete was represented using eight-node reduced integration brick elements (C3D8R), while the reinforcements were simulated using three-dimensional truss elements (T3D2) with only axial deformation. The support and loading plates were modeled using eight-node brick elements (C3DR). The beam and support were modeled as surface-to-surface contact with a frictional coefficient of 0.1. The influence of mesh size was evaluated, and based on the mesh sensitivity analysis, an element size of 25 mm was taken. The experimental results demonstrated that all beam failures were attributed to the rupture of tensile reinforcement. The inclusion of long fibers enhanced the post-peak behavior. The numerical study using the CDP model accurately predicted the load carrying capacity and moment capacity of the ultra-high-performance fiber reinforced concrete beams, as depicted in Figure 1.5. Furthermore, the load-displacement response exhibited good agreement with the experimental data.

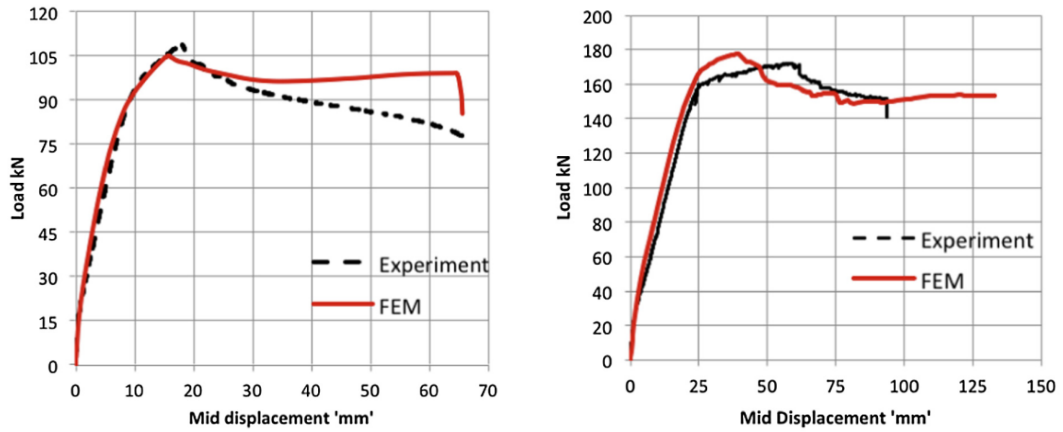


Figure 1.5: The load-displacement curves of experimental and numerical study [13]

Earij et al. (2017) [14] conducted a numerical parametric study on two reinforced concrete beams selected from an experimental study for capturing an accurate load-deflection response. For this purpose, three-dimensional models were created and analyzed by using explicit-dynamic time integration method in ABAQUS non-linear finite element software. The beams were subjected to cyclic four-point bending and the variables were (1) effect of mesh size, (2) element types for rebars and concrete material, (3) dilation angel, (4) tension softening model and (5) analyze type such as linear and non-linear. Based on the obtained results all listed variables had effects on the RC beam member response in terms of load-deflection curve and crack patterns.

Yoo et al. (2017) [15] performed an experimental and numerical study on five large scale reinforced concrete beams. The beams were subjected to four-point bending to investigate the feasibility of replacing the minimum shear reinforcement by 0.75% of hooked end steel fibers having an aspect ratio of 65. There were three sets of beams categorized as small, medium, and large with respect to cross sectional dimensions and length. Three of the beams had steel fibers without stirrups and the rest were reinforced concrete beam with minimum stirrups and without fibers. The compressive strength of concrete with and without fiber was 72 and 67 MPa respectively. The tensile reinforcement ratios were 0.64% and 0.72%. Results have shown that the presence of 0.75% of end hooked steel fiber capable to eliminate the minimum shear reinforcement and shift the failure mode from concrete crushing to steel bar rupture. The SFRC beams with no stirrup had higher flexural strength than the beams having stirrup w/o fibers.

However, SFRC beams had lower ultimate deflection and ductility capacity. The authors concluded that the using of steel fiber rather than stirrups on-site is not an easy work due to the difficulty in attaining quality control or assurance of steel fiber reinforced concrete.

Yo and Yoon (2015) [16] performed an experimental and numerical study to investigate the flexural behavior of 10 reinforced UHPC beams with different type of steel fibers and different ratios of tensile reinforcement under four-point bending. The loads were applied monotonically. The tensile reinforcement ratios were 0.94% and 1.50%. The concrete compressive strength was detected to be 200.9 MPa to 232.1 MPa. The used fibers were two types as smooth steel fiber with various lengths (13, 19.5, 30 mm) and twisted steel fiber with 30 mm length. Steel fibers aspect ratio varied between 65 to 100 for smooth and 100 for twisted fibers. Based on the results, existence of steel fibers slightly reduced the load corresponding to first cracking and deflection due to inhomogeneous fiber dispersion. However, post-cracking stiffness and load carrying capacity were enhanced remarkably in case of having fibers. This was explained by bridging of cracks by the fibers. On the other hand, increase in length of smooth steel fibers and presence of twisted fibers ended up with increase in post-peak response and ductility. Finally, due to crack localization phenomenon the beams with fibers performed a lower ductility index than that of the ones without fibers.

Meda et al. (2012) [17] tested seven RC beams under four-point bending for investigating the contribution of steel fiber to the flexural behavior. The volume fractions of hook ended steel fiber were 0.38% and 0.76% (30 and 60 kg/m³) with aspect ratio of 50, and the tensile strength of steel fiber was 1100 MPa. The ratios of tensile reinforcement were 0.75% and 1.5% with yield stress 534 MPa and ultimate strength of 630 MPa. The compressive strength of plain concrete was 49.7 MPa. According to obtained results, the presence of steel fiber shifted the failure pattern from concrete crushing to steel rupture. In addition, as the volumetric fiber ratio increased the ductility decreased depending on the strain concentrations in the steel rebars. However, addition of fibers to the reinforced concrete improved the load bearing capacity under flexure and this enhancement relied on the ratio of fiber reinforced concrete toughness to tensile reinforcement ratio, and this ratio heavily affects the overall ductility.

Yang et al. (2010) [18] investigated flexural behavior of 14 ultra-high-performance concrete (UHPC) RC beams under four-point bending. UHPC included 2% steel fibers by volume and effects of UHPC placing or casting method and steel rebar ratios were examined. The beams had various tensile reinforcement ratios as 0.6%, 0.9%, 1.2%, 1.31% and 1.96%. The compressive stresses of steel fiber reinforced concrete were in the range of 190.9 and 196.7 MPa, and the maximum equivalent tensile stresses were between 29.3 and 32.7 MPa. In the study two techniques were used to place the UHPC. Firstly, each beam -except for two specimens- was casted from one end of the mold and allowed to flow to the other end as shown in Figure 1.6. In the second approach, the UHPC was poured from the middle of the form and allowed to flow to both ends. The results showed that UHPC has the capacity to redistribute stresses and exposed to multiple cracks before fiber pullout. On the other hand, flexural capacity or the ultimate load was also noted to be affected from the casting method of UHPC. The beams having identical rebar ratio and cross-sectional dimensions but casted through the first technique exhibit 15% higher capacity than that of the beams casted by second approach. Finally, the steel fiber reinforced UHPC of used in the study performed effective ductile behavior owing to the yielding of rebar until flexural failure for the beams having low rebar ratios (<1.2%).

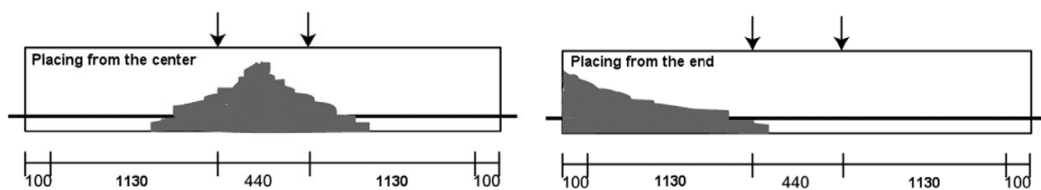


Figure 1.6: Procedure for placing the UHPC [18]

Ashour et al. (2000) [19] performed an experimental study to investigate the flexural behavior of twenty-seven reinforced concrete beams that were subjected to four-point bending load. For this purpose, the effect of reinforcement ratio, steel fiber content and compressive strength of concrete on the flexural behavior of reinforced concrete beams were assessed as variables. The compressive strength of concrete was detected to be 49, 79, and 102 MPa. The steel fiber contents were 0.0%, 0.5%, and 1%, and the

tensile reinforcement ratios were 1.18%, 1.77% and 2.37%. The results have shown the cracking, yielding, and ultimate moment capacities were enhanced as the fiber content increased. Furthermore, an increment in the steel fiber content and the concrete compressive strength yielded to increase in the flexural rigidity. Finally, the fiber improved the cracking pattern by reducing the width of cracks and increasing the number of cracks. Moreover, it increased the ductility and delayed the final crushing of concrete. The fibers had a remarkable enhancement in the ductility and post-cracking stiffness for all the tested beams.

Constitutive Models

Some of the constitutive models developed for determination of steel fiber reinforced concrete response under tension and compression is summarized as follows:

Lee et al. (2011) [20] proposed the Diverse Embedment Model (DEM) as a predictive tool in describing the tensile behavior of concrete having straight and hooked end steel fibers. The model incorporates the randomness of fiber embedment length and inclination angle, and accounts for the asymmetric anchorage of hooked end fibers in the constitutive relationship. It also takes into account the pullout characteristics of the fibers, including frictional bond behavior and mechanical anchorage. Verification studies have proven the effectiveness and accuracy of this model in predicting the relationship between tensile stress and crack width during uniaxial tension tests of specimens containing straight or hooked end steel fibers.

Lee et al. (2013) [21] introduced a simplified version of the Diverse Embedment Model (DEM) to eliminate the requirement for double numerical integration. This simplified model which is known as the Simplified Diverse Embedment Model (SDEM), was derived from the DEM by omitting the elongation of fibers and the variation of slip along the fiber. In addition, the model assumes that the slip on the shorter embedded side is equal to the crack width, while the slip on the longer embedded side is disregarded. Despite these simplifications, the authors reported that the SDEM provides an accurate representation of the direct tensile or flexural behavior of steel fiber reinforced concrete (SFRC) members with both straight and hooked end fibers. The necessary parameters to establish this model are (1) fiber length, (2)

distance between mechanical anchorages for hooked end fibers, (3) fiber volumetric ratio and aspect ratio and (4) the concrete compressive and cracking strength.

Lee et al. (2015) [22] proposed a model that defines the stress-strain behavior of concrete material with hooked end steel fibers under compression. This model was developed through uniaxial compression tests. The experimental results revealed that the steel fiber reinforced concrete (SFRC) samples exhibited ductile behavior beyond the peak strength. An increase in both fiber volumetric ratio and aspect ratio led to an enhancement of the strain at compressive strength. However, it was observed that the elastic modulus decreased. The parameters required for the model to be employed include (1) fiber volumetric ratio, (2) fiber aspect ratio, and (3) concrete compressive strength.

1.3 Objective and Scope

The main objective of this study is to investigate the effectiveness of NLFE method on the bending behavior of SFRC beams using MCFT formulations and CDP model. This was accomplished through validation work which involved comparison of experimental outputs to the results obtained from the NLFE approach.

This attempt was undertaken not only on beams prone to flexure failure, but also on beams with shear critical designs. For this purpose, an experimental study investigating the steel fiber additive effects on the bending behavior of flexure critically designed reinforced concrete beams with ultra-high strength concrete, was taken from the literature. Other than that, four additional large-scale beam specimens were produced and tested at the Structural Mechanics Laboratory of İzmir Katip Çelebi University. The beams were designed to be critical in shear and three out of four had hooked end steel fiber additive while the remaining one was conventionally reinforced with stirrups.

1.4 Organization

Chapter 1: Introduction

General information about the usage of steel fiber additive in structural engineering applications and aim and the scope are expressed. Also, a brief literature review on the experimental and numerical studies of fibrously reinforced concrete beams bending behavior is presented.

Chapter 2: Finite Element Modeling

Chapter starts with explaining the theoretical backgrounds of MCFT and CDP and followed by construction of numerical models using VecTor2 and ABAQUS software. The constitutive models defining the response of materials such as plain and fibrous concrete and steel are also discussed in this chapter.

Chapter 3: Validation of FE model on Flexure Critic Beams Using Literature

This chapter summarizes the selected experimental investigation from the literature. The obtained numerical analysis results were presented by a validation process with those of experimental.

Chapter 4: Validation of FE model on Shear Critic Beams: An Experimental Work

Details of the carried out experimental study were given. These included the reinforcement details, mechanical and physical properties of materials and the test setup. Finally, identical to Chapter 3, a validation process was performed using the numerically and experimentally obtained data.

Chapter 5: Conclusions

Findings of the conducted numerical and experimental study were presented.

Chapter 2

Finite Element Modelling

2.1 Introduction

In this chapter, the numerical models of two groups steel fiber reinforced concrete beams were established. The first group beams were taken from the study conducted by [15] in which they were designed to be critical in flexure and subjected to four-point bending. The second group beams, on the other hand, were critical in shear and constructed in the Structural Mechanics Laboratory of İzmir Katip Çelebi University.

After construction of numerical models, the FE analyses were completed utilizing MCFT formulations and a plasticity-based continuum damage model through commercially available two and three-dimensional nonlinear finite element codes VecTor2 and ABAQUS. They were based on static/implicit and dynamic/explicit solution methods, respectively. Geometric non-linearity was taken into account in both types of analyses. Details about the modeling approaches are presented under the following titles.

2.2 Numerical Methods

2.2.1 The Modified Compression Field Theory (MCTF)

Modified Compression Field Theory (MCFT) [23] is a theoretical framework developed for the analysis and design of reinforced concrete structures. It is an extension of the original Compression Field Theory (CFT) proposed by [24] in 1974, which explains the behavior of reinforced concrete under compression. MCFT provides a more accurate and comprehensive way of predicting the behavior of

reinforced concrete structures under various loading conditions. MCFT uses a smeared rotating crack approach for modelling cracked concrete.

2.2.1.1 Assumptions

The MCFT uses the following assumptions for deriving the formulations of element: (1) the reinforcement is distributed uniformly, (2) the cracks are uniformly distributed and rotating, (3) shear and normal stresses are applied uniformly, (4) the reinforcement and concrete are perfectly bonded, (5) the shear stresses in reinforcement are neglected, (6) the constitutive models of concrete and reinforcement are independent from each other.

These assumptions allow MCFT to predict the behavior of reinforced concrete structures with reasonable accuracy under a wide range of loading conditions. However, it is important to note that the accuracy of the model may be affected if the assumptions are not met in practice. Therefore, it is important to apply MCFT with caution and verify the results with experimental data.

2.2.1.2 The Relationships of Compatibility

The relationships of compatibility relate to the average strain components of the concrete and reinforcement as illustrated in Figure 2.1. Assuming a perfect bond between concrete and reinforcement, that meaning the concrete experiences similar average strains as reinforcement does, as given in Equations (2.1), (2.2).

$$\epsilon_x = \epsilon_{cx} = \epsilon_{sx} \quad (2.1)$$

$$\epsilon_y = \epsilon_{cy} = \epsilon_{sy} \quad (2.2)$$

The strain in any direction can be calculated if the strain components ϵ_x , ϵ_y , and γ_{xy} are available as shown in Figure 2.1.

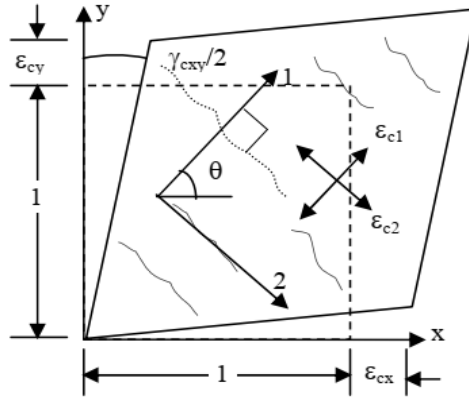


Figure 2.1: Average concrete strains due to average stress-strain response of concrete [25]

In the Figure 2.1, (ϵ_{c1}) is the average principal concrete tensile strain that is perpendicular to the cracks, (ϵ_{c2}) is the average principle concrete compressive strain that is parallel to cracks and (θ_c) is the principal strain direction. These parameters can be determined using the Mohr's circle of strain that shown in Figure 2.2 using Equations (2.3), (2.4), and (2.5).

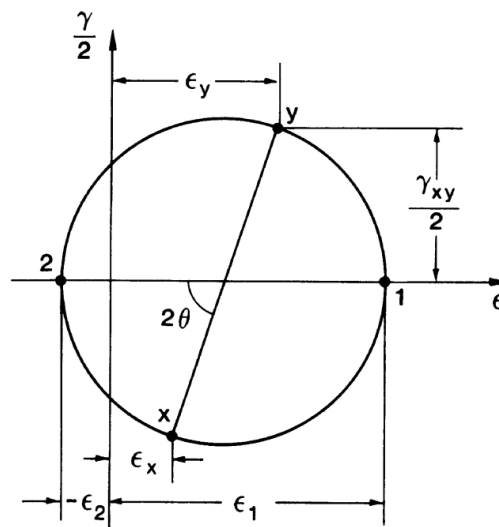


Figure 2.2: Mohr's circle for average strains [23]

$$\varepsilon_1 = \frac{(\varepsilon_x + \varepsilon_y)}{2} + \frac{1}{2} [(\varepsilon_y - \varepsilon_x)^2 + \gamma_{xy}^2]^{\frac{1}{2}} \quad (2.3)$$

$$\varepsilon_2 = \frac{(\varepsilon_x + \varepsilon_y)}{2} - \frac{1}{2} [(\varepsilon_y - \varepsilon_x)^2 + \gamma_{xy}^2]^{\frac{1}{2}} \quad (2.4)$$

$$\theta_c = \frac{1}{2} \tan^{-1} \left[\frac{\gamma_{xy}}{\varepsilon_x - \varepsilon_y} \right] \quad (2.5)$$

2.2.1.3 Equilibrium Conditions

The equilibrium equations can be obtained considering the free body diagram given in Figure 2.3 and are expressed by the Equations (2.6), (2.7) and (2.8). Additionally, Mohr's circle of stress, Figure 2.4, can be utilized to relate the average concrete stresses (f_{cx} and f_{cy}) and the average principal concrete tensile (f_{c1}) and compression stresses (f_{c2}). The relations are presented by Equations (2.9), and (2.10).

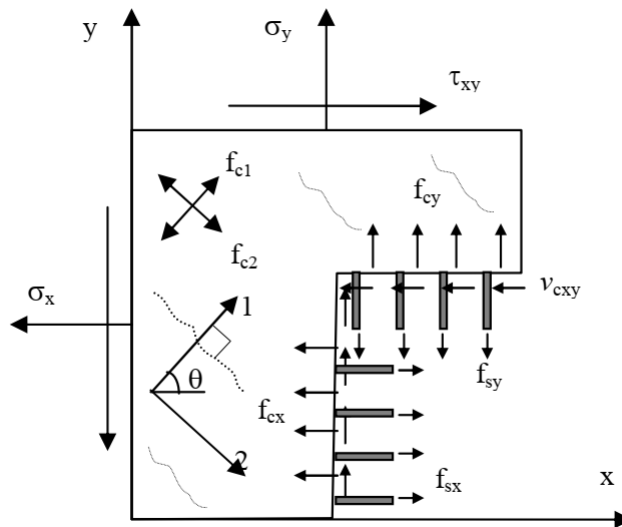


Figure 2.3: Free body diagram of reinforced concrete element [25]

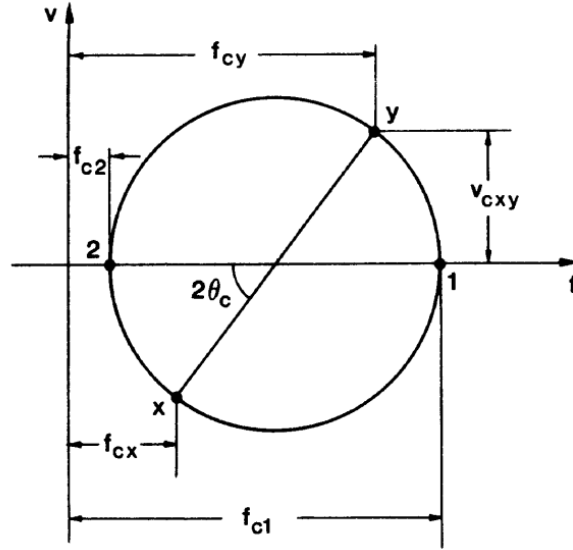


Figure 2.4: Mohr's circle for average concrete stresses [23]

$$\sigma_x = f_{cx} + \rho_{sx}f_{sx} \quad (2.6)$$

$$\sigma_y = f_{cy} + \rho_{sy}f_{sy} \quad (2.7)$$

$$\tau_{xy} = v_{cxy} \quad (2.8)$$

$$f_{cx} = f_{c1} - \frac{v_{cxy}}{\tan\theta_c} \quad (2.9)$$

$$f_{cy} = f_{c1} - v_{cxy} \cdot \tan\theta_c \quad (2.10)$$

2.2.1.4 Constitutive Relations

Constitutive relationships have a crucial role in establishing the correlation between average stresses and average strains for both concrete and reinforcement. The principal compressive stress in concrete (f_{c2}) can be determined as a function of the principal compressive strain (ε_2) and principal tensile strain ε_1 . The suggested function for this relationship, as proposed by [23], is presented in Equation (2.11), where f_{c2max} represents the maximum principal compressive stress as in Equation (2.12).

Additionally, (ε'_c) denotes the concrete strain corresponding to the peak stress (f'_c) , and generally equal to 0.002.

$$f_{c2} = f_{c2max} \left[2 \left(\frac{\varepsilon_2}{\varepsilon'_c} \right) - \left(\frac{\varepsilon_2}{\varepsilon'_c} \right)^2 \right] \quad (2.11)$$

$$f_{c2max} = \frac{f'_c}{0.8 - 0.34 \frac{\varepsilon_1}{\varepsilon'_c}} \quad (2.12)$$

The principal tensile stress in the concrete (f_{c1}) is a function relates to the principal tensile strain (ε_{c1}). To determine this function, it is required to find the uniaxial cracking strength (f'_t) and the cracking strain (ε_{cr}). When this value is not available it is can be estimated from Equations (2.13) and (2.14):

$$f'_t = 0.33 \sqrt{f'_c} \quad (2.13)$$

$$\varepsilon_{cr} = \frac{f'_t}{E_c} \quad (2.14)$$

Where E_c is the concrete elastic modulus (found from the slope of initial tangent line) and can be calculated using Equation (2.15):

$$E_c = 5000 \sqrt{f'_c} \quad (2.15)$$

The concrete exhibits linear-elastic behavior before cracking in tension and principal tensile stress is calculated as Equation (2.16):

$$f_{c1} = E_c \cdot \varepsilon_{c1} \text{ for } 0 < \varepsilon_{c1} < \varepsilon_{cr} \quad (2.16)$$

Tensile stresses may exist even after cracking of concrete due to the perfect bond between reinforcement and concrete. This phenomenon is known as tension stiffening and the proposed relationship by the MCFT is as given in Equation (2.17):

$$f_{c1} = \frac{f'_t}{1 + \sqrt{200 \varepsilon_{c1}}} \quad (2.17)$$

The MCFT utilizes average stress-strain to model a bilinear relationship of the reinforcement in compression and tension. The initial portion behaves linear elastic until yield stress, as Equation (2.18):

$$f_s = E_s \cdot \varepsilon_s \leq f_{s\text{yield}} \quad (2.18)$$

2.2.2 Concrete Damaged Plasticity (CDP) Model

This plasticity-based continuum damage model follows a non-associated plastic flow rule and employs the yield function proposed by [26] which was later revised by [27]. In CDP model, the material behavior is controlled not only by plasticity but also the two major failure mechanisms as tension cracking and compression crushing, Figure 2.5 and Figure 2.6 [28]. These failure mechanisms described by strain softening branch of material and result in isotropic (scalar) stiffness degradation or damage “ d ”.

The degraded stiffness (E) is presented by Equation (2.19) where d is the damage parameter which is ranging from 0 (undamaged) to 1 (fully damaged), and E_0 is the undamaged elastic stiffness.

$$E = (1 - d)E_0 \quad (2.19)$$

In the current study, d was defined based on the relatively simple damage model proposed by [26]. According to model, degradation occurs only in the softening region and can be specified for tension and compression as shown in Equation (2.20) [29], [30].

$$d = 1 - \sigma/f \quad (2.20)$$

In the Equation, f is either tensile or compressive strength of concrete material and σ is the current stress level.

2.2.2.1 Compressive Behavior

Under uniaxial compression the curve of stress-strain is linear elastic until the value of initial yield. In the plastic zone the behavior is presented by stress hardening followed by strain softening after the maximum stress and the compressive response is given by Equation (2.21).

$$\sigma_c = E_0(1 - d_c)(\varepsilon_c - \varepsilon_c^{pl}) \quad (2.21)$$

In the Equation, ε_c and ε_c^{pl} stands for total compressive strain and equivalent plastic strain which is automatically calculated by ABAQUS using equation (2.22) in which ε_c^{in} is inelastic strain. The inelastic strain is specified by extracting the elastic strain from the total strain as Equation (2.23), and the elastic strain is calculated by Equation (2.24).

$$\varepsilon_c^{pl} = \varepsilon_c^{in} - \frac{d_c}{(1 - d_c)} \frac{\sigma_c}{E_0} \quad (2.22)$$

$$\varepsilon_c^{in} = \varepsilon_c - \varepsilon_{0c}^{el} \quad (2.23)$$

$$\varepsilon_{0c}^{el} = \sigma_c / E_0 \quad (2.24)$$

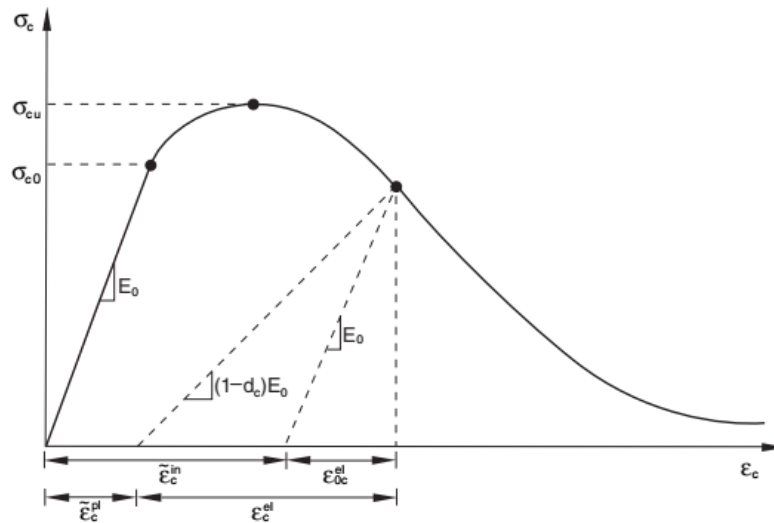


Figure 2.5: Compressive stress-inelastic strain curve [28]

2.2.2.2 Tension Stiffening

Uniaxial tension response is linear elastic until the value of cracking strength (failure stress). Once the strength is being reached softening in stress-strain response will be activated depending on the emerging of cracks. Behavior is governed by Equation (2.25).

$$\sigma_t = E_0(1 - d_t)(\varepsilon_t - \varepsilon_t^{pl}) \quad (2.25)$$

The post-failure is modeled considering the tension stiffening which allows determination of the strain-softening behavior for cracked concrete. It can be specified using either a fracture energy cracking criterion or post-failure stress-strain relation. Determination of tension stiffening is important in capturing the accurate results.

2.2.2.2.1 Post-failure stress-strain relationships

The behavior in the post-failure region is determined by the relation between the post-failure stress and cracking strain. The cracking strain (ε_t^{ck}) is detected by extracting the elastic strain from the total strain as given in Equation (2.26). The elastic strain stands for the virgin material and can be computed by the Equation (2.27). ABAQUS converts the cracking strain into the plastic strain (ε_t^{pl}) using Equation (2.28). In here, it should be noted that the plastic strain should not be take any negative values and/or decrease with increasing cracking strain since it will lead to error in the analysis.

$$\varepsilon_t^{ck} = \varepsilon_t - \varepsilon_{0t}^{el} \quad (2.26)$$

$$\varepsilon_{0t}^{el} = \frac{\sigma_t}{E_0} \quad (2.27)$$

$$\varepsilon_t^{pl} = \varepsilon_t^{ck} - \frac{d_t}{(1 - d_t)} \frac{\sigma_t}{E_0} \quad (2.28)$$

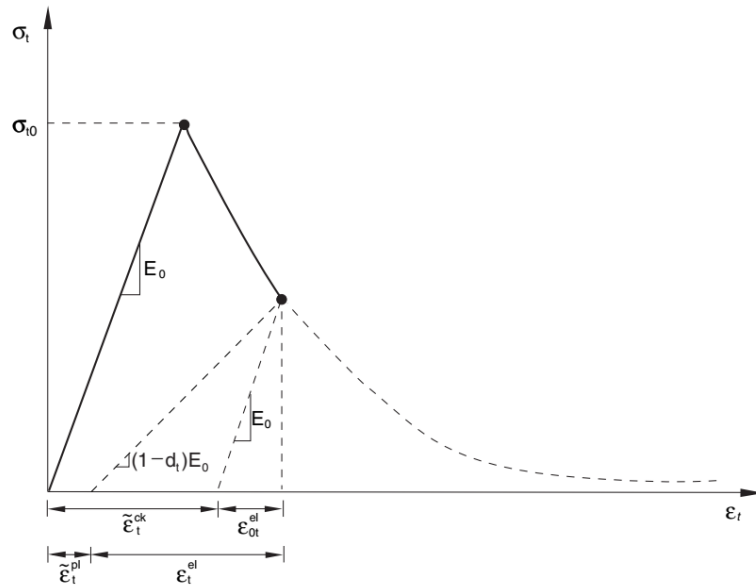


Figure 2.6: Cracking strain used for definition of tension stiffening data [28]

2.2.2.2.2 Fracture energy cracking criterion

Hillerborg (1976) [31] introduced the fracture energy (G_F) as a material parameter and expressed it as the energy required to create a unit area of crack. In this approach, the response of concrete is determined by using the stress-displacement response instead of the stress-strain response. The fracture energy cracking model can be generated by tabularization of the post-failure stress versus cracking displacement as illustrated in Figure 2.7.

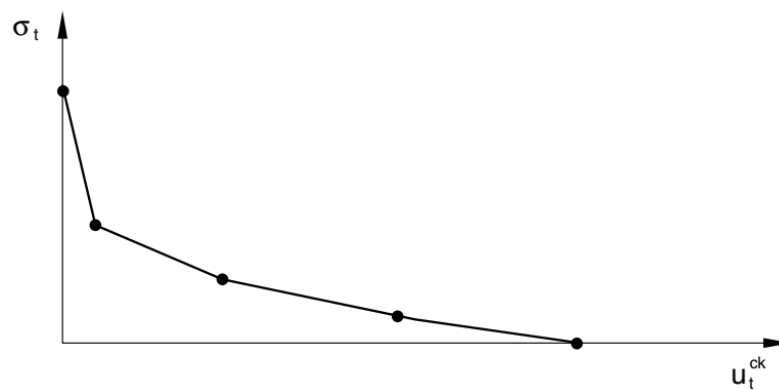


Figure 2.7: Post-failure stress versus displacement curve [28]

ABAQUS automatically acquires the plastic displacement (u_t^{pl}) through the cracking displacement (u_t^{cr}) as given in Equation (2.29) where l_0 is the sample length and assumed to be one unit length $l_0 = 1$.

$$u_t^{pl} = u_t^{cr} - \frac{d_t}{(1 - d_t)} \frac{\sigma_t l_0}{E_0} \quad (2.29)$$

In the current study, the fracture energy cracking criterion method was adopted.

2.2.2.3 Concrete plasticity

The non-associated plastic flow rule described below is employed in the CDP model by Equation (2.30):

$$\dot{\epsilon}_p = \lambda \frac{\partial G}{\partial \sigma} \quad (2.30)$$

Where σ and $\dot{\epsilon}_p$ refer to the stress and plastic strain rate tensors, respectively, λ is plastic multiplier, and flow potential G is the Drucker-Prager hyperbolic function given in Equation (2.31).

$$G = \sqrt{(\epsilon \sigma_{t0} \tan \psi)^2 + \bar{q}^2} - \bar{p} \cdot \tan \psi \quad (2.31)$$

\bar{p} and \bar{q} are the hydrostatic pressure stress and the Mises equivalent effective stress as expressed in Equation (2.32) and (2.33) respectively. ψ is the dilation angle measured at high confining pressure in the \bar{p} - \bar{q} plane. In the current study the dilation angle is selected as 35 degrees based on the sensitivity analysis. σ_{t0} is the uniaxial tensile stress at failure. ϵ is a parameter, referred to the eccentricity, which defines the rate at which the function approaches the asymptote. The default value of the eccentricity is 0.1 and was taken in the current study. When the value of flow potential eccentricity is significantly smaller than the default value, it might cause convergence problems.

$$\bar{p} = -\frac{1}{3}\text{trace}(\bar{\sigma}) \quad (2.32)$$

$$\bar{q} = \sqrt{\frac{3}{2}\|\text{dev}(\bar{\sigma})\|} \quad (2.33)$$

In Equation (2.32 and 2.33), $\bar{\sigma}$ is the effective stress calculated from Equation (2.34) where D_0^{el} is the initial elasticity matrix.

$$\bar{\sigma} = D_0^{el}:(\varepsilon - \varepsilon^{pl}) \quad (2.34)$$

2.2.2.3.1 Yield Function

The CDP model uses the yield function proposed by [26] with the revision suggested by [27] to account for the various loading cases causing different strength behavior under compression and tension. The development of the yield surface is controlled by the hardening variables $\tilde{\varepsilon}_t^{pl}$ and $\tilde{\varepsilon}_c^{pl}$. The yield function takes the form as given in Equation (2.35) in terms of effective stress with α , β and γ parameters which is presented by Equation (2.36), (2.37) and (2.38).

$$F = \frac{1}{1-\alpha}\left(\bar{q} - 3\alpha\bar{p} + \beta(\tilde{\varepsilon}^{pl})(\hat{\sigma}_{max}) - \gamma(-\hat{\sigma}_{max})\right) - \bar{\sigma}_c(\tilde{\varepsilon}_c^{pl}) = 0 \quad (2.35)$$

$$\alpha = \left(\left(\frac{\sigma_{b0}}{\sigma_{c0}}\right) - 1\right) / \left(2\left(\frac{\sigma_{b0}}{\sigma_{c0}}\right) - 1\right), 0 \leq \alpha \leq 0.5 \quad (2.36)$$

$$\beta = \frac{\bar{\sigma}_c(\tilde{\varepsilon}_c^{pl})}{\bar{\sigma}_t(\tilde{\varepsilon}_t^{pl})}(1 - \alpha) - (1 + \alpha) \quad (2.37)$$

$$\gamma = \frac{3(1 - K_c)}{2K_c - 1} \quad (2.38)$$

In Equation (2.35), $\hat{\sigma}_{max}$ is the maximum principle effective stress. $\frac{\sigma_{b0}}{\sigma_{c0}}$ is the ratio of initial equi-biaxial compressive yield stress to initial uniaxial compressive yield stress, the default value of 1.16 selected in this study. K_c is the ratio of the second stress invariant on the tensile meridian $q_{(TM)}$ to the second stress invariant on the compressive meridian $q_{(CM)}$, the values of it shown in Figure 2.8 at any value of the hydrostatic

stress. The default value is $2/3$ which is used in this study. $\bar{\sigma}_t(\bar{\varepsilon}_t^{pl})$ and $\bar{\sigma}_c(\bar{\varepsilon}_c^{pl})$ are the effective tensile cohesion stress and the effective compressive cohesion stress, respectively. Typical yield surfaces illustrated in Figure 2.8 and Figure 2.9 in the deviatoric plane and in the plane stress conditions, respectively.

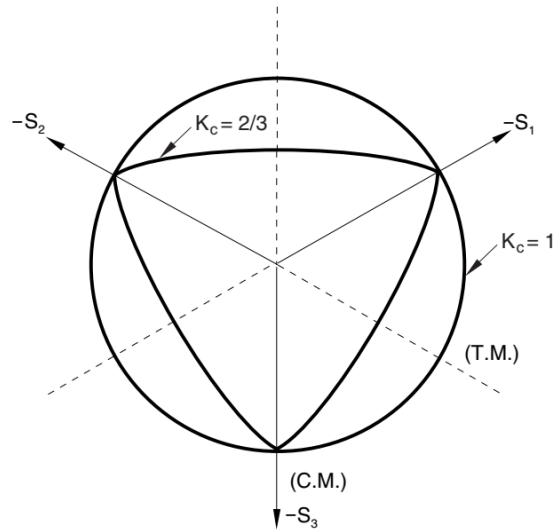


Figure 2.8: Yield surfaces in the deviatoric plane showing various K_c values [28]

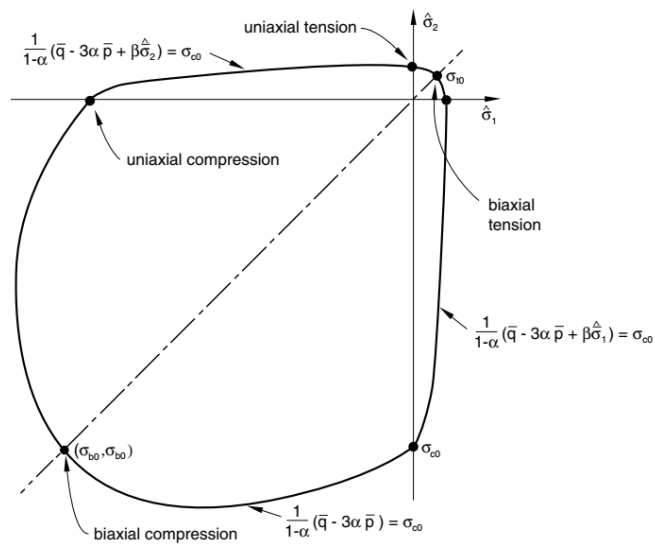


Figure 2.9: Yield surface in plane stress [28]

In the analysis the parameters used in CDP model for Plasticity is summarized in Table 2.1 below.

Table 2.1: The Parameters of Plasticity

Dilation Angle	Eccentricity	σ_{b0}/σ_{c0}	K_c
35	0.1	1.16	2/3

2.3 Development of Finite Element Model in VecTor2

Four and three-point bending test simulations were developed by the preprocessor FormWorks and analyzed through two-dimensional nonlinear finite element code VecTor2 [25]. Full-scale models were established as illustrated in Figure 2.10. Rectangular elements with four nodes and truss bar elements with two nodes were used to simulate the concrete and rebars, respectively. A perfect bond was assumed to model the interaction between concrete and rebar. The compressive and tensile responses of plain and fibrous concrete are represented by the models given in Table 2.2. The steel reinforcements were defined using the models presented in Table 2.3. The available mechanical and physical properties of concrete, steel reinforcement, and fibers were taken from the conducted material tests and given in Chapters 3 and 4. The default values for the other necessary parameters were used as in [25]. Pin and roller supports were not modeled explicitly, but instead; translational and rotational restrictions were given to the required nodes. The static load was increased by 0.1 mm displacement steps. In the preprocessor, the existing crack spacing/allocation formulations, such as CEB-FIB 1978 or Eurocode 2, were derived only for the plain reinforced concrete members, which do not have any fiber content. Therefore, the average crack spacings in fibrous beams were found by visual inspection and given in Table 2.4. Naming convention of beams are given in Chapter 3 and 4.

Table 2.2: The models used to define the response of plain and fibrous concrete

Material Property	Model
Concrete - Compression Pre-Peak	Beams w/o fibers: Popovics (HSC) Beams w/SF: Lee et al 2011 (FRC)
Concrete - Compression Post-Peak	Beams w/o fiber and w/stirrups: Modified Kent-Park Beams w/o fiber and stirrups: Base curve Beams w/SF: Lee et al 2011 (FRC)
Concrete – Compression Softening	Vecchio 1992-A (e1/e2 form)
Concrete – Tension Stiffening	Lee 2010 (w/ Post-Yield)
Concrete – Tension Softening	Beams w/o fiber: Bilinear Beams w/SF: Exponential
FRC Tension	SDEM – Monotonic

Table 2.3: The models were used to define the response of steel reinforcement

Material Property	Model
Rebar Dowel Action	Tassios (Crack Slip)
Rebar Buckling	Akkaya 2012 (Modified Dhakal- Maekawa)

Table 2.4: The average crack spacing of fibrous beam specimens

	Specimen					
	S	M	L	B2	B3	B4
Average crack spacing (mm)	130	150	161	100	121	115

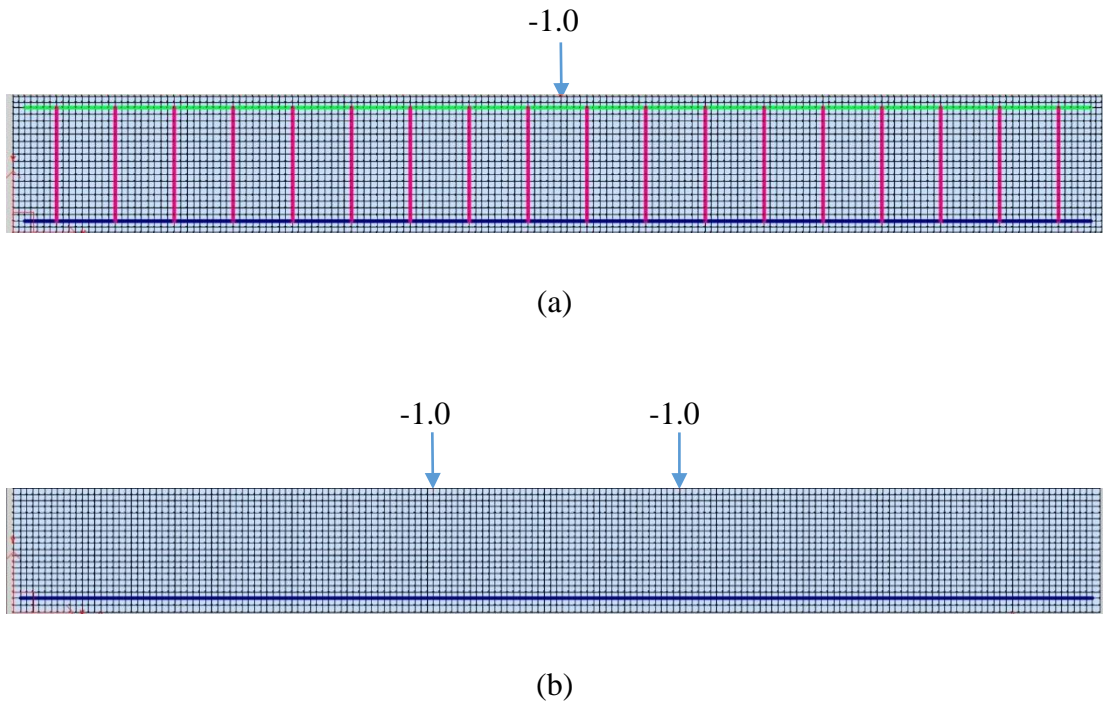


Figure 2.10: FE model of (a) reinforced concrete beam with stirrups (b) and fibrous concrete without stirrups

2.4 Development of Finite Element Model in ABAQUS

Next, four and three-point bending test simulations were conducted by three dimensional ABAQUS/Explicit NLFE software. Full-scale models were created. Construction of numerical models are explained in detail as follows.

2.4.1 Reinforced Concrete Beams

The behavior of concrete material was described by the concrete damage plasticity model (CDP). Eight node linear brick elements with reduced integration points were selected to construct the concrete beam parts as shown Figure 2.11 (left) and (right). Such type of solid elements decreases the analysis duration and can be utilized for complex nonlinear analyses including plasticity and large deformation. Therefore, C3D8R element type was selected.

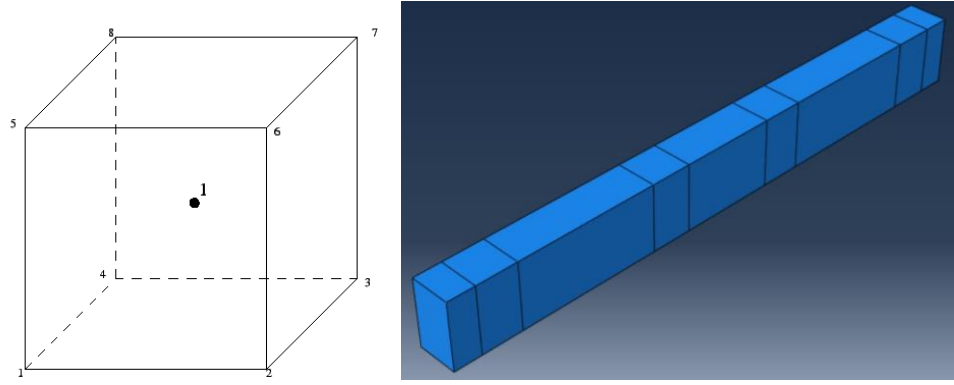


Figure 2.11: (Left) Solid element with reduced integration point, (Right) 3D Solid concrete beam part

2.4.2 Modeling the Compressive Response of Concrete

2.4.2.1 Concrete in the Selected Study

The compression test results of cylinder plain and fibrous concrete samples were directly taken from the selected study [15] and drawn in Figure 2.12 and Figure 2.13. Based on Equations (23) and (24) the response was converted into stress versus inelastic strain. Elastic modulus of both type concretes were computed through Equations (2.39) and (40) as suggested by [32] and [22], respectively.

$$E_c = 2.15 \times 10^4 \left(\left(\frac{f'_c}{10} \right)^{\frac{1}{3}} \right) \quad (2.39)$$

$$E_c = \left(-367V_f \frac{l_f}{d_f} + 5520 \right) f_c'^{0.41} \quad (2.40)$$

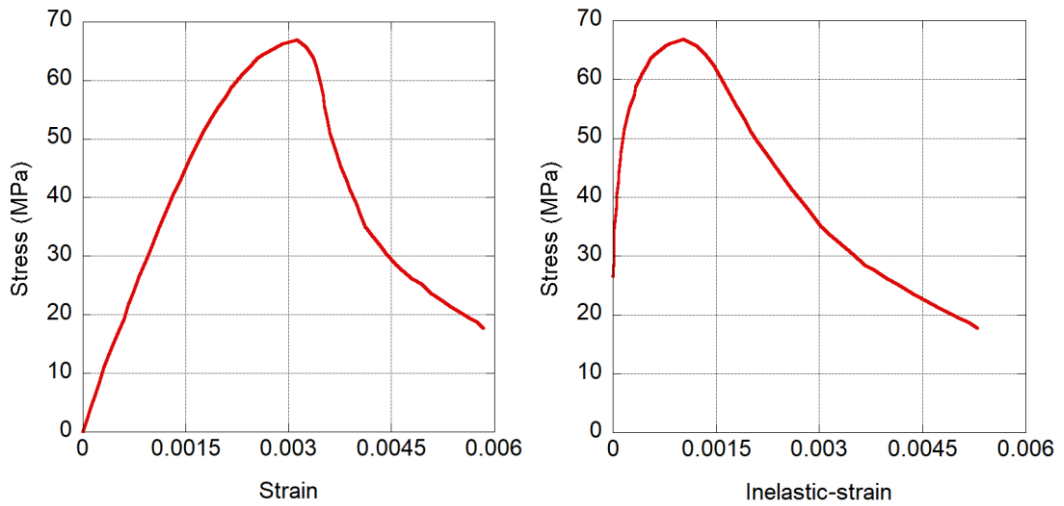


Figure 2.12: Compression behavior of plain concrete (taken from [15])

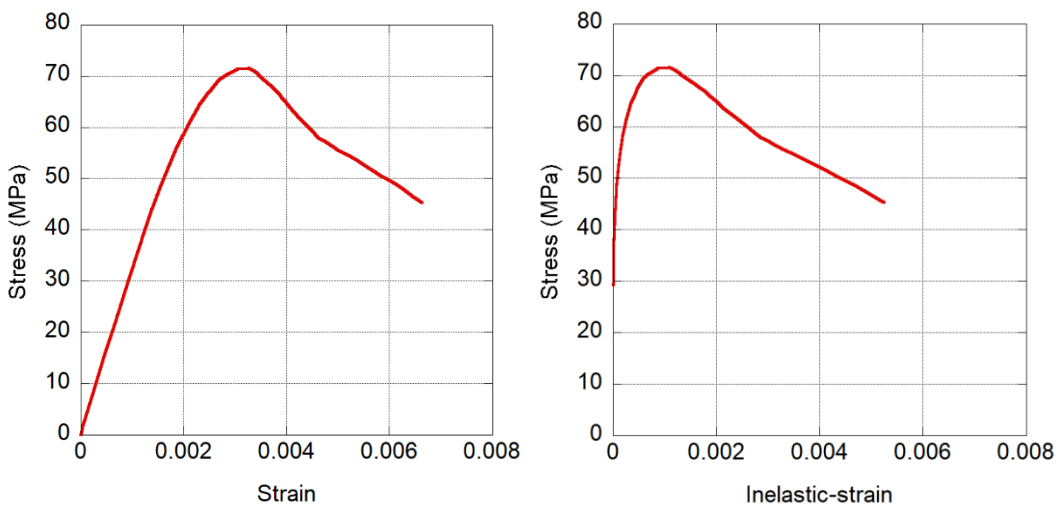


Figure 2.13: Compression behavior of concrete with fiber (taken from [15])

2.4.2.2 Concrete in the Conducted Laboratory Work

Compression behavior of plain concrete was modeled using Popovics (HSC) parabola [33] associated with the Kent and Park model [34]. Popovics (HSC) parabola was used until the peak stress corresponding to 0.002 strain. Afterwards, Kent and Park model followed beyond the maximum stress standing for confined concrete behavior as given in Figure 2.14. The compression stress-strain relationship proposed by Popovics is

expressed by Equation (2.41, 2.42 and 2.43) while Kent model is stated by Equations (2.44, 2.45, 2.46, and 2.47). The elastic modulus of the concrete is estimated via Equation (2.39). Where b_w is width of section, and s is the tie spacing in the Equation (2.47).

$$f_c = \left(\frac{\varepsilon_c}{\varepsilon_0}\right) f'_c \frac{n}{n - 1 + \left(\frac{\varepsilon_c}{\varepsilon_0}\right)^{nk}} \text{ for } \varepsilon_c < \varepsilon_0 \quad (2.41)$$

$$n = 0.80 + \frac{f'_c}{17} \quad (2.42)$$

$$k=1 \text{ for } \varepsilon_c < \varepsilon_0 \quad (2.43)$$

$$f_c = f'_c(1 - Z(\varepsilon_c - \varepsilon_0)) \text{ for } \varepsilon_c > \varepsilon_0 \quad (2.44)$$

$$Z = \frac{0.5}{\varepsilon_{50u} + \varepsilon_{50h} - 0.002} \quad (2.45)$$

$$\varepsilon_{50u} = \frac{3 + 0.29 f'_c}{145 f'_c - 1000} \quad (2.46)$$

$$\varepsilon_{50h} = \frac{3}{4} \rho_s \sqrt{\frac{b_w}{s}} \quad (2.47)$$

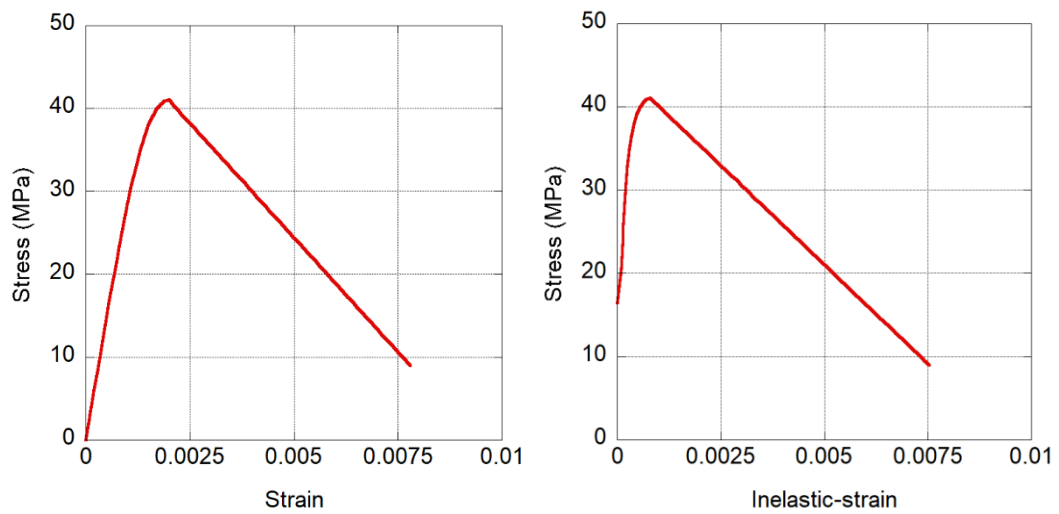


Figure 2.14: Analytically calculated compressive behavior of confined plain concrete

Compressive response of FRC was modeled using Lee model [22], Figure 2.15. The stress-strain relationship proposed by Lee is expressed in Equations (2.48, 2.49, 2.50, 2.51, and 2.52) in which V_f is the volumetric fiber ratio, l_f and d_f are the length and diameter of steel fiber, respectively. The modulus of elasticity of the fibrous concrete is computed through Equation (2.40).

$$f_c = f'_c \left(\frac{A \left(\frac{\varepsilon_c}{\varepsilon_0} \right)}{A - 1 + (\varepsilon_c / \varepsilon_0)^B} \right) \quad (2.48)$$

$$A = B = \frac{1}{1 - \left(\frac{f'_c}{\varepsilon_0 E_c} \right)} \text{ for } \frac{\varepsilon_c}{\varepsilon_0} \leq 1.0 \quad (2.49)$$

$$A = 1 + 0.723 \left(V_f \frac{l_f}{d_f} \right)^{-0.957} \text{ for } \frac{\varepsilon_c}{\varepsilon_0} > 1.0 \quad (2.50)$$

$$B = \left(\frac{f'_c}{50} \right)^{0.064} \left(1 + 0.882 \left(V_f \frac{l_f}{d_f} \right)^{-0.882} \right) \geq A \text{ in Equation (2.50) for } \frac{\varepsilon_c}{\varepsilon_0} > 1.0 \quad (2.51)$$

$$\varepsilon_0 = \left(0.0003 V_f \frac{l_f}{d_f} + 0.0018 \right) f'_c{}^{0.12} \quad (2.52)$$

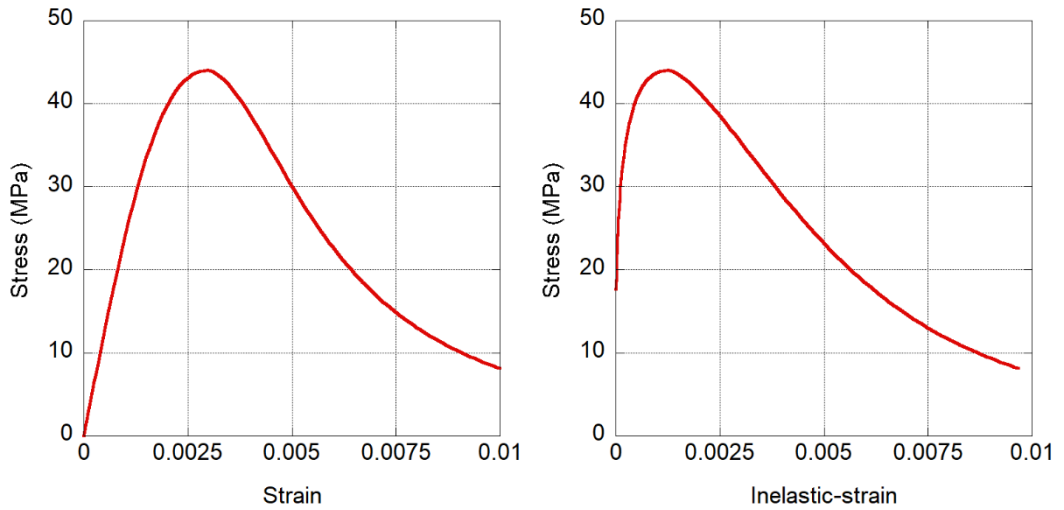


Figure 2.15: Analytically calculated compression behavior of fibrous concrete

2.4.3 Modeling the Tensile Response of Concrete

In all analyses, tension stiffening effect was also considered through a fracture energy dependent model proposed by Hordijk [35] for plain concrete and the SDEM model proposed by Lee [21] for fibrous concrete. In the Hordijk model, tension stress versus crack opening width relationship is expressed by Equation (2.53), and the calculated curve is presented in Figure 2.16. In Equation (2.53), w_t is crack opening width; w_{cr} is the crack opening width at the complete loss of tensile stress and given by Equation (2.54); σ_t tensile stress normal to crack direction, f_t concrete uniaxial tensile strength and $c_1=3.0$ and $c_2=6.93$ are constants determined from tensile tests of concrete. CEB-FIP (1991) model [32], was used in this report to determine G_F by Equations (2.55) in which d_a is the maximum aggregate size of concrete. The Poisson's ratio (ν) was taken as 0.2. In the selected study, the direct tensile strength of plain concrete was calculated using Equation (2.56) which suggested by [32].

$$\frac{\sigma_t}{f_t} = \left(1 + \left(c_1 \frac{w_t}{w_{cr}}\right)^3\right) e^{-c_2 \frac{w_t}{w_{cr}}} - \frac{w_t}{w_{cr}} (1 + c_1^3) e^{-c_2} \quad (2.53)$$

$$w_{cr} = 5.14 \frac{G_F}{f_t} \quad (2.54)$$

$$G_F = (0.0469d_a^2 - 0.5d_a + 26) \left(\frac{f'_c}{10}\right)^{0.7} \text{ (N/mm)} \quad (2.55)$$

$$f_t = 1.4 \times \left(\frac{f'_c}{10}\right)^{\frac{2}{3}} \quad (2.56)$$

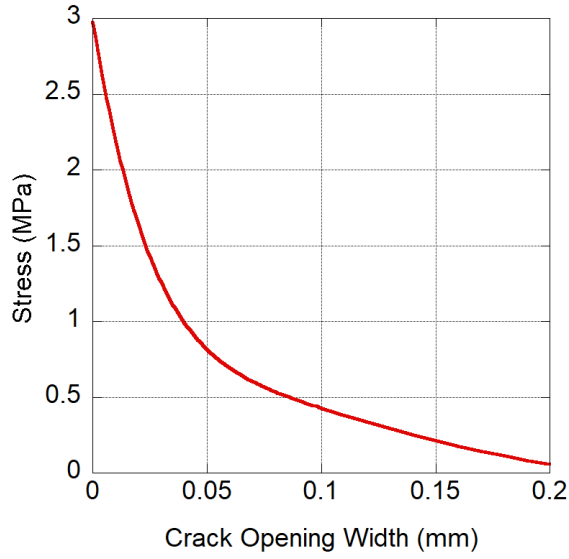


Figure 2.16: Calculated tensile behavior of plain concrete using [35]

On the other hand, tension stress versus crack opening width relationship of fibrous concrete is calculated based on SDEM model and presented in Figure 2.17. The tensile strength of concrete having steel fiber is expressed in Equation (2.57), where f_f is the tensile stress carried by steel fiber and f_{ct} presents the tensile stress provided by the concrete portion, Equation (2.58). In here it should be noted that, $f_f = f_{st}$ for straight fibers, $f_f = f_{st} + f_{eh}$ for hooked-end fibers. f_{st} and f_{eh} presents the tensile stresses attained by fibers due to frictional bond behavior and mechanical anchorage effect, respectively and given in Equation (2.59 and 2.60). In these Equations, α_f is the fiber orientation factor that can be assumed to be 0.5, K_{st} and K_{eh} are the factors to represent average pullout stresses of fiber due to frictional bond behavior and mechanical anchorage of hooked-end fiber, respectively. Additionally, $\tau_{f,max}$ and $\tau_{eh,max}$ are the frictional bond strength and the mechanical anchorage strength, l_i stands for the distance between mechanical anchorages for hooked end fiber. Finally, for plain concrete the coefficient c in Equation (2.58) is 15. In the selected study, the equivalent direct strength of fibrous concrete was calculated by converting the tensile strength obtained from four-point beam as suggested by [36].

$$f_{SFRC} = f_f + f_{ct} \quad (2.57)$$

$$f_{ct} = f_{cr}e^{-cw_{cr}} \quad (2.58)$$

$$f_{st} = \alpha_f V_f K_{st} \tau_{f,max} \frac{l_f}{d_f} \left(1 - \frac{2w_{cr}}{l_f}\right)^2 \quad (2.59)$$

$$f_{eh} = \alpha_f V_f K_{eh} \tau_{eh,max} \frac{2(l_i - 2w_{cr})}{d_f} \quad (2.60)$$

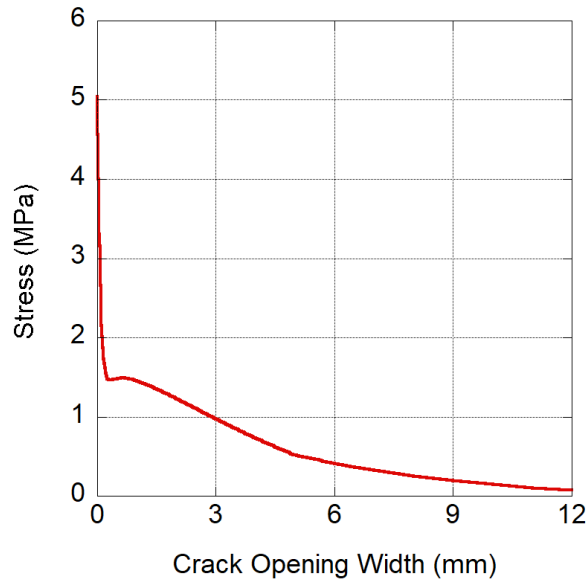


Figure 2.17: Calculated tensile response of concrete with hooked-end fibers using [21]

2.4.4 Support and Load Plates

Support conditions and loading plates were explicitly modeled using eight node brick elements with reduced integration (C3D8R) as rectangular prisms with the dimension of 300x300x50 mm in length, width, and thickness, respectively. The load is applied as an incremental displacement using the middle plates at the top of beam as illustrated in Figure 2.18. The interaction between the plates and the beam specimens was provided by tie constraint and general contact explicit with frictional coefficient of 0.57 to inspect the effect of these two techniques on the results.

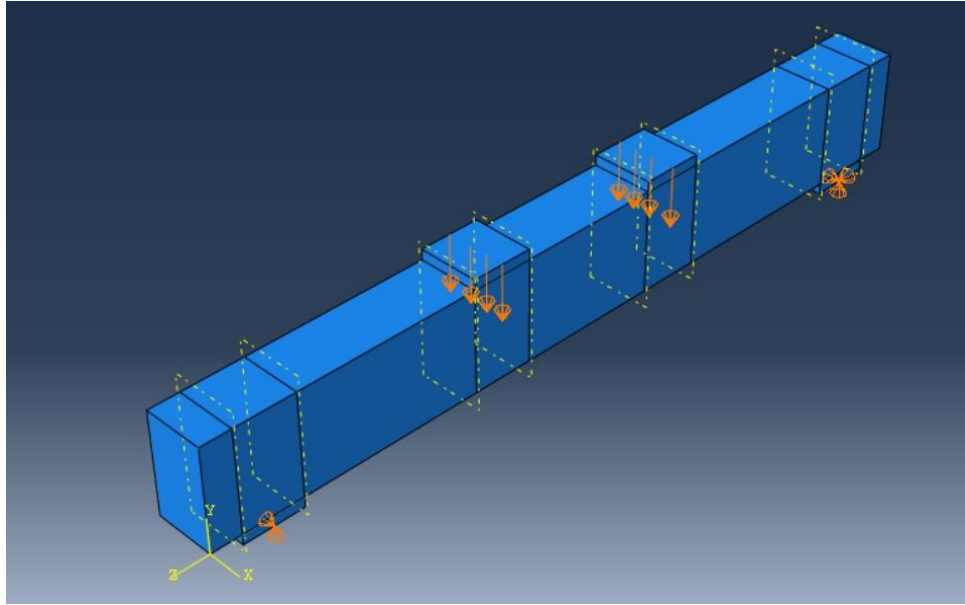
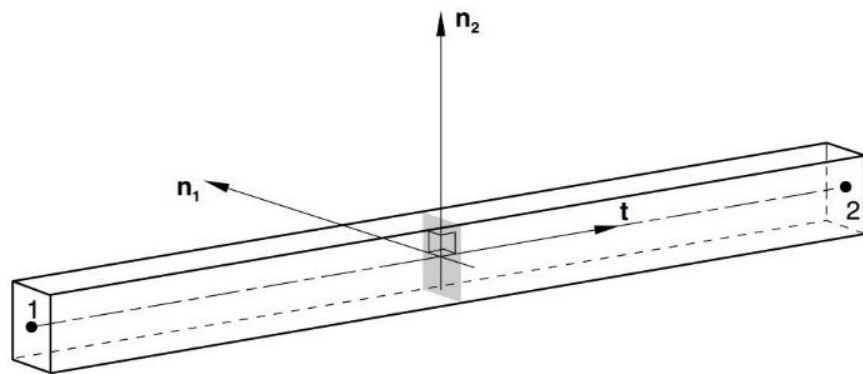


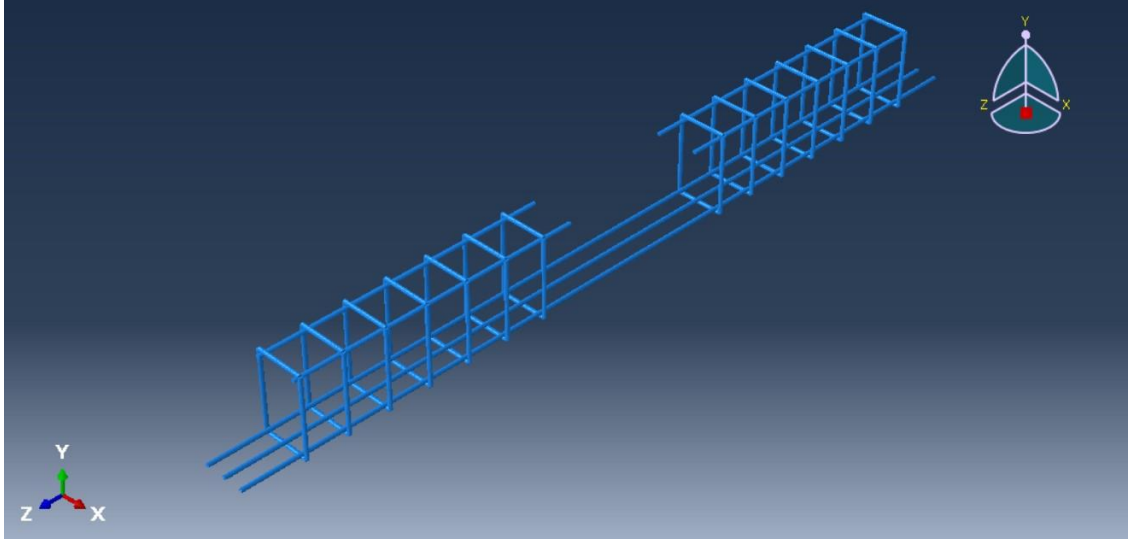
Figure 2.18: The FE model of the beam with two loading plates at top

2.4.5 Steel Reinforcement Rebars

Modeling of rebars was conducted using 3D two node linear beam elements (B31) as shown in Figure 2.19 (a). Additionally, Figure 2.19 (b) presents the steel reinforcement part. The embedded element technique was used to establish perfect bond between concrete brick elements and steel reinforcement beam elements. For this purpose, concrete elements were selected to be host elements while steel reinforcement was being embedded to the host material.



(a)



(b)

Figure 2.19: (a) 3D two node linear beam elements, (b) and steel reinforcement part

The stress-strain relationship of steel reinforcements was established using the piecewise functions provided in the Turkish Building Earthquake Code (TBEC) 2018 [37] and then converted into true stress-strain curve as specified in the ABAQUS manual using Equations (2.61) and (2.62), Figure 2.20 (a). In the Equations σ_{true} is the true stress, σ_{nom} is the engineering or nominal stress while ϵ_{true} is the true strain, and ϵ_{nom} is the engineering strain. The plastic range of material behavior was introduced to ABAQUS by subtracting the elastic strain from the overall strain as shown in Equation (2.63) where E_s is the modulus of elasticity of the steel, Figure 2.20 (b).

$$\sigma_{true} = \sigma_{nom}(1 + \epsilon_{nom}) \quad (2.61)$$

$$\epsilon_{true} = \ln(1 + \epsilon_{nom}) \quad (2.62)$$

$$\epsilon_{plastic} = \epsilon_{true} - \left(\frac{\sigma_{true}}{E_s}\right) \quad (2.63)$$

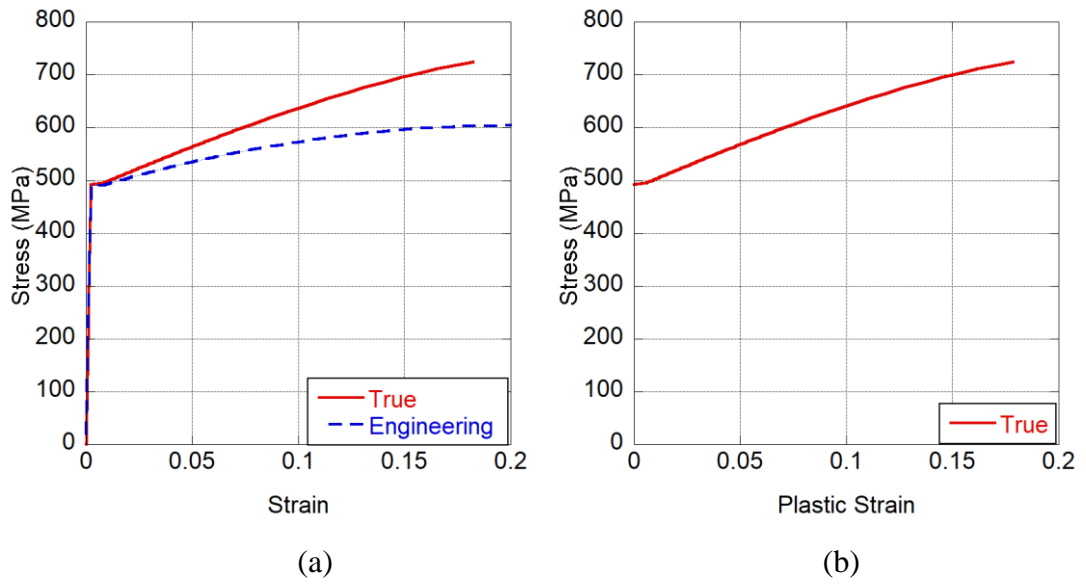


Figure 2.20: (a) The true and engineering model of steel reinforcements with a yield strength of 490 MPa, (b) and true plastic stress-strain curve

Chapter 3

Validation of FE model on Flexure Critic Beams Using Literature

3.1 Introduction

This chapter presents the results of MCTF, and plasticity based NLFE analyses of beams critical in flexure. In here, a parametric study was also performed by ABAQUS to understand the effect of contact type, tension stiffening models of fibrous concrete and mesh size on the response under quasi-static load. Once the results were obtained, a validation job of both theoretical approaches was done. Here, validation of finite element method refers to the process of verifying the accuracy, sensitivity and reliability of the constructed finite element models by comparing its predictions with those of experimental.

3.2 Preparation of Test Specimens

The study conducted by [15], included the four-point bending tests of five simply supported RC beams, Figure 3.1, and two of them had plain concrete with stirrups while the rest had fibrous concrete without stirrups. Three different sizes of beams were manufactured to evaluate the size effect. The dimensions are summarized in Table 3.1.

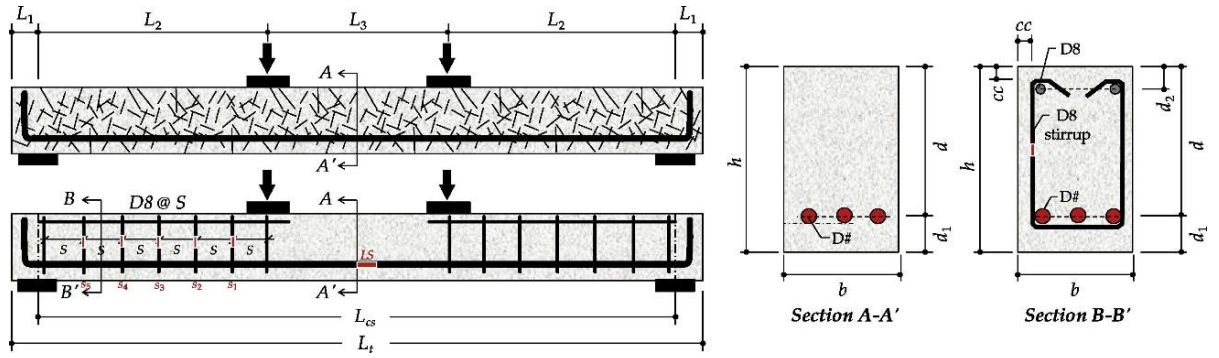


Figure 3.1: Specimen geometry and reinforcement details [15]

Table 3.1: Dimensions of test specimens

	L_t (mm)	L_{cs} (mm)	h (mm)	b (mm)	d (mm)
S-N	2000	1700	250	150	197
S-SF	2000	1700	250	150	197
M-SF	3200	2550	350	210	294
L-N	4400	3700	500	300	442
L-SF	4400	3700	500	300	442

The symbols “S”, “M” and “L” refers to small, medium, and large beam sizes, respectively. And the symbols N and SF stand for concrete w/o fiber and w/fiber respectively. The reinforcement ratios were selected between 0.64% and 0.72%. The mechanical and physical properties of rebars are summarized in Table 3.2. A minimum amount of transverse reinforcement was employed in the beams having plain concrete to prevent the brittle shear failure. However, no shear reinforcement was used in the beams having concrete w/fibers to investigate the contribution of hooked end steel fibers to the shear strength.

Table 3.2: The details and properties of steel reinforcing

	(D#)	Reinforcement ratio ρ (%)	A_s (mm ²)	f_y (Mpa)	E_s (GPa)	ϵ_y	ϵ_u	s (mm)
S-N	D10	0.72	3x71.3	491	200	0.0025	0.20	98
S-SF	D10	0.72	3x71.3	491	200	0.0025	0.20	-
M-SF	D16	0.64	2x198.6	510	200	0.0026	0.19	-
L-N	D19	0.65	3x286.5	473	200	0.0024	0.19	220
L-SF	D19	0.65	3x286.5	473	200	0.0024	0.19	-

3.3. Experiments

The compressive strength of plain and fibrous concrete was detected to be 67 and 72 MPa, respectively. The hooked end steel fibers have a diameter of 0.55 mm and length of 35 mm. Volumetric fraction of steel fiber was selected to be 0.75% based on the recommendations of [38] for all SFRC beams. The mechanical and physical properties of hooked end steel fiber are summarized in Table 3.3.

Table 3.3: Properties of hooked steel fibers

	Diameter d_f (mm)	Length l_f (mm)	Aspect Ratio (l_f/d_f)	Density (g/cm ³)	Tensile Strength (MPa)	Elastic Modulus (GPa)
Hooked steel fiber	0.55	35	65	7.9	1400	200

Four-point loading tests were performed via displacement controlled universal testing machine (UTM) with a maximum capacity of 2000 kN, Figure 3.2. The applied load, mid-span deflection and strain occurring in steel reinforcement were recorded instantaneously by a data acquisition device. The results included load-displacement response, failure modes and crack patterns, to validate the numerical models.

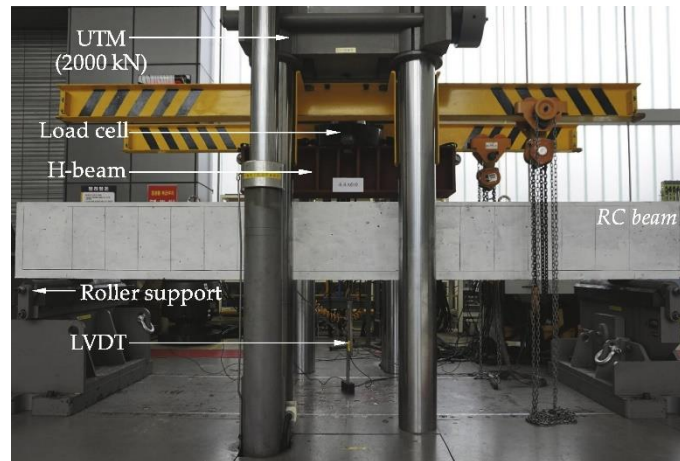


Figure 3.2: Four point bending structural test set up [15]

3.4 Results and Discussion

3.4.1 Predicted Response using Plasticity Analysis (ABAQUS)

3.4.1.1 Parametric Study

The effects of contact type, tension stiffening model and mesh sensitivity to the FE analysis results of the small size SFRC beams were investigated.

3.4.1.1.1 Contact Type

As mentioned in Section 2.4.4, the interaction between beam specimens and plates was modeled using two different methods to understand their effect on the FE analysis. First a general contact explicit was used with tangential and normal behavior. A tangential behavior was defined using a penalty friction with friction coefficient of 0.57 as suggested by [39]. In addition, normal behavior was introduced by hard contact. Next, a tie constraint interaction technique was used by defining a master and slave surface. The surfaces were selected according to the element stiffness in which the elements having higher material stiffness were defined to be master and the other elements were assigned to be slave. Therefore, concrete was selected as slave surface, and steel plates were selected as master surface. The load-deflection curves obtained

from both contact types were illustrated in Figure 3.3. In addition, the analysis results were summarized in Table 3.4. It can be inferred that the required analysis time for tie constraint interaction was slightly lower than the general contact explicit. However, when the accuracy of peak load estimation and its corresponding deflection considered, general contact type resulted in more accurate outcomes. Therefore, the general contact explicit type of interaction model was selected in the current study.

Table 3.4: The effect of contact type on the FE analysis results

	Experiment	Contact Type	
		General Contact Explicit	Tie Restraint
Peak Load (kN)	107.3	101.1	100.6
Deflection at Peak Load (mm)	5.5	5.3	4.6
Computation Time (s)	-	4638	3768

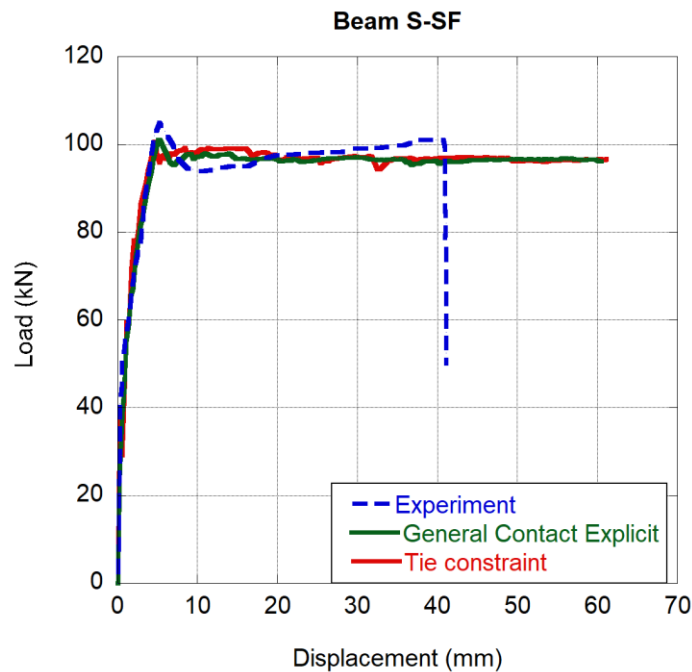


Figure 3.3: Comparison of load-deflection response of small SFRC beam with different contact types

3.4.1.1.2 Tension Stiffening Models

Two different tension stiffening models were utilized for the analysis, namely: (1) SDEM [21] and (2) Fib Model Code 2010 [40]. Both methods depend on fracture energy, and it is calculated using the relation of tensile stress versus crack width. This relationship defines the tensile behavior of fibrous concrete in the numerical model, as shown in Figure 3.4. Using the models fracture energy was computed at a crack width of 5 mm and presented in Table 3.5. On the other hand, the load-displacement response of the specimen was illustrated in Figure 3.5. It can be observed from the results that the SDEM model captured the response of the beam specimen more accurately than FIB model, where the FIB model caused an overestimation in the post-yield region. This is due to the higher fracture energy calculated from the FIB model as shown in Table 3.5. Therefore, the SDEM model was selected in the current study.

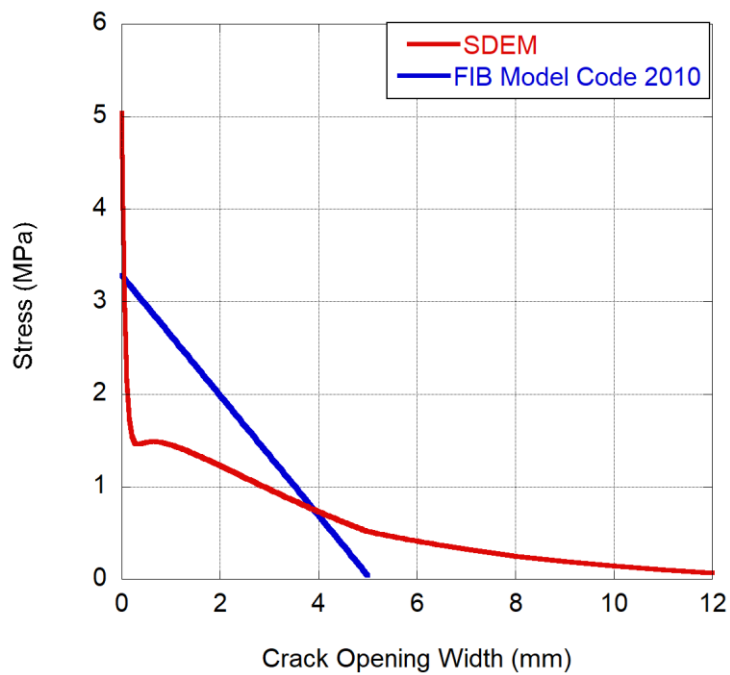


Figure 3.4: Calculated tensile behavior of fibrous concrete using SDEM and FIB Model Code 2010

Table 3.5: The computed fracture energies

<i>Tension Stiffening Model</i>	<i>Calculated Fracture Energy @5 mm crack width (N/mm)</i>
FIB Model Code 2010	8.33
SDEM	5.64

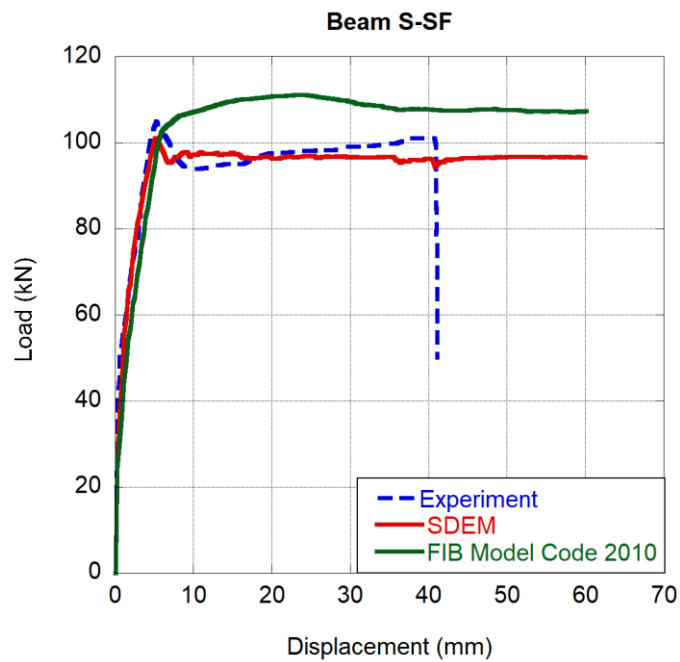


Figure 3.5: Comparison of load-deflection response of small SFRC beam with different tension stiffening models

3.4.1.1.3 Mesh Sensitivity

A mesh convergence study was performed to find the mesh size that yields the most accurate results with the minimum amount of computational resources. For this purpose, different mesh sizes such as 50, 35, 25, 15 and 10 were modeled for small size SFRC beam and analyses were carried out until 50 mm mid-span deflection. As can be understood from Table 3.6, the beams with mesh sizes 25, 35 and 50 slightly underestimated the peak load and at least five times overestimated the corresponding deflection. However, the peak load and corresponding deflection was acceptably predicted when 10- and 15-mm mesh sizes were used. In addition, these two mesh

sizes could represent the actual response more successfully than the rest, Figure 3.6. Finally, considering the required solution time the analysis having 10 mm mesh size was eliminated. Therefore, the optimum mesh size was selected to be 15 mm while modeling the small beams in this study. Identically, the rest of the beams were investigated, and based on the results 15- and 20-mm mesh sizes were adopted for the medium and large beams, respectively. Finally, the detected mesh sizes were used in both software, ABAQUS and VecTor2.

Table 3.6: The effect of mesh size on the result of the SFRC beam

	Experiment	Mesh Size				
		10	15	25	35	50
Peak Load (kN)	107.3	107.03	101.1	98.4	95.2	94.3
Deflection at Peak Load (mm)	5.5	5.3	5.3	28.4	59.5	45.1
Computation Time (s)	-	52738	4638	1987	634	287

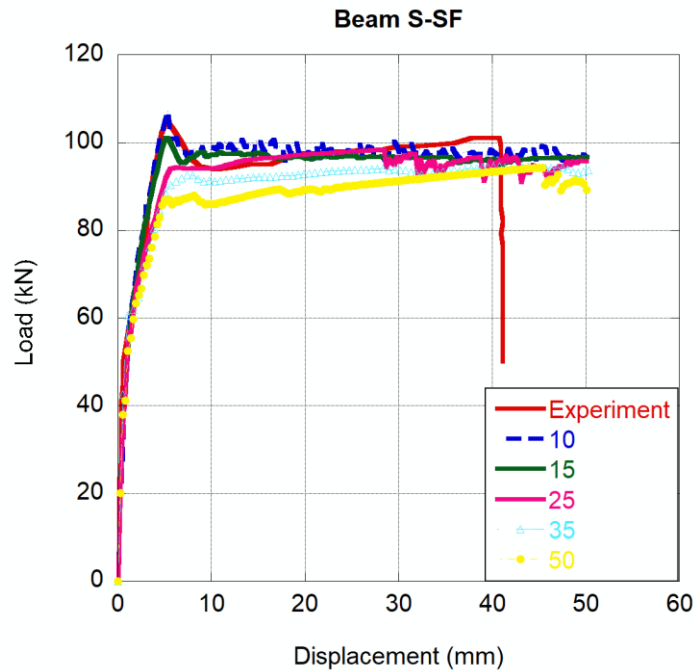


Figure 3.6: Comparison of load-deflection response of small SFRC beam with different mesh sizes

3.4.1.2 Load-Deflection Relationship

The comparative load-deflection results are presented from Figure 3.7 to Figure 3.11. In here it should be noted that, the analyses were not terminated unless a numeric failure occurred (such as a sudden strength loss) and continued until the experimental failure deflection to interpret the general trend of response. Nevertheless, a specific ultimate (failure) point was adopted to determine the proper crack patterns. This was decided based on either the minimum plastic strain in the outermost concrete layer yielding to crush or the ultimate strain in rebars reaching rupture. The crushing strain of plain concrete was understood to be 0.006 from the compression tests of concrete samples in the study taken from the literature. However, the crushing strain of fibrous concrete was set to 0.01 as advised by ACI 544 [41] since the steel fiber additive increases the ductility of the material. Furthermore, the ultimate (or rupture) strain of rebars was taken as specified in the selected study, 0.2.

Firstly, the response of small size SFRC beam investigated. As can be seen from the Figure 3.7, small beam behavior under load could be captured precisely, including the softening behavior of fibrous concrete which ends up with a gradual decrease of flexural load carrying capacity after the peak (or yield) load is reached. The load was predicted to be lower than the experimental value, except in the cracking region. The errors were calculated to be 4, 6 and 4% for yield, peak and ultimate loads. The yield deflection was captured accurately. However, the ultimate deflection was underestimated by 27%.

Investigation followed by the medium size SFRC beam. The yield load and corresponding deflection was predicted precisely by the analysis. The peak and ultimate load were higher than the experimental values by 3 and 5% respectively. However, the rate of error increased for the detected deflections. For example, the deflection corresponding to peak load occurred earlier than the experiment by an error of 63.5% and the ultimate deflection was underestimated by 30%.

Afterwards, the response of large size SFRC beam under load was discussed. As can be understood from Figure 3.9, load-deflection curve exhibited partial agreement. Though the general trend of the curve fits well before yielding of tensile reinforcements, the fluctuation in the post-yield region due to the softening of fibrous

concrete material was not observed in the numerical results. The yield and peak loads were detected by 4 and 0.4% overestimation while 4% underestimation was calculated for the ultimate load. On the other hand, the ultimate deflection was overestimated by 16%.

In the response of small size beam having plain concrete, curve of pre-yield region was predicted accurately. However, the post-yield region exhibited a gradual decrease of load due to crushing of outermost concrete layer. The yield, peak and ultimate loads were computed to be lower than that of the experiment. The calculated errors were 15, 21 and 25%, respectively. On the other hand, the yield deflection was overestimated by 17% whereas the ultimate deflection was underestimated by 54%.

Finally, the behavior of large size beam with plain concrete was investigated. The response before yielding agreed well with that of the experimental. However, the post-yield region tended to decrease gradually due to crushing of concrete. The numerically calculated load was lower than the experimental loads except the cracking load. The rates of errors were 30, 11 and 26% for yield, peak and ultimate load. On the other hand, the ultimate deflection was overestimated by 22%.

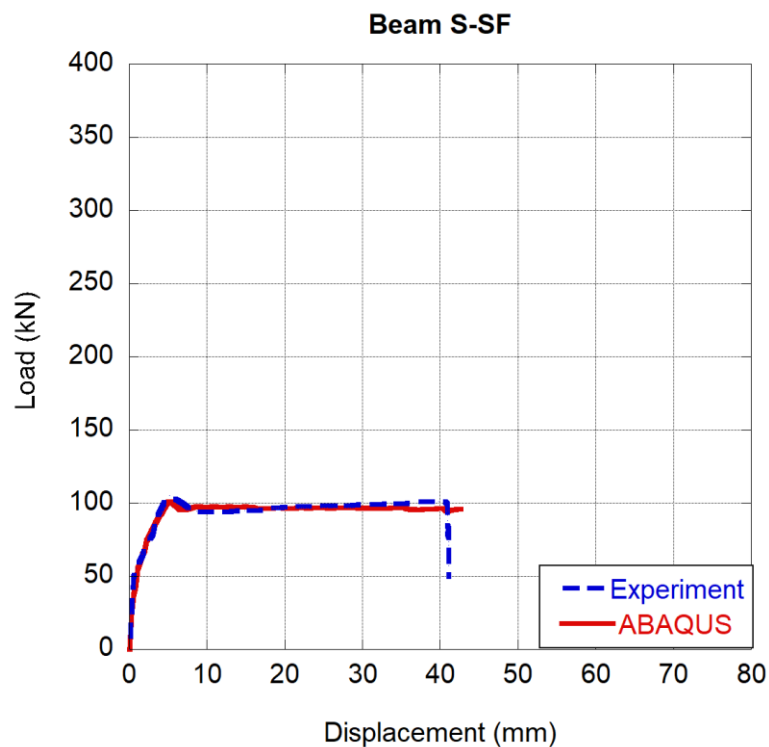


Figure 3.7: Load-mid span deflection curve for S-SF

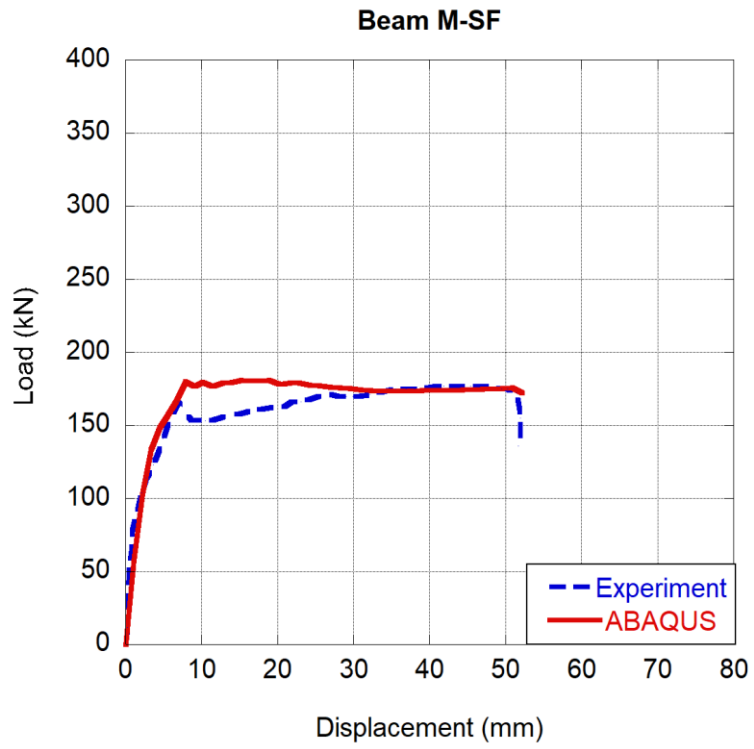


Figure 3.8: Load-mid span deflection curve for M-SF

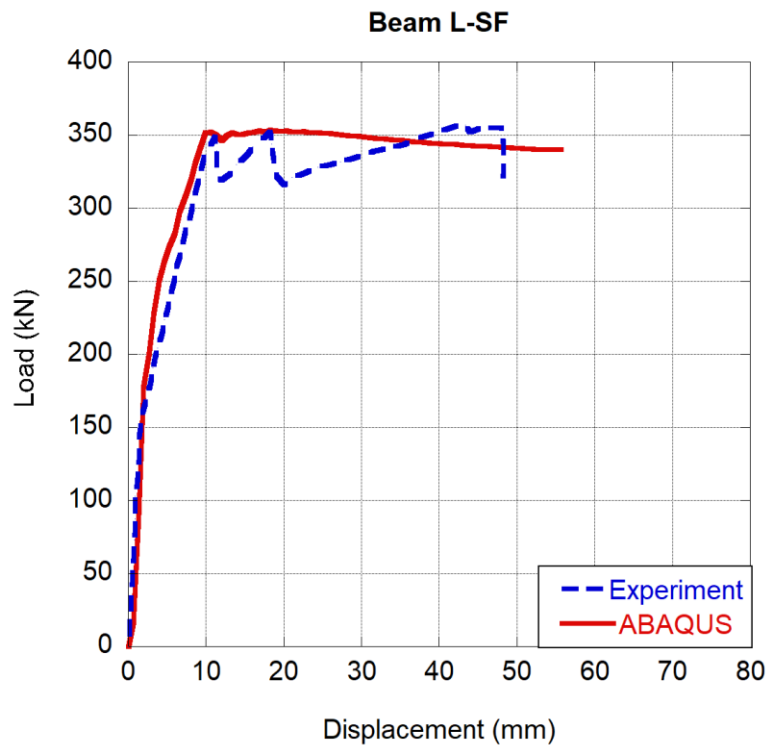


Figure 3.9: Load-mid span deflection curve for L-SF

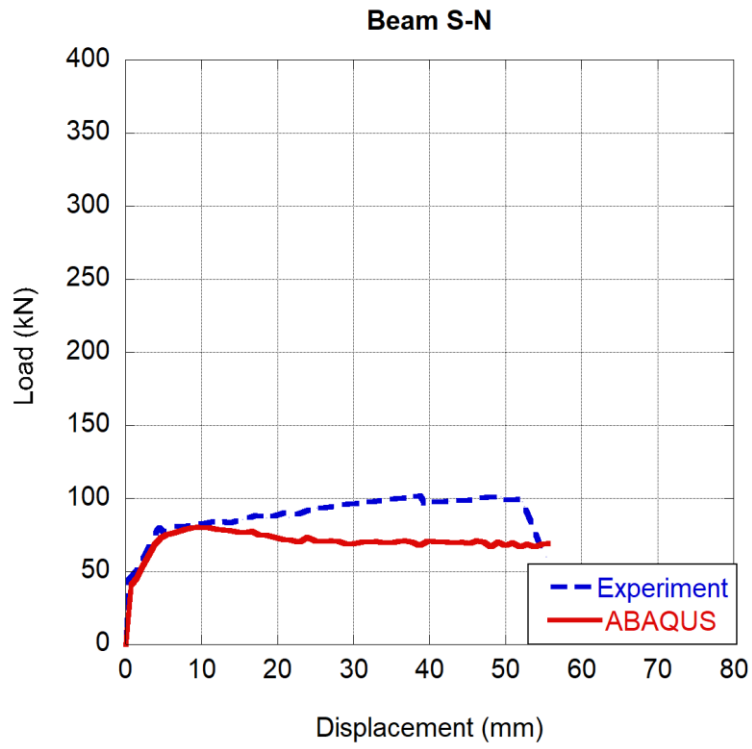


Figure 3.10: Load-mid span deflection curve for S-N

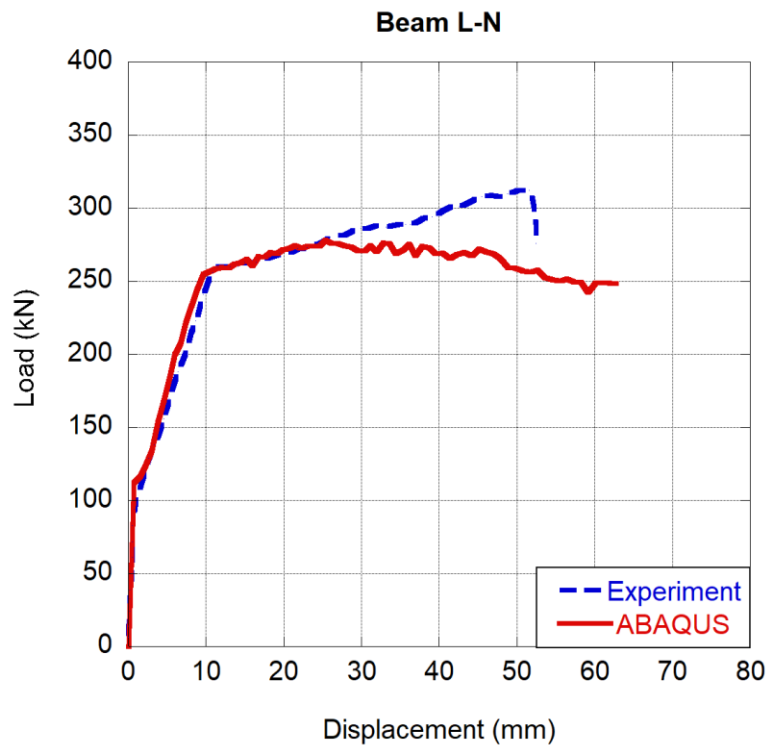


Figure 3.11: Load-mid span deflection curve for L-N

3.4.1.3 Crack pattern

None of the analyses indicate rebar rupture at the previously determined numerical ultimate (failure) deflection, but concrete crushes were detected at the outermost concrete layer since the specified minimum plastic strain values (0.01) and (0.006) were exceeded for SFRC and HSC beams, respectively, Figure 3.12. The computed tension damage profiles compared to their experimental counterparts and shown in Figure 3.13.

As can be seen from the Figure, two major flexural cracks, indicating a crack localization phenomenon, were captured in both small and large SFRC beam, in addition a major flexural crack was captured in the medium beam identical to that of the experiment. However, different than the beams having fibers the flexural cracks significantly propagated into the compression zone in HSC beams w/o fibers. This indicates an enhanced resistance to the propagation of cracks for the fibrous concrete. Finally, it can be concluded that the crack patterns of all specimens could be captured satisfactorily. On the other hand, all the specimens failed from the concrete crush in FE analysis which is identical to the experiment of plain concrete beams but different than the SFRC specimens.

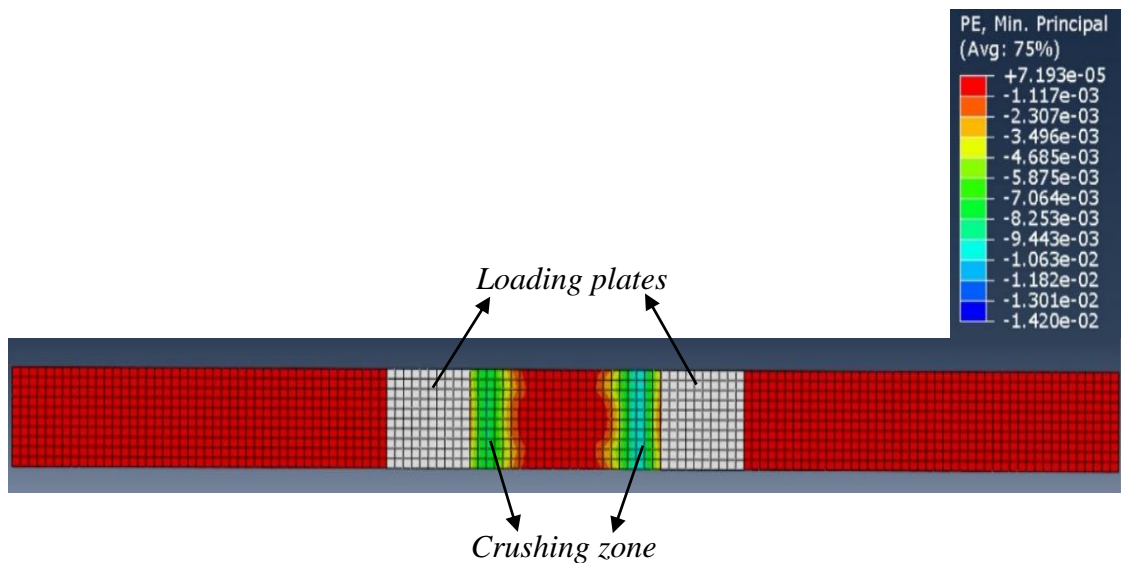
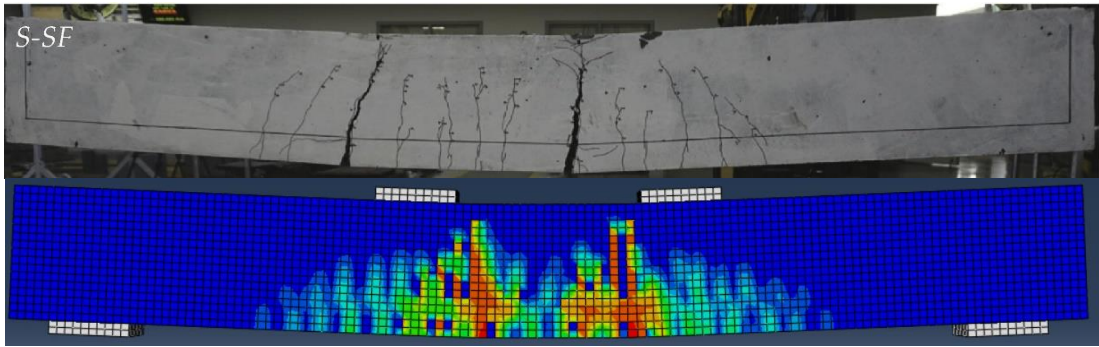
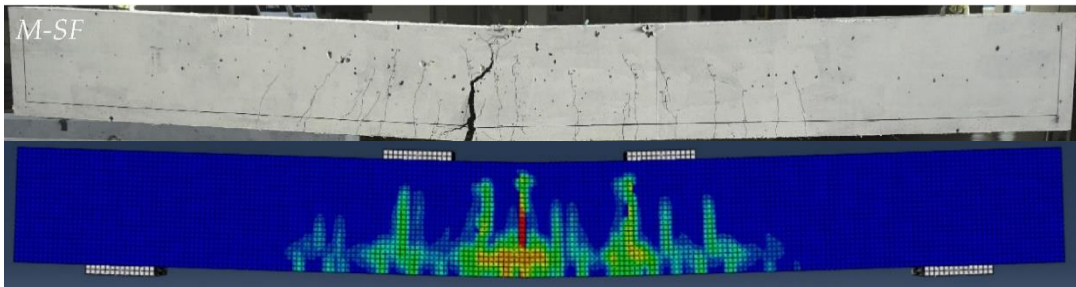


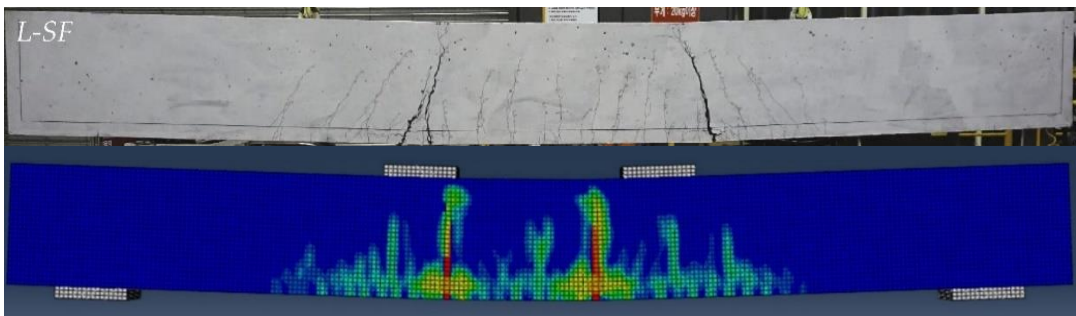
Figure 3.12: The top view of the small beam illustrates the concrete crushes at the outermost layer



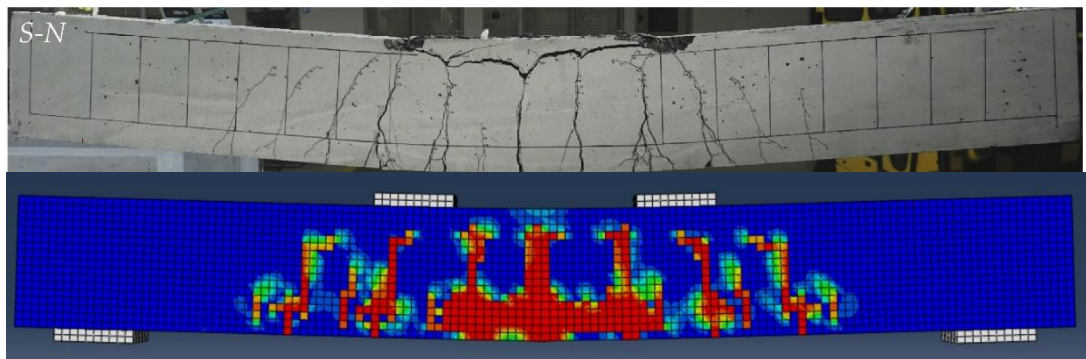
a) Small SFRC beam



b) Medium SFRC beam

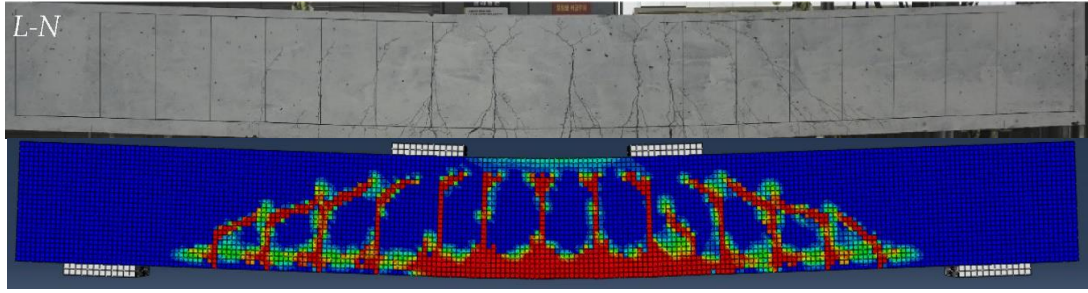


c) Large SFRC beam



d) Small HSC beam

Figure 3.13: Cracking patterns at failure



e) Large HSC beam

Figure 3.13: Cracking patterns at failure (continued)

3.4.1.4 Ductility

The ability of RC beams to deform from yielding to failure is known as ductility. Ductility index is computed by dividing the deflection at the ultimate load Δ_u to the deflection at the yield load Δ_y , as expressed in Equation (3.1). Table 3.7 presents the results obtained from the numerical and experimental study for the HSC and SFRC beams. It can be understood from the results that the ductility index calculated from the FE analysis was higher than the experimental for both of the large size beam specimens, and lower for the small and medium size specimens. In the experiments and FE analyses, the ductility indexes of the large and small size HSC beams w/o fibers were found out to be higher than their SFRC counterparts. Therefore, it can be expressed that numerical analysis is able to capture the tendency of reduction in ductility for the RC beams having hooked end steel fibers with a varying tensile reinforcement ratio between 0.64 to 0.72% by a certain amount of error. On the other hand, the highest ductility in the experiments was detected for the small size HSC beam while it was obtained for large size HSC beam in the FE analysis.

$$\mu_p = \frac{\Delta_u}{\Delta_y} \quad (3.1)$$

Table 3.7: Ductility Indices of the HSC and SFRC beams

Beam Specimen	Ductility Index (FE)	Ductility Index (Test)	Error %
S-N	6.3	11.83	46.7
S-SF	6	8.16	26.5
M-SF	5.4	7.15	24.5
L-N	8.5	4.91	73.1
L-SF	6.5	4.54	43.2

3.4.2 Predicted Response using MCTF Analysis (VecTor2)

3.4.2.1 Load-Deflection Relationship

Load-deflection curves obtained from VecTor2 analysis are presented from Figure 3.14 to Figure 3.18 and compared with that of selected experimental study. In here, the analyses were continued until sudden strength losses calculated by the code and this deflection point denoted as ultimate state or failure. However, the small size beam with plain concrete did not experience a sudden strength loss indicating a numerical failure. Therefore, an exception was made for this beam and the analysis ran until the experimental failure.

The yield, peak and ultimate loads were calculated to be slightly lower than that of experiment for small size SFRC beam. The detected error tended to decrease in the post-yield region (9 and 11% for peak and ultimate load, respectively) while it was calculated to be higher at yielding (15%). On the other hand, the ultimate deflection could be captured accurately in the FE analysis, Figure 3.14.

Next, the response of medium size SFRC beam investigated. The loads were calculated to be lower than that of the experiment, but with decreased margin of error when compared to the previous beam. The calculated errors for yield, peak, and ultimate loads were 3, 1, and 4% respectively. On the other hand, the ultimate deflection was overestimated by 4%.

The investigation followed by large size SFRC beam. Different than the previous two beams, the flexural rigidity was estimated higher as against to the experiment. The loads were determined to be quite close but lower than those of the experimental values. The errors were computed to be 0.1, 0.9 and 7% for the yield, peak and ultimate loads. Finally, the ultimate deflection was underestimated by 1%.

Afterwards, the behavior of small size beam with plain concrete investigated. The yield, peak and ultimate loads were underestimated by 14, 17, and 14%. In this beam there was no sudden loss of strength indicating numeric failure, and hence, the ultimate deflection was decided based on the assumption made in the following section with 43% underestimation.

Finally, the numerical response of large size beam with plain concrete resulted in an exaggeration of the flexural rigidity. In contrast to previous specimens, the yield load was 3% greater than the experimental value. The rest of the loads were lower than the experimental values. Peak and ultimate load errors were calculated to be 3 and 9%, respectively. The ultimate deflection, on the other hand, was overestimated by 29%.

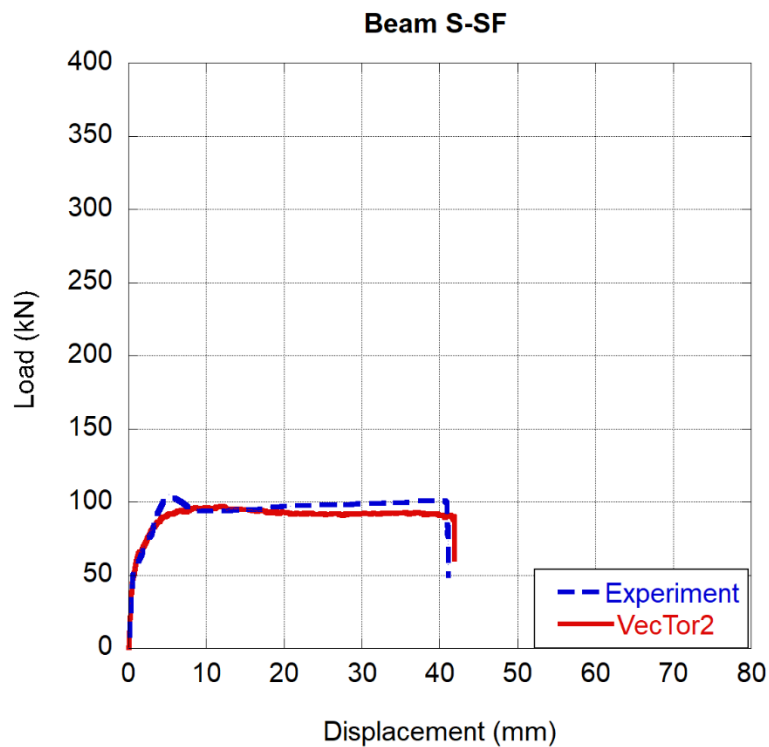


Figure 3.14: Load-mid span deflection curve for S-SF beam

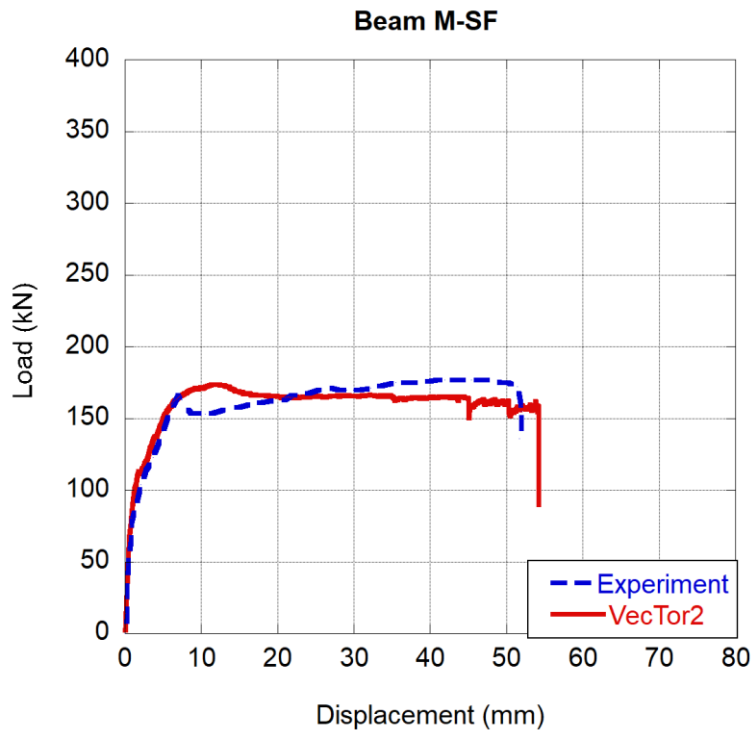


Figure 3.15: Load-mid span deflection curve for M-SF beam

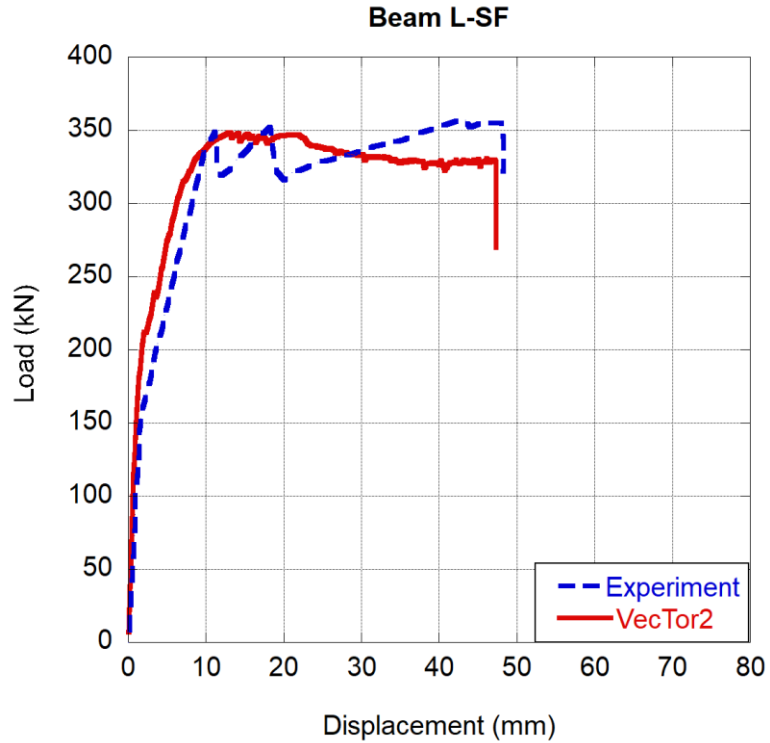


Figure 3.16: Load-mid span deflection curve for L-SF beam

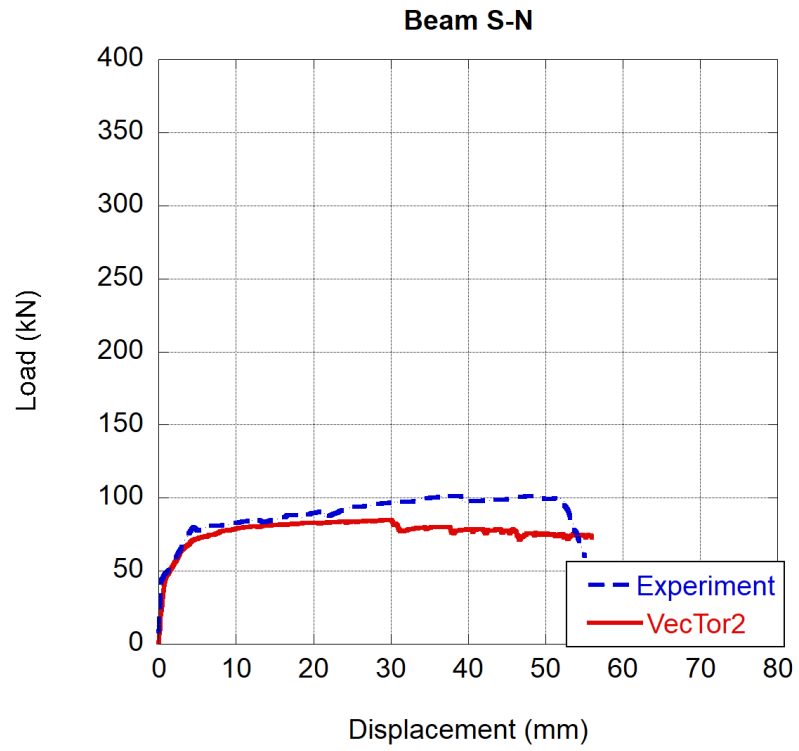


Figure 3.17: Load-mid span deflection curve for S-N

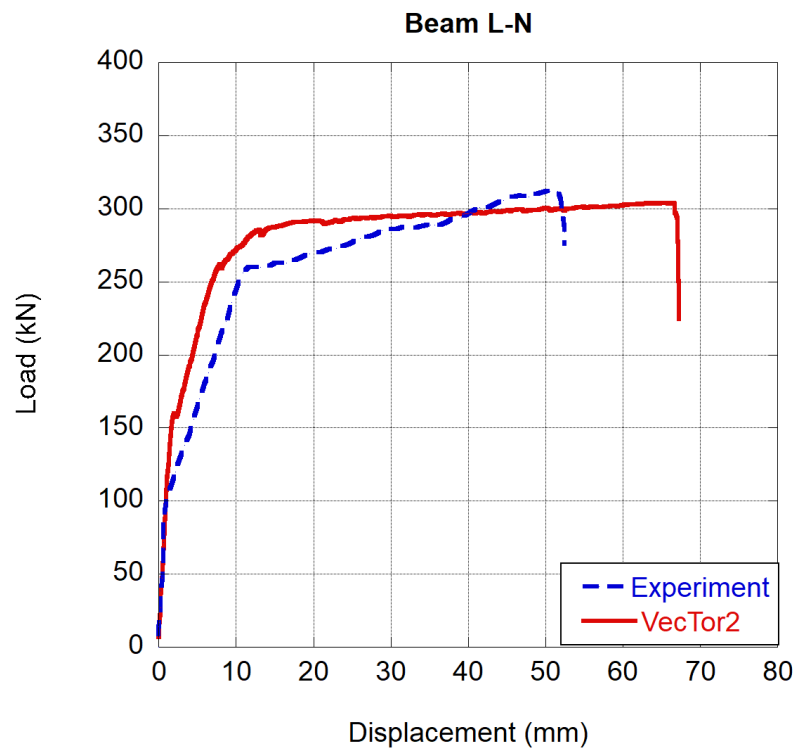
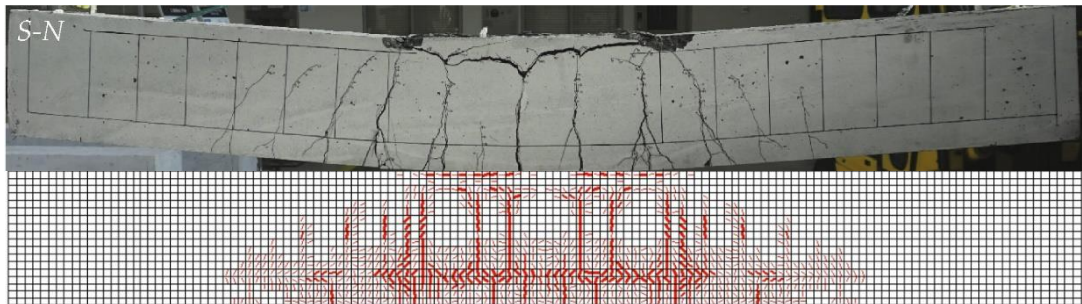


Figure 3.18: Load-mid span deflection curve for L-N beam

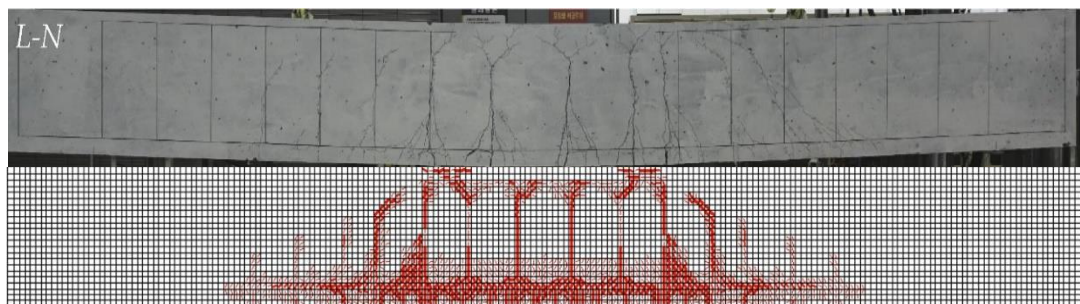
3.4.2.2 Crack pattern

In the numerical analyses of VecTor2, the cracking pattern obtained at the ultimate state, which was occurring due to either crushing of the outermost concrete layer since the specified net principal compressive strain value exceeded or rebar rupture. The obtained numerical failure of all beams was due to rebar rupture except small beam having plain concrete. This beam failed depending on the crushing of concrete.

In the beams without fibers VecTor2 could capture the severe concrete crushes at the outermost layer of beam cross-section as well as the major flexural cracks located at the constant moment region, Figure 3.19 (a and b). The numerical analyses reported widely distributed hairline thick cracks almost along the length of all beams having SF which is eventually not valid for the experimental findings of those beams, Figure 3.19 (c, d and e). In addition, at least one of the major flexural cracks starting from the bottom of the beam could be captured.

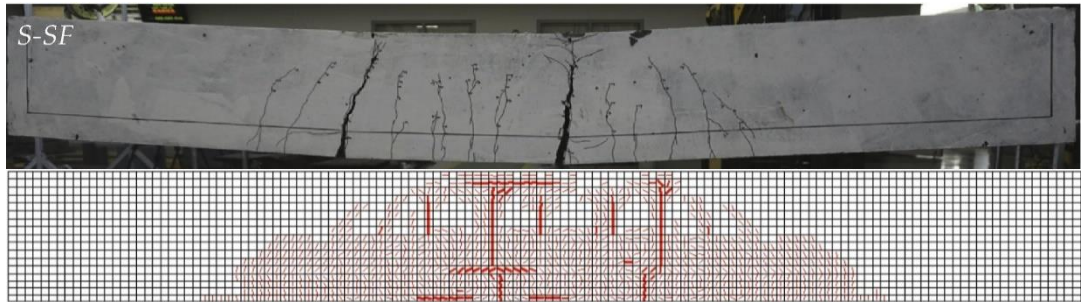


a) Small HSC beam



b) Large HSC beam

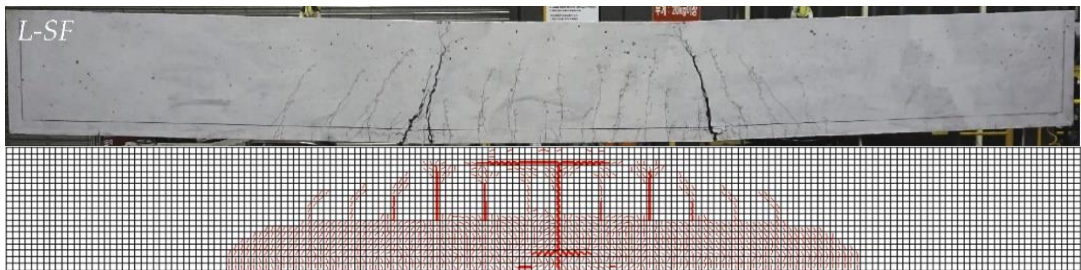
Figure 3.19: Cracking patterns at failure



c) Small SFRC beam



d) Medium SFRC beam



e) Large SFRC beam

Figure 3.19: Cracking patterns at failure (continued)

3.4.2.3 Ductility

The ductility was estimated using the Equation (3.1) as mentioned in Section 3.4.1.4. The calculated ductility indices are summarized in Table 3.8. It can be inferred from the table that the ductility indices computed from the FE analysis were generally higher than the experimental except for the small size HSC beam.

Table 3.8: Ductility Indices of the HSC and SFRC beams

Beam Specimen	Ductility Index (FE)	Ductility Index (Test)	Error (%)
S-N	7.5	11.83	36.6
S-SF	9.3	8.16	14
M-SF	7.9	7.15	10.5
L-N	8	4.91	63
L-SF	6.3	4.54	38.8

3.4.3 Comparison of Results

3.4.3.1 Load-Deflection Relationship

As seen from the Figure 3.20 to Figure 3.22, ABAQUS can predict the flexural stiffness and peak load for the three different sizes of SFRC beams accurately. However, the ultimate deflection was either underestimated (small and medium sizes) or overestimated (large size). On the other hand, Vector2 can predict the ultimate deflection accurately. However, it underestimated the peak and failure loads with a maximum error of 11%.

In the small size HSC beam, ABAQUS being more pronounced, the peak and failure loads as well as their corresponding mid-span deflections were underestimated in both numeric models, Figure 3.23. Finally, in the large size HSC beam, the analysis conducted by ABAQUS exhibited a good agreement in the pre-yield region and partial agreement in post-yield region with an underestimation of ultimate load and corresponding deflection. On the other hand, the obtained result from VecTor2 presented an overestimation of the pre-yield region and ultimate deflection.

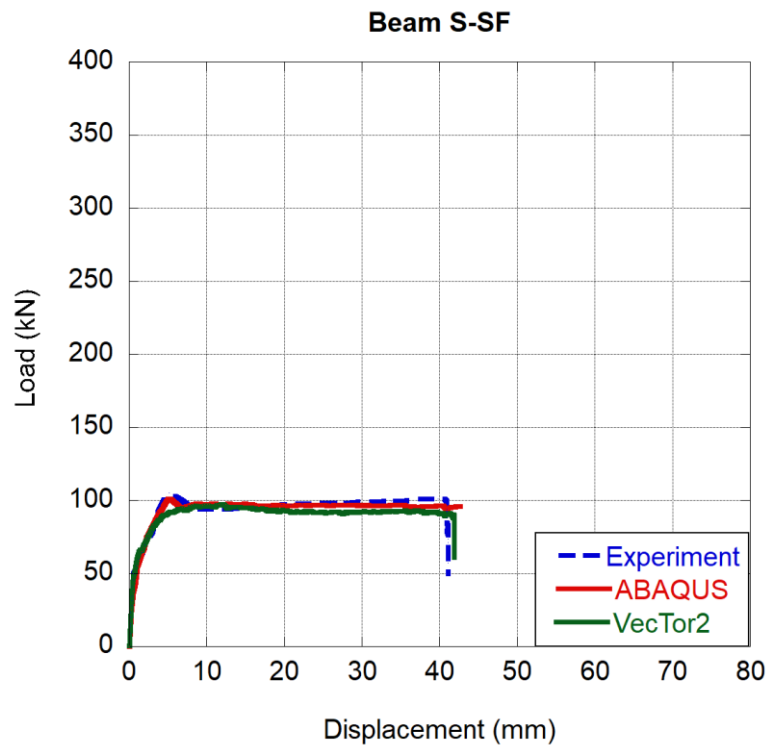


Figure 3.20: Comparison of Load-mid span deflection curves for S-SF

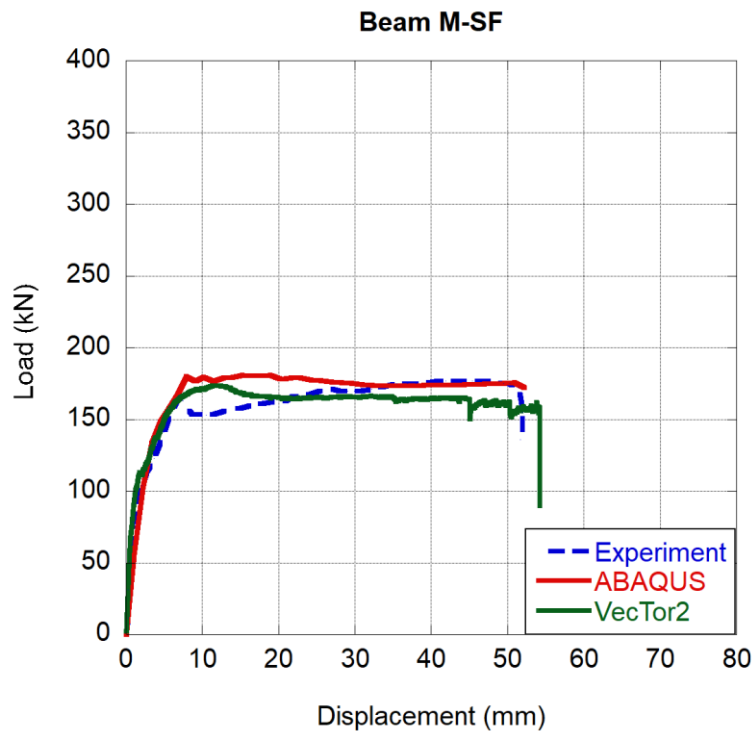


Figure 3.21: Comparison of Load-mid span deflection curves for M-SF

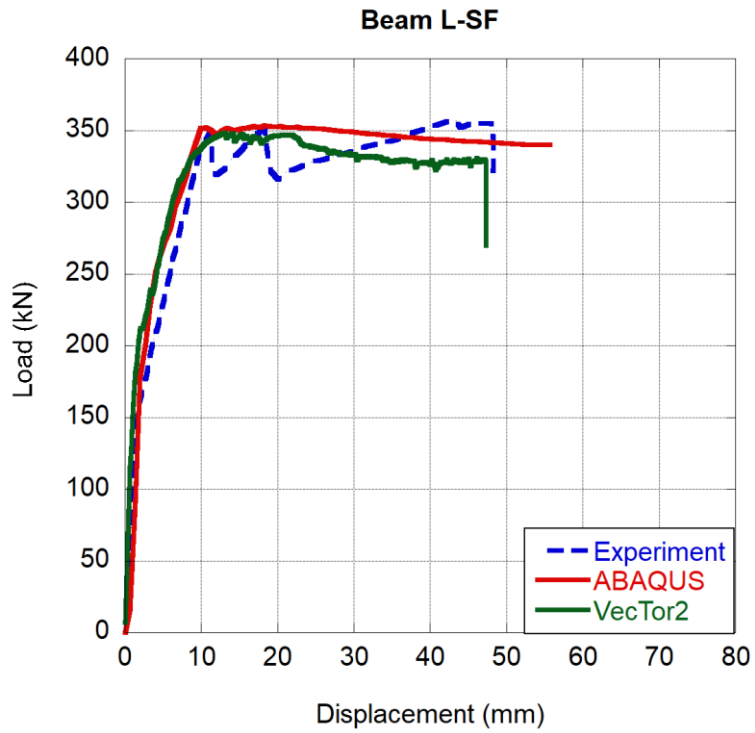


Figure 3.22: Comparison of Load-mid span deflection curves for L-SF

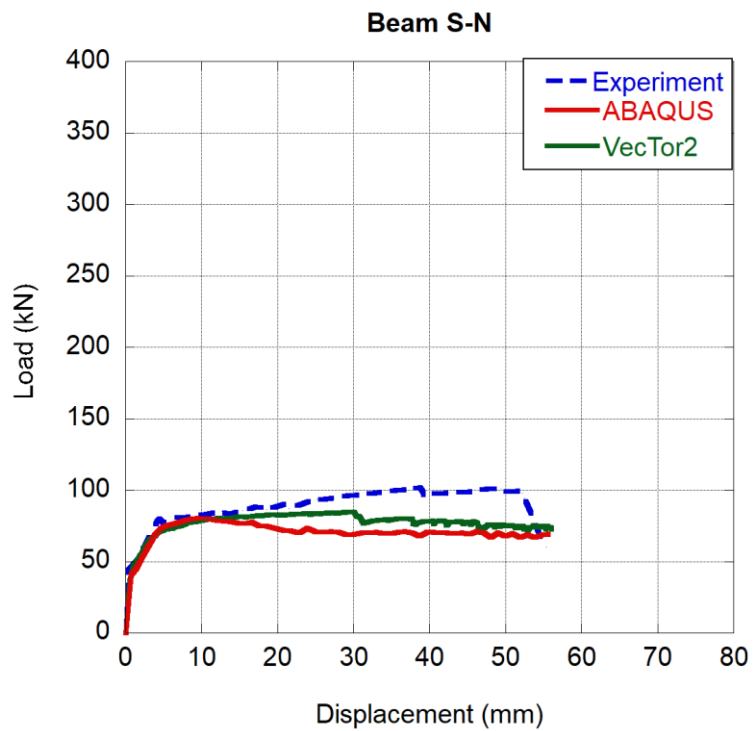


Figure 3.23: Comparison of Load-mid span deflection curves for S-N

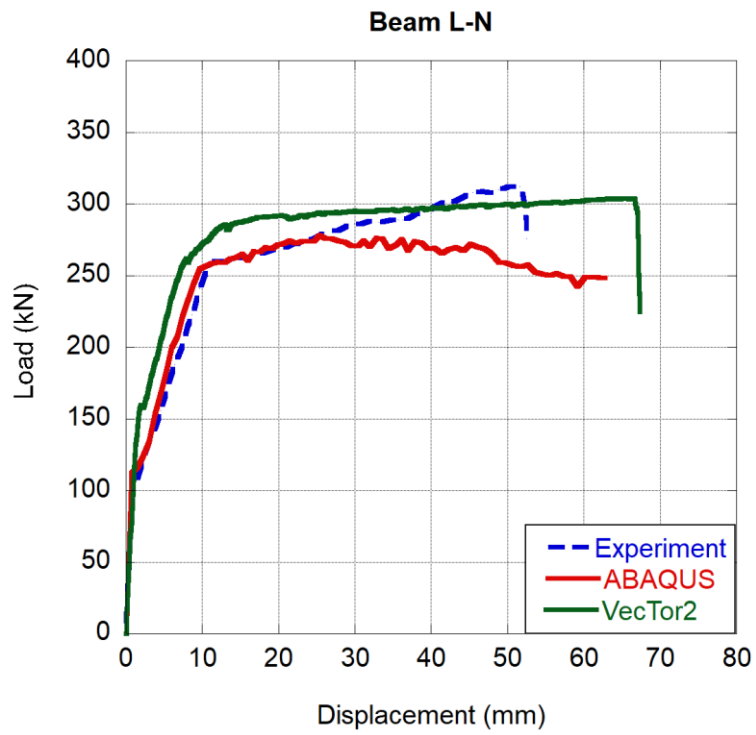


Figure 3.24: Comparison of Load-mid span deflection curves for L-N

Chapter 4

Validation of FE models on Shear Critical Beams: An Experimental Work

4.1 Introduction

This Chapter includes experimental and numerical work. Firstly, four RC beams designed to be critical in shear were produced and tested under three-point bending to investigate the possible effects of steel fiber aspect ratio on the bending behavior. One of the specimens had plain concrete with stirrups while the rest had fibrous concrete without stirrups. Once the experimental work was concluded, a numerical study was initiated to validate the FE methods on shear-critical RC beams. The FE models were established using the material properties obtained from the experimental study.

4.2 The Experimental Setup

Simply supported reinforced concrete beams are statically loaded from the mid-length of the beam by means of a hydraulic jack with a capacity of 300 kN as shown in Figure 4.1. A load cell was placed under the hydraulic jack to identify the load exerted on the beam. The mid-span deflection was obtained using a linear position transducer (LPT). In addition, the strain gauges were glued to the two tensile and compression reinforcements from the mid-length of the specimens. Therefore, the yield force could be determined. Finally, the data from these sensors was gathered through an eight-channel static data acquisition device which can retrieve data every 125 milliseconds.



Figure 4.1: Beam specimen and the sensors ready for test

4.3 Production of Test Specimens

In total four large-scale and doubly reinforced beam specimens were constructed and tested in İzmir Katip Çelebi University Structural Laboratory. All the beams had identical tensile reinforcement ratios of 1.05% and dimensions of 200 mm in width, 300 mm in height, and 2400 mm in length. One of the beams was designed to be a control specimen (B1) and had the minimum amount of transverse reinforcement based on TS500 requirements. In addition, the B1 beam did not have any fiber additive. The remaining beams (B2, B3, and B4) did not have any stirrups but instead included 0.5% hooked-end steel fibers with three different aspect ratios to assess the pure effect of hooked-end steel fiber on the shear strength. The volumetric fiber ratio was 0.5% for B2, B3, and B4 beams. A detailed technical drawing of the beams' side view and cross-section is presented in Figure 4.2.

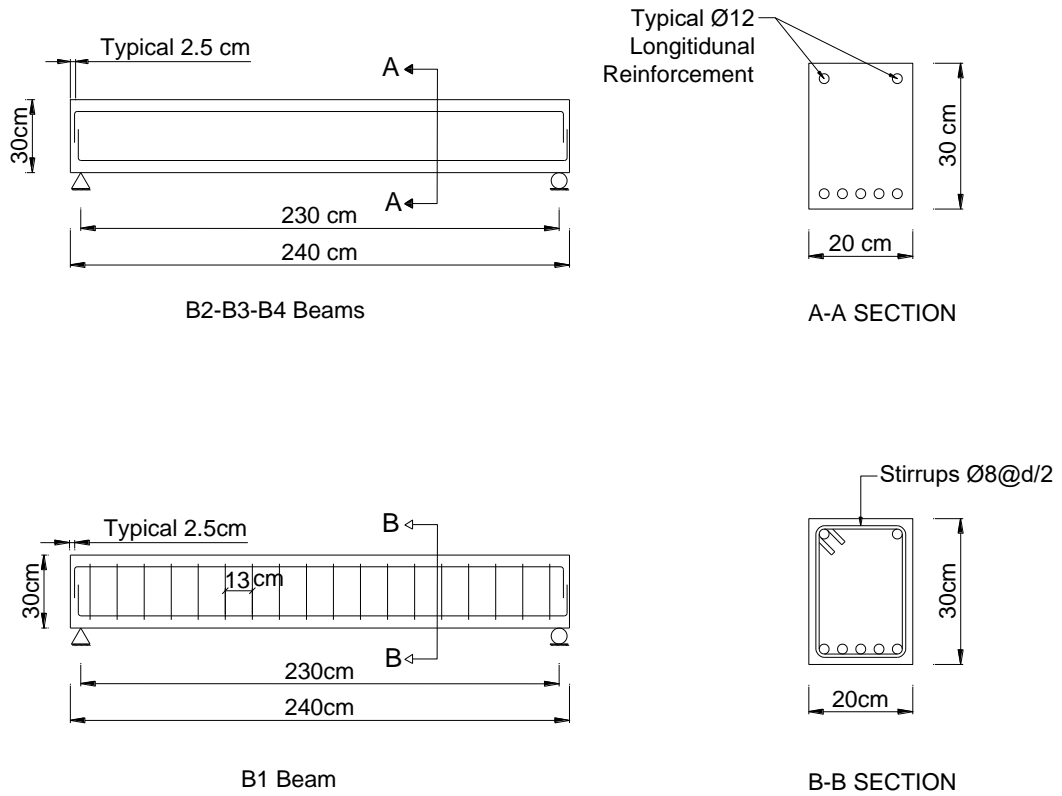


Figure 4.2: Detailing of B1, B2, B3 and B4 beams

4.4 Materials

Steel reinforcements were made of B420C-grade deformed bars. The yield and ultimate strength of the material were determined through the tension tests. Based on the test results of three 30 cm long coupons, the average yield and ultimate strengths were detected to be 500 and 670 MPa, respectively.

Concrete was ordered from a ready-mix concrete company specifying a minimum cylindrical compressive strength of 40 MPa with a 16 mm maximum aggregate size and 0.56 water/cement ratio. Using a hand mixer, the concrete and steel fibers were mixed in the previously constructed reservoirs and afterward, poured into the formworks. At least two standard cubes (15x15x15 cm) and cylinders (10x20 cm) were taken to perform compression and split tensile tests. The samples were kept by the beams and subjected to the same environmental conditions. On the test day of the beams, which is not less than 28 days, the concrete samples were tested through a hydraulic press, and the average strengths are given in Table 4.1. The strength values

of the cube samples were converted to equivalent cylinder values by multiplication of 0.85 based on [42]. Additionally, the equivalent direct tensile strength was calculated from the split tensile test as suggested in [36].

Table 4.1: The average compressive and tensile strength of concrete used in beams

<i>Beam</i>	<i>Cube Compressive Strength (MPa)</i>	<i>Equivalent Cylinder Compressive Strength (MPa)</i>	<i>Split Tensile Strength (MPa)</i>	<i>Equivalent Direct Tensile Strength (MPa)</i>
B1	48.50	41.00	3.70	2.55
B2	51.50	44.00	3.50	2.41
B3	54.90	46.50	3.85	2.65
B4	58.40	49.70	4.27	2.93

The physical and mechanical properties of utilized hooked-end steel fibers are summarized in Table 4.2.

Table 4.2: The types of fiber additives used in the beams

<i>Beam</i>	<i>Physical and mechanical properties of steel fiber</i>			
	<i>Length (mm)</i>	<i>Diameter (mm)</i>	<i>Aspect Ratio (L/D)</i>	<i>Tensile Strength (MPa)</i>
B2	60	0.9	66.7	1100
B3	60	0.75	80	1100
B4	50	1	50	1100

4.5 Results and Discussion

4.5.1 Experimental Load-Deflection Relationship

The load-displacement curves of all specimen beams were illustrated in Figure 4.3. Due to the safety concerns and limitation of hydraulic jack stroke, the experiments were stopped when the load-carrying capacity was reached. Here it should be noted that an additional FE analysis for a beam w/o stirrups and fibers was also conducted, and the obtained response is presented in Figure 4.3. As can be seen from Figure 4.3, the beam exhibits a sudden failure when the tensile reinforcements yielded. This indicates a shear-critical design of the beam section without any shear reinforcement and fibers.

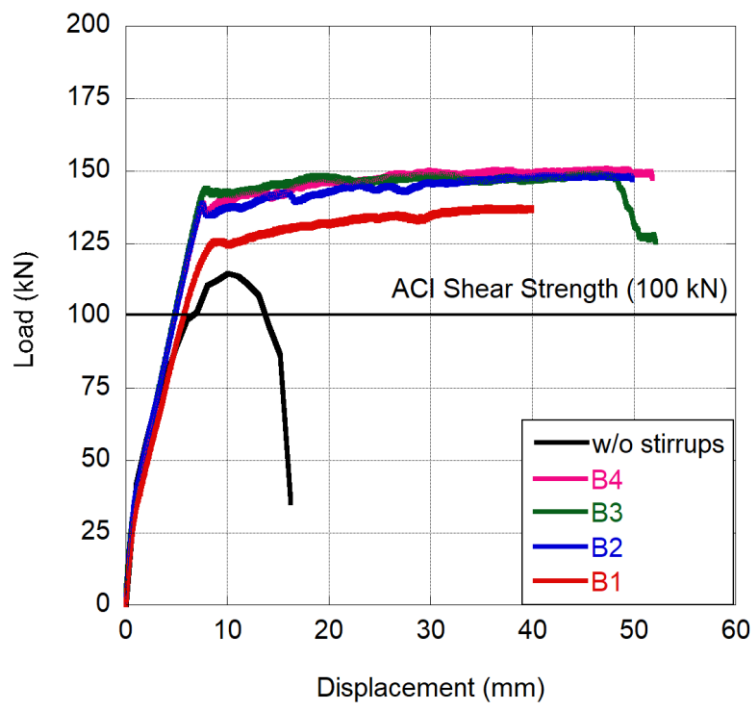


Figure 4.3: The load-displacement curve of the beam samples

Next, the B1 control beam was investigated. Introducing the minimum amount of shear reinforcement at each half-effective depth spacing shifted the beam behavior from brittle to ductile. Identically, the existence of 0.5% hooked-end steel fibers converted the behavior into ductile depending on the significantly improved shear strength. Moreover, depending on the increase in compressive strength of concrete yield load and carrying capacity enhanced as against to the beam having plain concrete w/stirrup. Yield load increased by 10 to 12% while carrying capacity enhanced by 8 to 10%. When the beams having steel fibers compared to each other, it is understood that the aspect ratio of fibers did not exhibit an obvious effect on either the pre- or post-yield behavior of the beams.

4.5.2 Predicted Response Using Plasticity Analysis (ABAQUS)

4.5.2.1 Load-Deflection Relationship

The validation process was conducted similar to Chapter 3. The FE models were developed as mentioned in Chapter 2. The load-deflection response of beams B1, B2, B3, and B4 is presented from Figure 4.4 to Figure 4.7.

First, the behavior of B1 was investigated. It could be seen from Figure 4.4 that the FE analysis predicted the load displacement of B1 precisely in the pre and post-yield regions. The error of yield and peak load was detected to be 2 and -1% respectively. On the other hand, the error of deflection corresponding to yield and peak loads was determined to be 1 and 7% respectively.

Next, beam B2 was investigated. As could be noticed from Figure 4.5 the pre-yield section was estimated accurately. However, the post-yield section exhibited a quite slight overestimation. In which, the peak and yield loads as well as their corresponding deflection values were overestimated by 3 to 4%.

In the B3 beam the pre-yield zone was predicted precisely while the post-yield region showed a slight overestimation identical to specimen B2. The exaggeration was 3 and 5% for the yield load and deflection while it was more pronounced for the peak load (8%) and its deflection (12%).

Finally, beam B4 was investigated. It could be seen from Figure 4.7 that the calculated load-displacement curve agreed quite well with that of the experimental in both pre and post-yield regions.

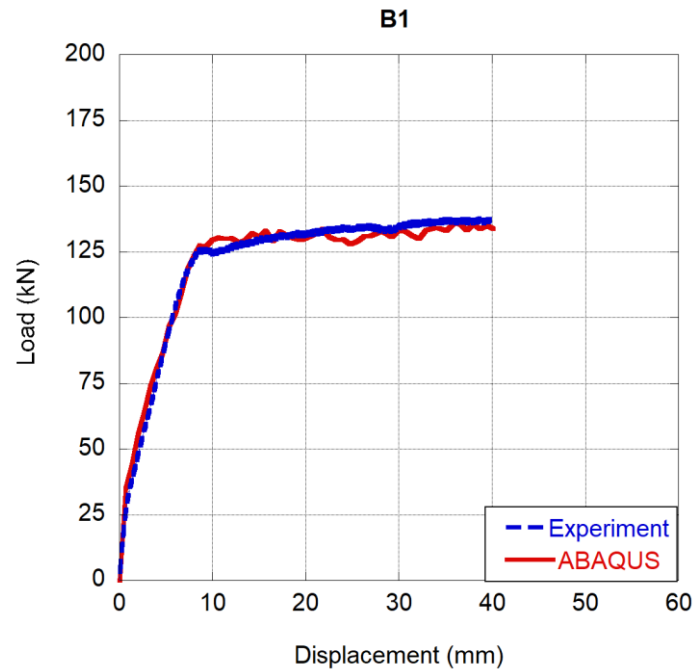


Figure 4.4: Load-displacement curve of B1 specimen

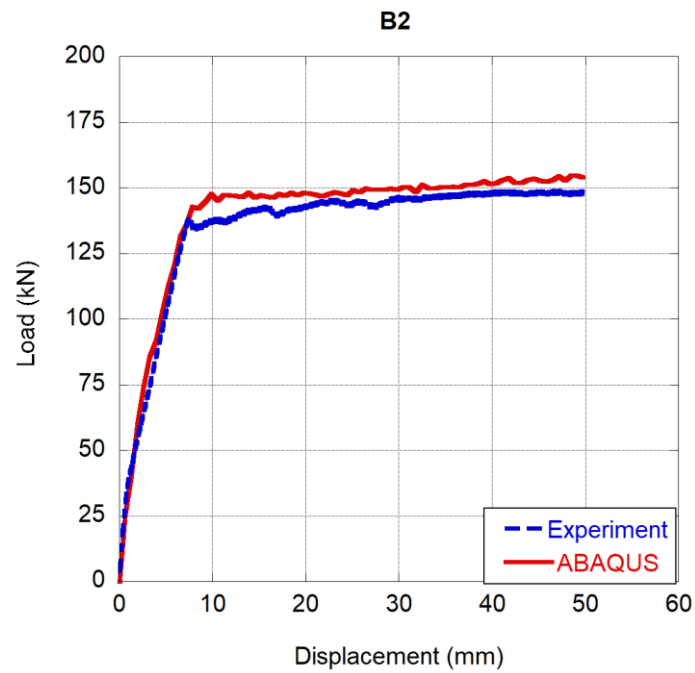


Figure 4.5: Load-displacement curve of B2 specimen

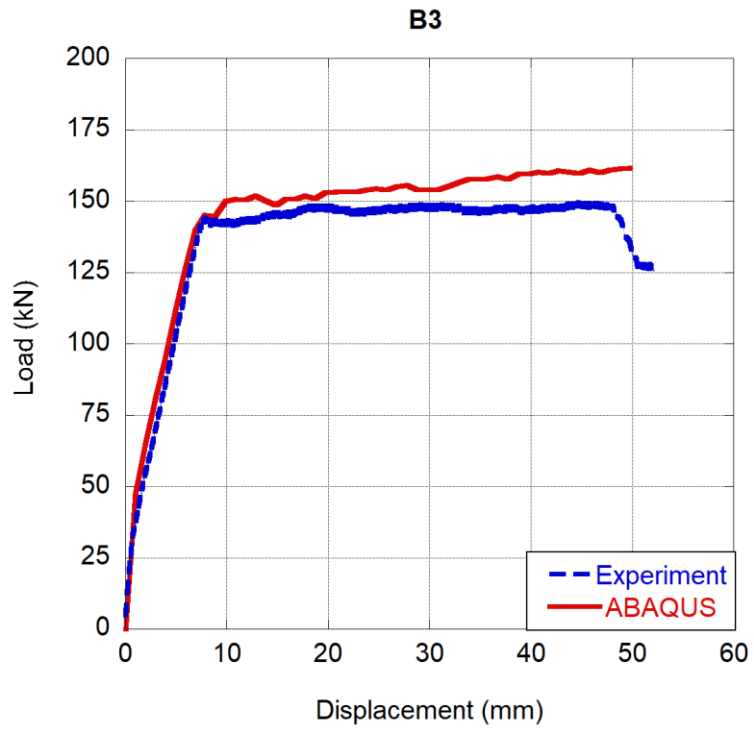


Figure 4.6: Load-displacement curve of B3 specimen

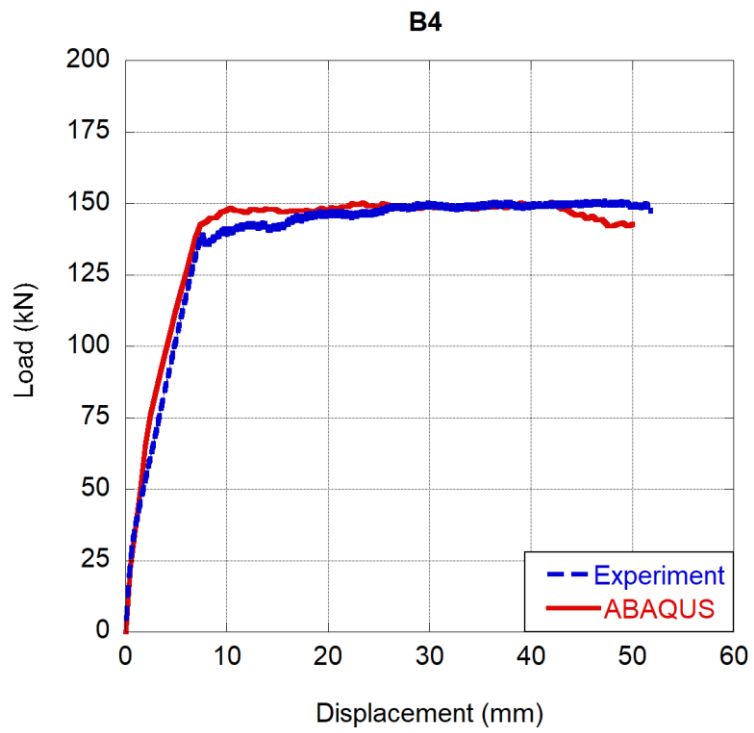
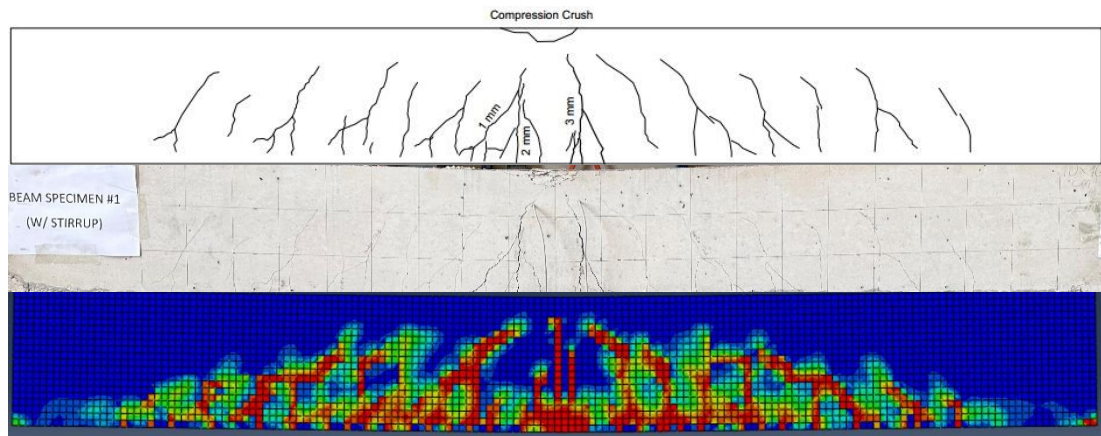


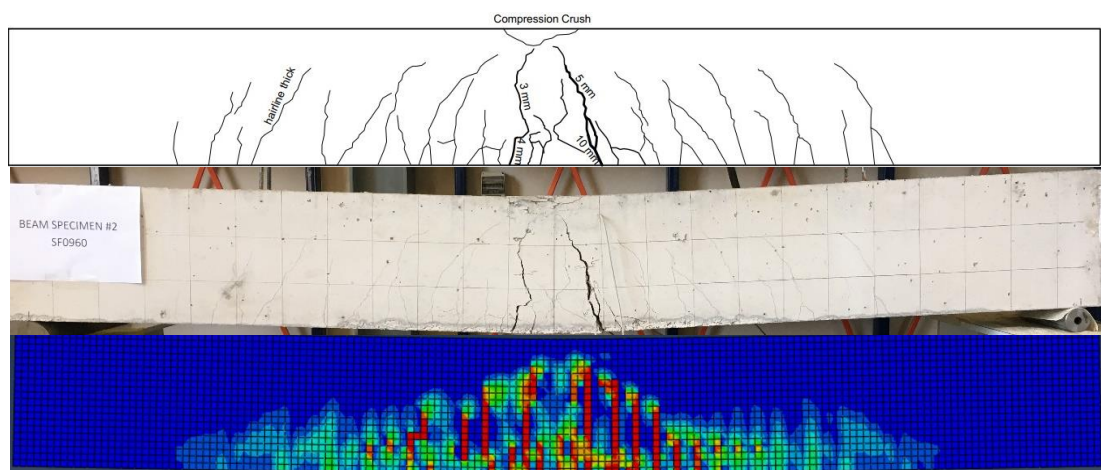
Figure 4.7: Load-displacement curve of B4 specimen

4.5.2.2 Crack Patterns

The crack pattern of experimental study was taken at capacity load (peak), while the crack pattern of numeric analysis was taken at the failure that specified as in Chapter 3. The experimental crack patterns and numerically detected damages of all specimens were presented in Figure 4.8. As can be observed from Figure 4.8, two major flexural-shear cracks formed at the maximum moment zone of all beams. The width of cracks reached up to 10 mm and hairline thick flexural-shear cracks were also observed to be distributed along the beams. On the other hand, numerically detected damage patterns could reveal the highest damage occurring approximately in the maximum moment region while the remaining portion of the beams was assessed to be lightly damaged.

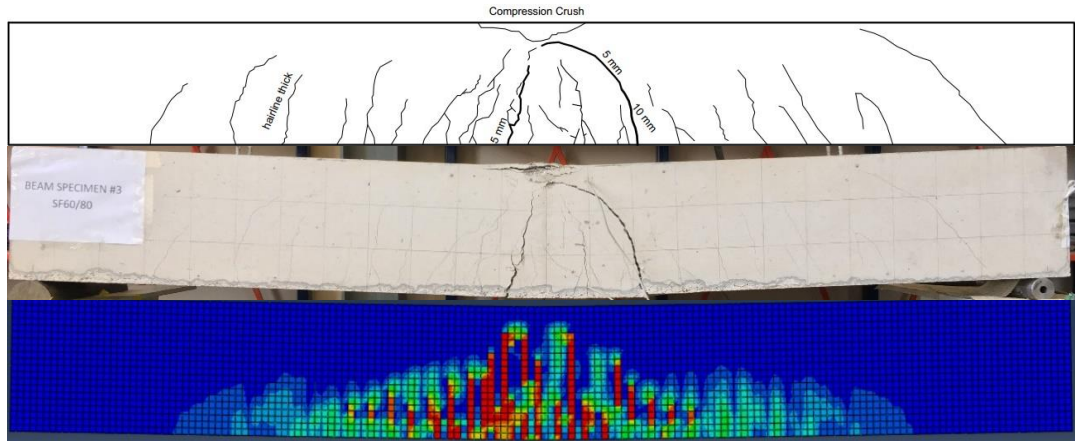


a) B1

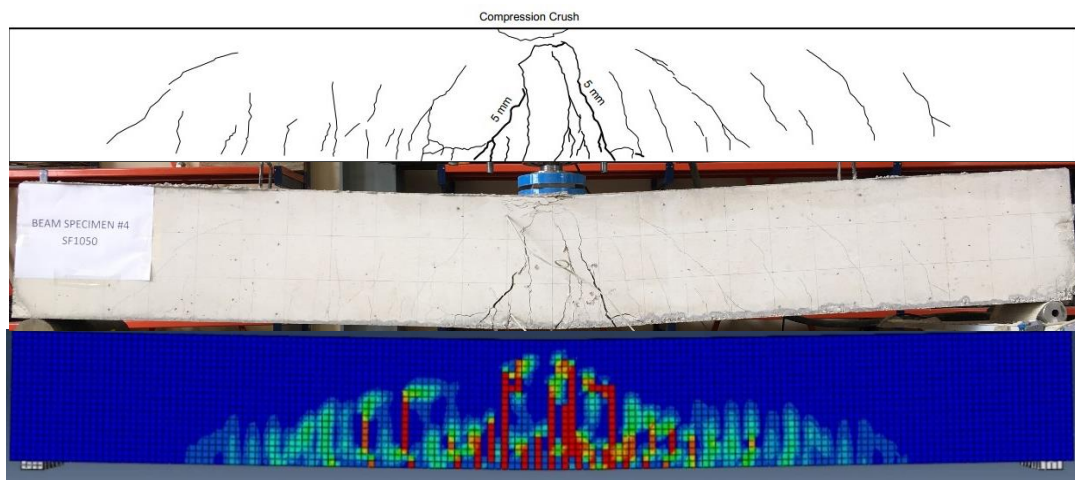


b) B2

Figure 4.8: Experimentally obtained crack patterns and numerically captured damages



c) B3



d) B4

Figure 4.8: Experimentally obtained crack patterns and numerically captured damages (continued)

4.5.2.3 Ductility

In this section, due to unavailability of the failure deflection the ductility index was calculated using Equation (4.1) where Δ_p and Δ_y are the deflection corresponding to load at peak and yield respectively. Existence of either steel fibers or minimum amount of stirrups converted the behavior into ductile. However, the beams having fibrous concrete performed 40% higher ductility performance in average as could be understood from Table 4.3. Those beams had almost identical ductility indexes in the vicinity of 6 despite the different aspect ratios of steel fibers. On the other hand, the

results of the FE analysis generally agreed well with the tested results, in which the fibrous concrete specimens had higher ductility index than the control specimen.

$$\mu_p = \frac{\Delta_p}{\Delta_y} \quad (4.1)$$

Table 4.3: Experimental and numerical ductility Indices of the beams

Beam Specimen	Ductility Index (Test)	Ductility Index (FE)	Error %
B1	4.5	4.2	6.7
B2	6.3	6.2	1.6
B3	6	6.4	6.7
B4	6.4	5.7	10.9

4.5.3 Predicted Response Using MCTF Analysis (VecTor2)

4.5.3.1 Load-Deflection Relationship

The numerical simulation was modelled using the identical constitutive relationships defined in Chapter 2. The load displacement curve of specimen B1 was presented in Figure 4.9. Flexural stiffness was calculated slightly higher than that of experimental. Yield and peak loads were significantly overestimated in the analysis, 9 and 20%, respectively. The corresponding deflections were detected with -21% and -19% errors.

When the response of beams having fibrous concrete is investigated, it can be expressed that the flexural stiffness and yield load could be captured quite well by the MCTF-based analysis, Figure 4.10 to Figure 4.12. However, post-yield behavior exhibited discrepancies for all shear critical SFRC beams. For example, 7.5 to 14% exaggerations were computed for the peak load while the error in its deflection varied between -38 and -52%.

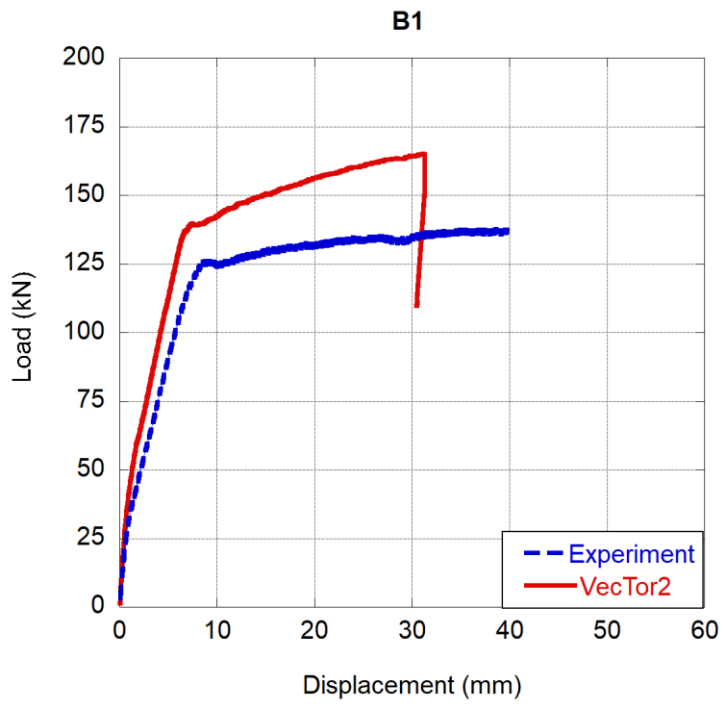


Figure 4.9: Load-displacement curve of specimen B1

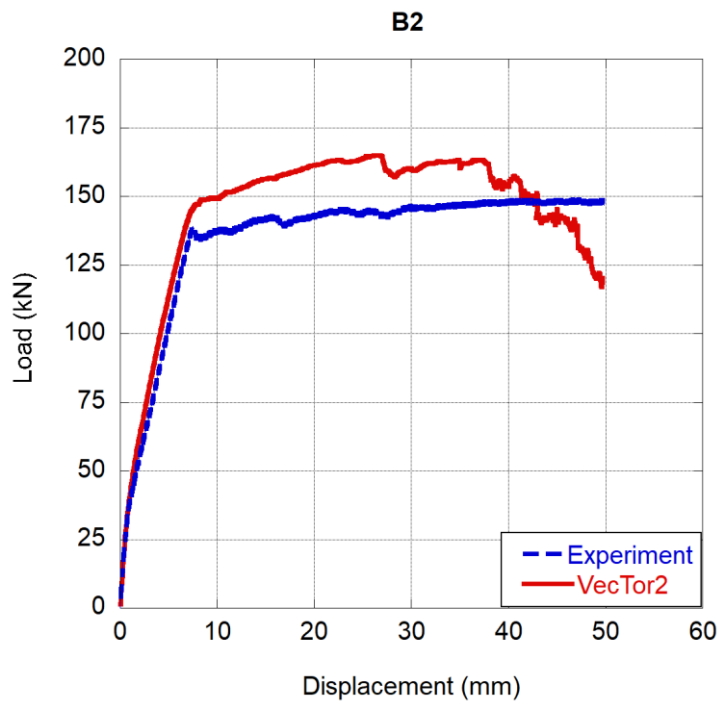


Figure 4.10: Load-displacement curve of specimen B2

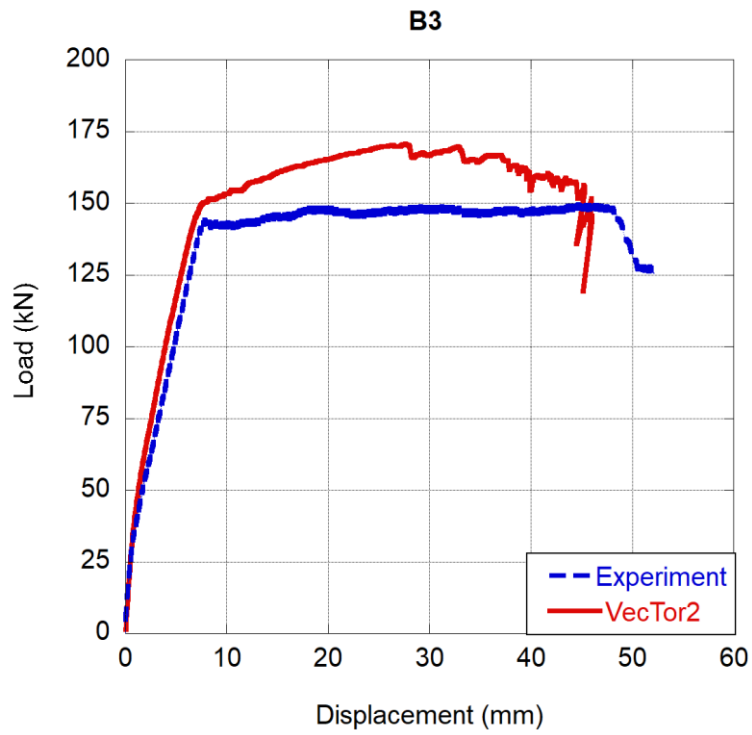


Figure 4.11: Load-displacement curve of specimen B3

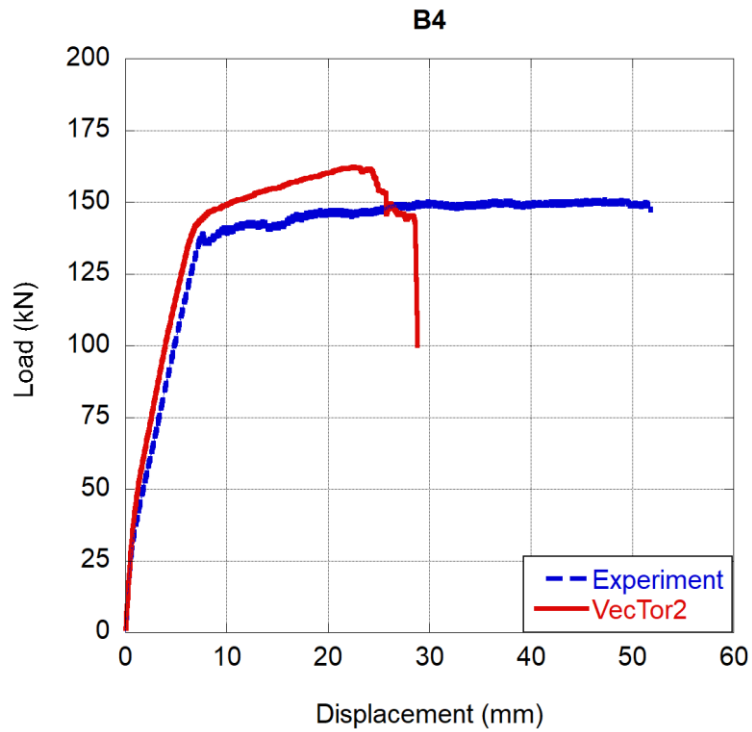
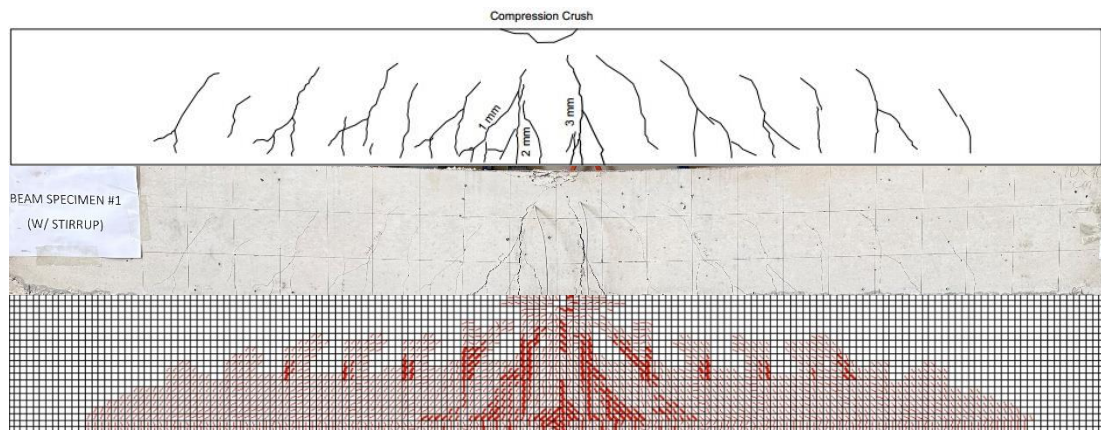


Figure 4.12: Load-displacement curve of specimen B4

4.5.3.2 Crack Patterns

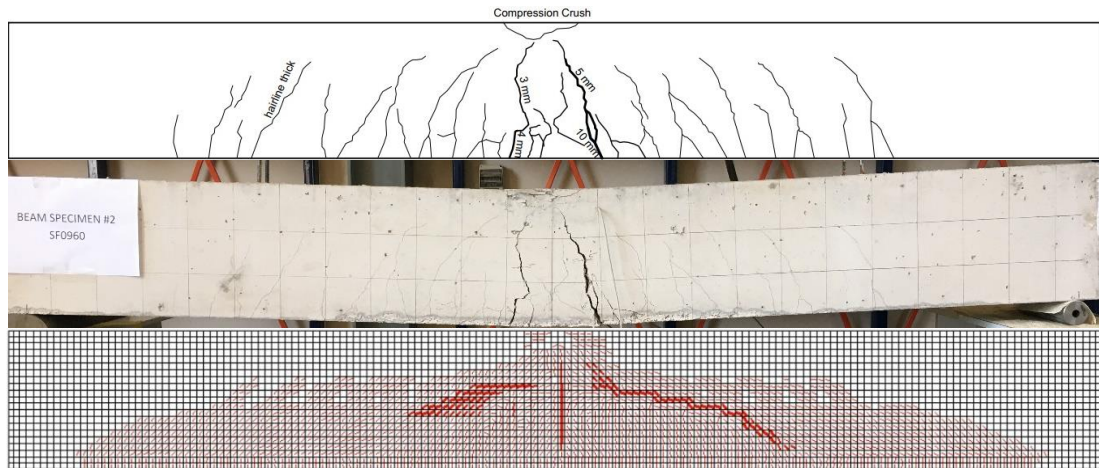
As mentioned previously the crack pattern of experimental study was taken at capacity load (peak). However, the crack pattern of numeric analysis was taken at the failure state as specified in Chapter 3. In the analyses, none of the beams failed owing to rebar rupture. In fact, a numerical failure initiated when the net principal compressive strain exceeded 0.003 and 0.01 for the beams without and with fiber, respectively, and large shear cracks formed concurrently in the fibrous beams.

VecTor2 predicted two major flexural cracks truly in the loading cone of the B1 beam. In addition, the hairline thick flexural-shear cracks distributed almost along the length of the beam, Figure 4.13 (a). However, though those type of cracks (hairline thick flexural-shear cracks) were also observed in the experiment, they were not as densely distributed as the numerical analysis. The crack patterns of the beams having fibrous concrete clearly occurred in shear form Figure 4.13 (b, c, and d). Furthermore, the concrete crush was also revealed.

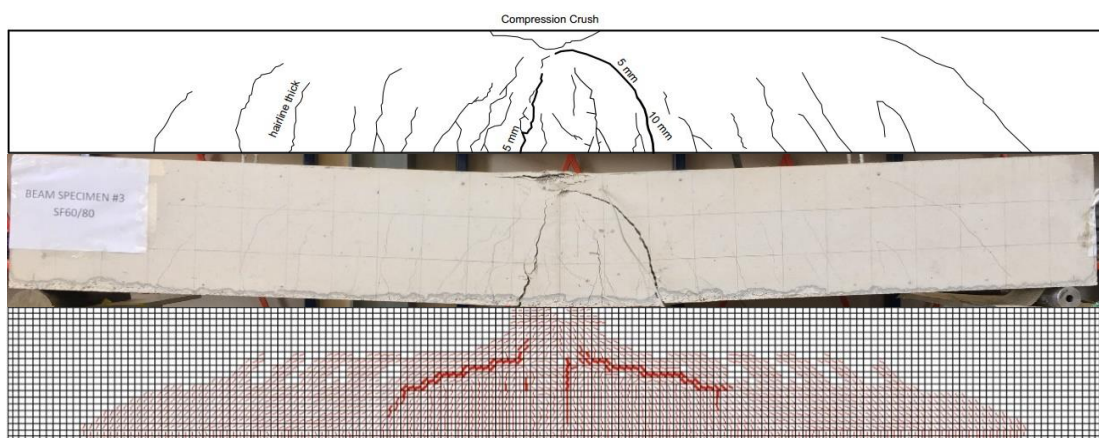


a) B1

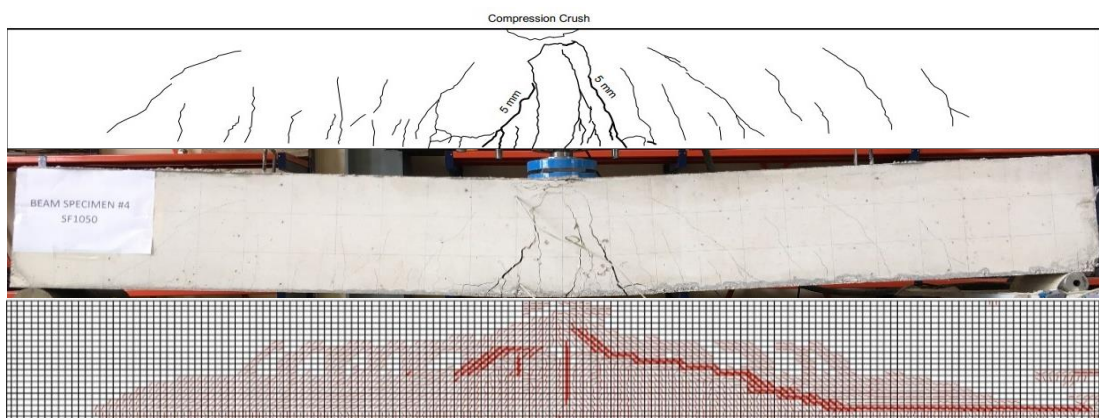
Figure 4.13: Experimentally and numerically obtained crack patterns of plain and fibrous concrete beams



b) B2



c) B3



d) B4

Figure 4.13: Experimentally and numerically obtained crack patterns of plain and fibrous concrete beams (continued)

4.5.3.3 Ductility

The ductility was calculated using the Equation (4.1) as mentioned in Section 4.5.2.3 with respect to peak load. This occurred relatively earlier deformation level compared to the experiments. Therefore, except B1 beam, ductility index of rest of the specimens were computed to be lower as noted in Table 4.4.

Table 4.4: Calculated ductility indices of the beams

Beam Specimen	Ductility Index (Test)	Ductility Index (FE)	Error %
B1	4.5	4.6	2.2
B2	6.3	3.7	41.3
B3	6	4	33.3
B4	6.4	3.3	48.4

4.5.4 Comparison of Results

4.5.4.1 Load-Deflection Relationship

As seen from the Figure 4.14 to Figure 4.17, ABAQUS can predict the flexural stiffness and peak load for all the beams accurately. However, the peak deflection was calculated with a maximum error of 12%. On the other hand, Vector2 estimated the deflection corresponding to peak load up to 52% lower. Moreover, it overestimated the peak load by 20% for the B1 beam and by a maximum of 14% for the fibrous beams.

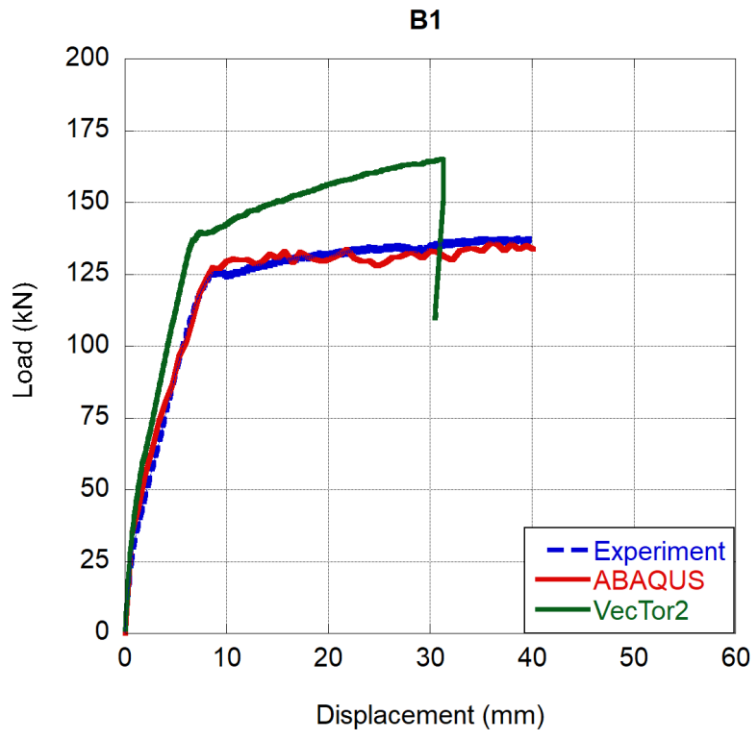


Figure 4.14: Comparison of Load-mid span deflection curves for B1

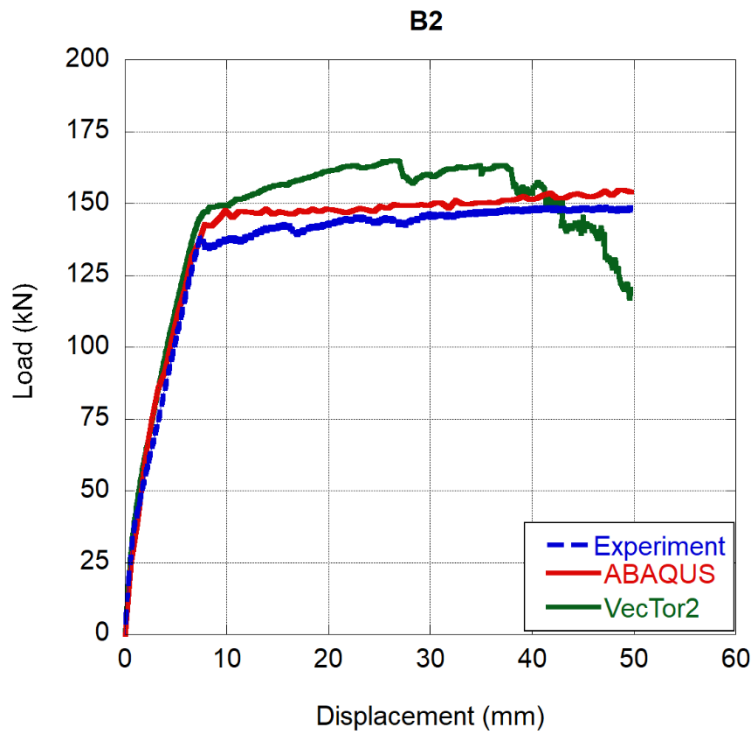


Figure 4.15: Comparison of Load-mid span deflection curves for B2

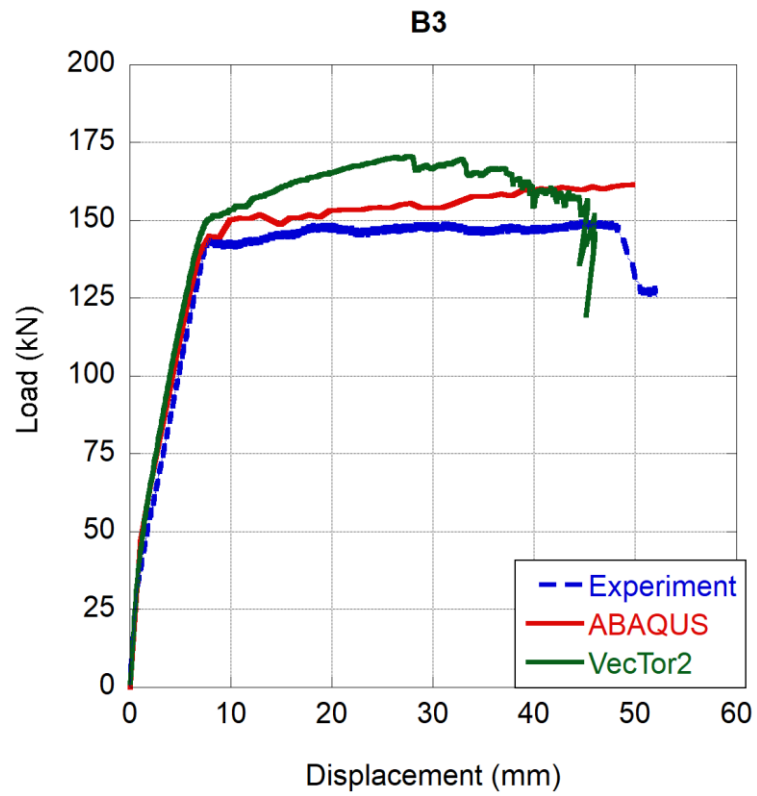


Figure 4.16: Comparison of Load-mid span deflection curves for B3

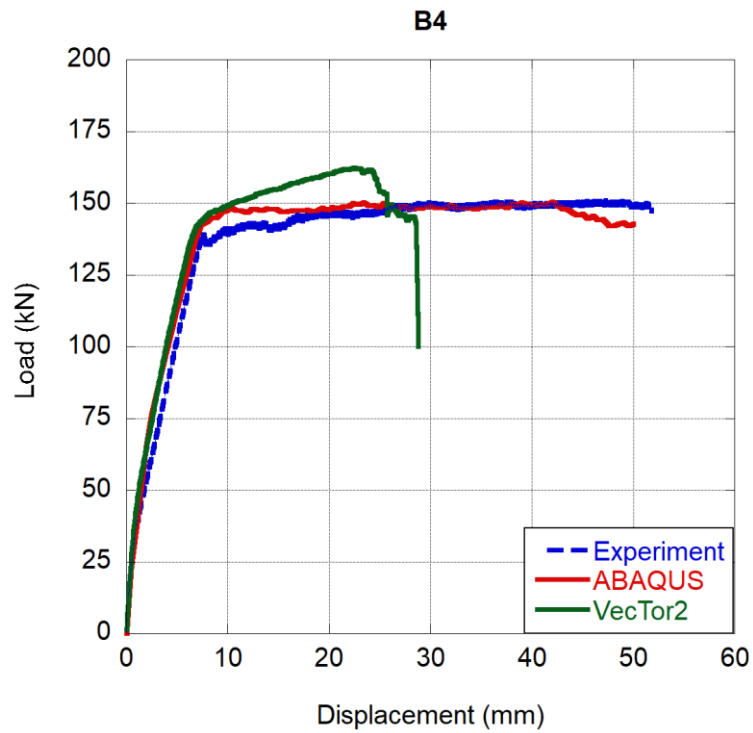


Figure 4.17: Comparison of Load-mid span deflection curves for B4

Chapter 5

Conclusion

A numerical and experimental study was conducted on the bending behavior of beams with and without steel fibers. The main objective of this study was to investigate the ability and accuracy of CDP model and MCTF formulations in reflecting the behavior of the RC beams. For this purpose, two groups of beams were used. The beams in the first group were selected from literature and were critical against flexure. However, the second group beams were designed to be critical in shear and constructed and tested in the laboratory.

In the selected study five beams existed of different sizes. The volumetric steel fiber ratio kept constant as 0.75% in the three fibrous beams. Tensile reinforcement ratios were 0.64, 0.65 and 0.72%. On the other hand, the conducted experimental study had four beams with dimensions of 2400x300x200 mm. The fibrous beams were designed using steel fibers of varying aspect ratios and the volume of fiber ratio kept constant as 0.5%. The tensile reinforcement ratio was uniformly set at 1.05% in all beams. Based on the discussions and obtained results above, the following conclusions can be drawn:

a) Findings from the experimental study are listed below:

- The presence of 0.5% steel fiber in the RC beams with a 1.05% tensile reinforcement ratio which is leading a shear critical section converted the behavior from sudden and brittle failure to ductile type identical to the beams with minimum amount stirrup based on TS500.
- The inclusion of 0.5% steel fiber into the concrete increased the compressive strength of material. Consequently, the yield and peak loads were enhanced by

10% approximately compared to the beam having minimum amount of stirrup but without fibers.

- Utilization of different aspect ratios of steel fiber did not exert a pronounced effect on the bending behavior of RC beams.
- The crack patterns observed in SFRC beams were found to be almost identical to those in RC beam with stirrups.

b) Findings from the numerical study are as follows:

- Using the general contact explicit in the CDP model resulted in more accurate member response when compared to the tie contact, despite slightly increased computational time.
- The choice of tension stiffening model had a significant role in obtaining the true load-displacement curve. Implementation of the FIB Model Code 2010 overestimated the post-yield region due to its high fracture energy. Contrary, application of the SDEM model yielded more precise results in the pre- and post-yield regions.
- The load-deflection curves obtained through the employment of MCFT formulations provide accurate estimation of flexural rigidity for both types of SFRC beams. When it comes to HSC beams without fibers, an overestimation was made except the small size flexural critical beam.
- The MCFT formulations demonstrated considerable accuracy in predicting the general trend of the load-deflection curve for flexure critical beams; however, it exhibited limitations in effectively capturing the behavior of shear-critical beams.
- The MCFT formulations captured the major flexural cracks located in the maximum moment region for both flexural and shear-critical designs of high-strength concrete (HSC) beams without fibers. The crack patterns of beams with fibers could be partially detected.
- CDP model could capture the flexural rigidity, overall trend of load-deflection curve and damages excellently without exception for all types of beams.

References

- [1] ACI Committee 544.1-96, “Report on fiber reinforced concrete”. American Concrete Institute. 1996.
- [2] S. J. Foster. “The application of steel-fibers as concrete reinforcement in Australia: from material to structure”. *Materials and Structures*, 42:1209–1220, 2009.
- [3] R. J. Craig, J. Decker, L. Dombrowski, R. Laurencelle, and J. Federovich. “Inelastic behavior of reinforced fibrous concrete”. *Journal of Structural Engineering*, 113(4): 802–817, 1987.
- [4] R. N. Swamy, S. Al-Ta'an, and Sami A. R. A. “Steel fibers for controlling cracking and deflection”. *Concrete International*, 1:41–49, 1979.
- [5] A. Bentur, S. Mindess. “Concrete beams reinforced with conventional steel bars and steel fibers: properties in static loading”. *The International Journal of Cement Composites and Lightweight Concrete*. 5(3): 199–202, 1983.
- [6] S. M. F. Mahmood, A. Agarwal, S. J. Foster, and H. Valipour. “Flexural performance of steel fiber reinforced concrete beams designed for moment redistribution”. *Engineering Structures*. 177: 695-706, 2018.
- [7] H. V. Dwarakanath, T. S. Nagaraj. “Deformational behavior of reinforced fiber reinforced concrete beams in bending”. *Journal of Structural Engineering*. 118(10): 2691–2698, 1992.
- [8] L. Vandewalle. “Cracking behavior of concrete beams reinforced with a combination of ordinary reinforcement and steel fibers”. *Materials and Structures*. 33:164–170, 2000.

- [9] B. H. Oh. “Flexural analysis of reinforced concrete beams containing steel fibers”. *Journal of Structural Engineering*. 118(10): 2821–2835, 1992.
- [10] F. Altun, T. Haktanir, K. Ari. “Effects of steel fiber addition on mechanical properties of concrete and RC beams”. *Construction and Building Materials*. 21: 654–661, 2007.
- [11] H. C. Mertol, E. Baran, and H. J. Bello. “Flexural behavior of lightly and heavily reinforced steel fiber concrete beams. *Construction and Building Materials*. 98: 185–193, 2015.
- [12] M. A. Cankaya and C. Akan. “An experimental and numerical investigation on the bending behavior of fiber reinforced concrete beams”. *Turkish Journal of Civil Engineering*, 34(1): 59-78, 2023.
- [13] M. Singh, A. H. Sheikh, M. S. Mohamed Ali, P. Visintin, and M. C. Griffith. “Experimental and numerical study of the flexural behavior of ultra-high performance fiber reinforced concrete beams”. *Construction and Building Materials*. 138: 12-25, 2017.
- [14] A. Earij, G. Alfano, K. Cashel, and X. Zhou. “Nonlinear three-dimensional finite-element modelling of reinforced-concrete beams: computational challenges and experimental validation”. *Engineering Failure Analysis*, 82: 92-115, 2017.
- [15] D. Y. Yoo, T. Yuan, J. M. Yang, and Y. S. Yoon. “Feasibility of replacing minimum shear reinforcement with steel fibers for sustainable high-strength concrete beams”. *Engineering Structures*. 147: 207-222, 2017.
- [16] D. Y. Yoo, and Y. S. Yoon. “Structural performance of ultra-high-performance concrete beams with different steel fibers”. *Engineering Structures*. 102: 409-423, 2015.
- [17] A. Meda, F. Minelli, and G. A. Plizzari. “Flexural behavior of RC beams in fiber reinforced concrete”. *Composites: Part B*. 43: 2930-2937, 2012.

- [18] I. H. Yang, C. Joh, and B. S. Kim. "Structural behavior of ultra-high performance concrete beams subjected to bending". *Engineering Structures*. 32: 3478-3487, 2010.
- [19] S. A. Ashour, F. F. Wafa, and M. I. Kamal. "Effect of the concrete compressive strength and tensile reinforcement ratio on the flexural behavior of fibrous concrete beams". *Engineering Structures*, 22: 1145–58, 2000.
- [20] S. C. Lee, J. Y. Cho, and F. J. Vecchio. "Diverse embedment model for steel fiber-reinforced concrete in tension: model verification". *ACI Materials Journal*. 108(5): 526-535, 2011.
- [21] S. C. Lee, J. Y. Cho, and F. J. Vecchio. "Simplified diverse embedment model for steel fiber reinforced concrete elements in tension". *ACI Materials Journal*. 110(4): 403-412, 2013.
- [22] S. C. Lee, J. H. Oh, and J. Y. Cho. "Compressive behavior of fiber-reinforced concrete with end-hooked steel fibers". *Materials*. 8(4): 1442-1458, 2015.
- [23] F. J. Vecchio and M. P. Collins. "The Modified compression-field theory for reinforced concrete elements subjected to shear". *ACI Journal*, 83(2): 219-231, 1986.
- [24] D. Mitchell and M. P. Collins. "Diagonal compression field theory- a rational model for structural concrete in pure torsion". *ACI Journal Proceedings*, 71(8): 396-408, 1974.
- [25] P. S. Wong, F. J. Vecchio and H. Trommels. *Vector2 & FormWorks User's Manual*, 2002.
- [26] Lubliner J., Oliver J., Oller S. and Onate E. "A plastic-damage model of concrete." *International Journal of Solids and Structures*, 25(3), 299-326., (1989).
- [27] Lee J. and Fenvers G. L. "Plastic-damage model for cyclic loading of concrete structures." *Journal of Engineering Mechanics*, 124(8), 892-900, (1998).

- [28] Hibbitt, Karlsson and Sorensen. ABAQUS analysis manual version 6.14, “23.6.3 Concrete damaged plasticity”. INC, Warrington, Cheshire, 2000.
- [29] Yu T, Teng JG, Wong YL, Dong SL. “Finite element modeling of confined concrete—II: Plastic-damage model”. *Engineering Structures*, 32(3), 680-691, 2010.
- [30] Goran H. M., Zhenjun Y., and Aram M. T. H. “Experimental and numerical studies of size effects of ultra-high performance steel fiber reinforced concrete (UHPRFC) beams.” *Construction and Building Materials*, 48, 1027-1034, 2013.
- [31] Hillerborg A., Modeer M. and Petersson P. E. “Analysis of crack formation and crack growth in concrete by means of fracture mechanics and finite elements.” *Cement and Concrete Research*, 6, 773-782, 1976.
- [32] CEB Bulletin No. 213/214, “CEB-FIP model code 90”. 1991.
- [33] Sandor Popovics. “A Numerical approach to the complete stress-strain curve of concrete.” *Cement and Concrete Research*, 3(5), 583-599, 1973.
- [34] Kent D. C., Park R. “Flexural members with confined concrete”. *Journal of the Structural Division*, 97(7), 1969-1990, 1971.
- [35] Hordijk DA. “Local approach to fatigue of concrete”. Delft University of Technology. Delft. 1991.
- [36] U. Ersoy, G. Özcebe and T. Tankut. “Reinforced concrete”. METU Press, Ankara, 2016.
- [37] TBEC, “Turkish Building Earthquake Code”. Afet ve Acil Durum Yönetimi Başkanlığı, Resmi Gazete, 2018.
- [38] ACI Committee 318. Building code requirements for structural concrete (ACI 318-14) and commentary (318R-14). Farmington Hills: American Concrete Institute. 2014.
- [39] B. G. Rabbat, M. ASCE, and H. G. Russell. “Friction coefficient of steel on concrete or grout”. *Journal of Structural Engineering*. 111(3):505-515, 1985.

- [40] Fib Bulletin No.55. Model Code 2010. 2010
- [41] American Concrete Institute (ACI) 544.4R-18, 2018. Guide to Design with Fiber-Reinforced Concrete. Michigan, USA.
- [42] TS EN 206, Concrete – Specification, performance, production and conformity, Turkish Standard Institute, Ankara, 2014.

Appendices

Appendix A

Tabularization of Numerically Calculated and Experimentally Obtained Load, Deflection and Error Data

- Flexural Critic Beams: Yoo et. al. (2017), the table below lists the obtained experimental and numerical (ABAQUS) data. P_{cr} , P_{yield} , Δ_{cr} , and Δ_{yield} standing for the cracking, yielding load and their corresponding deflection values.

	P_{cr} (kN)			Δ_{cr} (mm)			P_{yield} (kN)			Δ_{yield} (mm)		
	Exp.	Num.	Error (%)	Exp.	Num.	Error (%)	Exp.	Num.	Error (%)	Exp.	Num.	Error (%)
<i>S-N</i>	44.2	40.9	7.5	0.72	0.8	11.1	80.6	68.6	14.9	4.58	3.8	17
<i>S-SF</i>	50.3	59.2	17.7	0.74	1.4	89.2	105.4	101	4.2	5	5	0
<i>M-SF</i>	78.1	133.7	71.2	0.88	3.4	286.4	168.7	167.7	0.6	7.2	6.7	6.9
<i>L-N</i>	109.6	112.1	2.3	1.04	0.72	30.8	255.3	221.6	13.2	10.5	7.4	29.5
<i>L-SF</i>	114.8	177.9	55	1.00	2	100	317.6	330.7	4.1	10.6	8.6	18.9

- Flexural Critic Beams: Yoo et. al. (2017), the table below lists the obtained experimental and numerical (ABAQUS) data. P_p , P_{ult} , Δ_p , and Δ_{ult} standing for the peak, ultimate load and their corresponding deflection values.

	P_p (kN)			Δ_p (mm)			P_{ult} (kN)			Δ_{ult} (mm)		
	Exp.	Num.	Error (%)	Exp.	Num.	Error (%)	Exp.	Num.	Error (%)	Exp.	Num.	Error (%)
<i>S-N</i>	102.3	80.7	21.1	38.7	9.5	75.5	97.6	73.5	24.7	52.1	23.9	54.1
<i>S-SF</i>	107.3	101.1	5.8	5.54	5.3	4.3	101	96.8	4.2	40.8	30	26.5
<i>M-SF</i>	176.1	180.9	2.7	41.7	15.2	63.5	165	173.6	5.2	51.5	36.3	29.5
<i>L-N</i>	312.9	278.2	11.1	51.3	25.4	50.5	312	230	26.3	51.6	62.8	21.7
<i>L-SF</i>	352.0	353.5	0.4	42.8	18.3	57.2	355	341.2	3.9	48.1	55.6	15.6

- Flexural Critic Beams: Yoo et. al. (2017), the table below lists the obtained experimental and numerical (VecTor2) data. P_{cr} , P_{yield} , Δ_{cr} , and Δ_{yield} standing for the cracking, yielding load and their corresponding deflection values.

	P_{cr} (kN)			Δ_{cr} (mm)			P_{yield} (kN)			Δ_{yield} (mm)		
	Exp.	Num.	Error (%)	Exp.	Num.	Error (%)	Exp.	Num.	Error (%)	Exp.	Num.	Error (%)
<i>S-N</i>	44.2	44.8	1.36	0.72	0.9	25	80.6	69.2	14.1	4.58	4	12.7
<i>S-SF</i>	50.3	66	31.2	0.74	1.4	89.2	105.4	89.6	15	5	4.4	12
<i>M-SF</i>	78.1	86	10.1	0.88	0.9	2.3	168.7	164	2.8	7.2	6.8	5.6
<i>L-N</i>	109.6	159.8	45.8	1.04	2	92.3	255.3	261.8	2.55	10.5	8.3	21
<i>L-SF</i>	114.8	174.4	51.9	1.00	1.3	30	317.6	317.3	0.1	10.6	7.5	29.2

- Flexural Critic Beams: Yoo et. al. (2017), the table below lists the obtained experimental and numerical (VecTor2) data. P_p , P_{ult} , Δ_p , and Δ_{ult} standing for the peak, ultimate load and their corresponding deflection values.

	P_p (kN)			Δ_p (mm)			P_{ult} (kN)			Δ_{ult} (mm)		
	Exp.	Num.	Error (%)	Exp.	Num.	Error (%)	Exp.	Num.	Error (%)	Exp.	Num.	Error (%)
<i>S-N</i>	102.3	84.9	17	38.7	29.5	23.8	97.6	83.7	14.2	52.1	29.9	42.6
<i>S-SF</i>	107.3	97.3	9.3	5.5	12	118.2	101	90.8	11.2	40.8	41	0.5
<i>M-SF</i>	176.1	173.8	1.3	41.7	11.6	72.2	165	158.8	3.8	51.5	53.7	4.3
<i>L-N</i>	312.9	304	2.84	51.3	66.4	29.4	312	304	2.6	51.6	66.4	28.7
<i>L-SF</i>	352.0	348.7	0.9	42.8	13.1	69.4	355	329	7.3	48.1	47.6	1

- Shear Critic Beams: Experimental study, the table below lists the obtained experimental and numerical (ABAQUS) data. P_{cr} , P_{yield} , Δ_{cr} , and Δ_{yield} standing for the cracking, yielding load and their corresponding deflection values.

	$P_{cr} (kN)$			$\Delta_{cr} (mm)$			$P_{yield} (kN)$			$\Delta_{yield} (mm)$		
	<i>Exp.</i>	<i>Num.</i>	<i>Error (%)</i>	<i>Exp.</i>	<i>Num.</i>	<i>Error (%)</i>	<i>Exp.</i>	<i>Num.</i>	<i>Error (%)</i>	<i>Exp.</i>	<i>Num.</i>	<i>Error (%)</i>
<i>B1</i>	31.1	35.1	12.9	0.9	0.7	22.2	125.2	127.4	1.8	8.5	8.6	1.2
<i>B2</i>	35.6	25.5	28.4	0.9	0.7	22.2	138.9	142.9	2.9	7.5	7.8	4
<i>B3</i>	31.2	46.7	49.7	0.7	1	42.9	141.3	145.1	2.7	7.4	7.8	5.4
<i>B4</i>	33.9	23.4	31	0.8	0.5	37.5	138	142.7	3.4	7.4	7.4	0

- Shear Critic Beams: Experimental study, the table below lists the obtained experimental and numerical (ABAQUS) data. P_p , P_{ult} , Δ_p , and Δ_{ult} standing for the peak, ultimate load, and their corresponding deflection values.

	$P_p (kN)$			$\Delta_p (mm)$			$P_{ult} (kN)$			$\Delta_{ult} (mm)$		
	<i>Exp.</i>	<i>Num.</i>	<i>Error (%)</i>	<i>Exp.</i>	<i>Num.</i>	<i>Error (%)</i>	<i>Exp.</i>	<i>Num.</i>	<i>Error (%)</i>	<i>Exp.</i>	<i>Num.</i>	<i>Error (%)</i>
<i>B1</i>	137.6	136	1.2	38.6	35.8	7.3	-	132.2	-	-	14.7	-
<i>B2</i>	148.9	154.7	3.9	47.3	48.5	2.5	-	148.2	-	-	19.5	-
<i>B3</i>	149.5	161.6	8.1	44.6	49.8	11.7	-	153.1	-	-	19.2	-
<i>B4</i>	151	150.6	0.3	47.3	42	11.2	-	148.3	-	-	20.7	-

- Shear Critic Beams: Experimental study, the table below lists the obtained experimental and numerical (VecTor2) data. P_{cr} , P_{yield} , Δ_{cr} , and Δ_{yield} standing for the cracking, yielding load and their corresponding deflection values.

	P_{cr} (kN)			Δ_{cr} (mm)			P_{yield} (kN)			Δ_{yield} (mm)		
	Exp.	Num.	Error (%)	Exp.	Num.	Error (%)	Exp.	Num.	Error (%)	Exp.	Num.	Error (%)
<i>B1</i>	31.1	35	11.1	0.9	0.69	23.3	125.2	136.8	9.3	8.5	6.7	21.2
<i>B2</i>	35.6	36.2	1.7	0.9	0.79	12.2	138.9	143.7	3.5	7.5	7.2	4
<i>B3</i>	31.2	37.6	20.5	0.7	0.79	12.8	141.3	145	2.6	7.4	6.9	6.8
<i>B4</i>	33.9	35.6	5	0.8	0.69	13.8	138	141.7	2.7	7.4	6.9	6.8

- Shear Critic Beams: Experimental study, the table below lists the obtained experimental and numerical (VecTor2) data. P_p , P_{ult} , Δ_p , and Δ_{ult} standing for the peak, ultimate load, and their corresponding deflection values.

	P_p (kN)			Δ_p (mm)			P_{ult} (kN)			Δ_{ult} (mm)		
	Exp.	Num.	Error (%)	Exp.	Num.	Error (%)	Exp.	Num.	Error (%)	Exp.	Num.	Error (%)
<i>B1</i>	137.6	165.2	20.1	38.6	31.2	19.2	-	164.8	-	-	31.4	-
<i>B2</i>	148.9	165	10.8	47.3	26.7	43.6	-	160.2	-	-	35	-
<i>B3</i>	149.5	170.7	14.2	44.6	27.7	37.9	-	161.6	-	-	38	-
<i>B4</i>	151	162.4	7.5	47.3	22.5	52.4	-	145.8	-	-	25.9	-

Appendix B

Technical Specification of Data Acquisition Device and Instrumentations

A.1 Data Acquisition Device

➤ Trademark - Model: Teknik Destek Grubu (TDG) - Test Box-1001

Technical Specifications

CHANNELS		INPUT / OUTPUT INTERFACES	
Number of Channels	8 per Device (Chassis)	Channel Inputs	DSUB9 Female
Extention	Up to 64 Channels (per Gateway)	Power Input and Chain	C14 Connector (IEC Power Cable, Computer Type)
Input Range	±10 V	Inter Connection (RS485)	2 x DSUB9 Male
Input Type	Differential	Gateway Communication	USB B Type (Printer Cable)
Gain Selection	Independent Adjustable Gain for Each Channel 8 levels from x1 to x890	Gateway Power	DC Jack
		Display	7-Segment Address Display
DIGITIZATION		PHYSICAL & ENVIRONMENTAL	
ADC	16 Bit, Delta-Sigma Oversampling	Dimensions	288 x 103 x 160 mm
Sampling Rate	8 Örnek / Saniye (Kanal Başına)	Operating Temperature	-20 C° ... + 60 C°
Sampling Type	Multiplexing	Storage Temperature	-30 C° ... + 80 C°
Dynamic Rate	< 72 dB	Enclosure	Aluminium, Laboratory Type
Filtering	Analog Anti-Aliasing Low Pass Filter		
COMMUNICATION		ACCESSORIES	
Devices and Gateway	RS485	TESTBOX Bridge	Gateway for Computer Connection (1 Gateway is Included Free of Charge To Be Used With Up To 8 Devices)
Connection to Computer	USB via Gateway	TESTBOX Q-Cable	120, 350 Ohm Quarter/Half Bridge Completion Cable
SENSOR COMPATIBILITY		TESTBOX RTD Cable	For Connection PT100 sensors
Compatible Sensor Types	Position Transducers (Potentiometric, DC Type, Strain Based) Load Cell LVDT (DC Type) Voltage Output Sensors Full Bridge Strain Based Sensors Strain Gauge (via Q-Cable) Thermocouple (via TC Connection Box) RTD (via RTD Cable)	Thermocouple	Connector Box for Multiple Thermocouple Inputs with Cold Junction Compensation Sensor
Sensor Excitation (Supply) Options	5 VDC, 10 V DC (Independently Adjustable via Switch For Each Channel)	CERTIFICATION	
POWER		CE	LVD (2014/35/EU) EMC (2014/30/EU)
Power Input	220 V AC - 50 Hz	Local	Home (Inland) Produce Certification
Power Consumption	10W Max.	Calibration	TDG Calibration Lab. Factory Calibration
Gateway	9V DC 500 mA Adapter	SOFTWARE	
		TDG Software	EASYTEST BASIC



Teknik Destek Grubu Bilimsel Ölçme Ltd. Şti.
ODTÜ Teknokent Bilişim İnovasyon Merkezi
Mustafa Kemal Mah. Dumlupınar Bul. 280G B-Blok
D:214 Çankaya/Ankara/TURKEY
P : +90 312 473 97 91-92
info@tdg.com.tr
www.tdg.com.tr

A.2 Uniaxial Strain Gauge

- Trademark - Model: Teknik Destek Grubu (TDG) - BF120 -10AA

DEPLASMAN
POZİSYON
SENSÖRLERİ

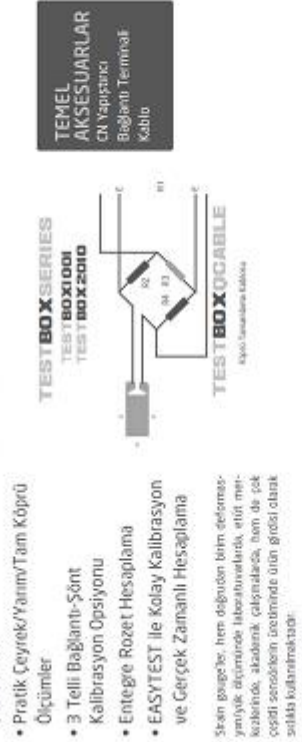
YÜK HÜCRELERİ
LOAD CELLS

STRAIN GAUGES

Geniş seçenekler ve ayrıntılı bilgiler için:
www.testart.com.tr
Türkiye'nin Sensör ve Test Portalı

STRAIN GAUGES BİRİM DEFORMASYON ÖLÇERLER

- Yüksek Performans-Maliyet
- TESTBOX Serisi Veri Toplama Sistemleri ile Uyumluluk
- 16-24 Bit Statik/Dinamik Ölçümler
- Uygun Maliyetli İnovatif Q-Cable Çözümü ile
- Pratik Çeyrek/Yarı/Tam Köprü Ölçümler
- 3 Telli Bağlantı-Sönt Kalibrasyon Opsiyonu
- Entegre Rozet Hesaplama
- EASYTEST ile Kolay Kalibrasyon ve Gerçek Zamanlı Hesaplama



Strain gaugeler, her ölçümün temel deformasyonlu ölçümünde laboratuvarlarda, elifi mer-kulilerinde, alüminyum çubuklarda, tam da çekme testi serilerinin ölçümünde olan geniş otomatik kullanılmaktadır.

Temel yapıya genişletilebilir olarak, dairesel, üçgen, dörtgen, yarıdaire, boy değişiminin elektrikli bir sinyal olarak algılanmasını sağlar. Aşağıdaki strain gaugeler temel olarak üçe ayrılabilir: dirençli, Gerilim (200 ve 3500)lik modelle, dirençli bu basitçe dirençler olarak bir kural olan direnç boyu değişimi olarak diğer değeri tanımlanır.

	BF-120-10AA	BF-120-309A	BF-120-60A
Ölçüm/Çift Boyutu (mm)	10x2.5	30x2.0	6x2.2
Taban Boyutu (mm)	16,7x5,0	36,1x5,0	12,5x4,3
Direnç (Ω)	120	120	120
Yüksek Gauge Faktörü	2	2	2
Strain Limit	%3	%3	%3
Fağ Ölmesi (Genim)	105	105	105
Çalışma Sıcaklığı (°C)	-20 ~ +80	-20 ~ +80	-20 ~ +80

1328. Sokak 5/6 Akşahi Ouedler 06460 Çankaya / Ankara / TÜRKİYE
Tel: +90 312 473 97 91-92 - Faks: +90 312 473 97 93
Info@teknikdestek.com.tr - www.teknikdestek.com.tr

CE, TÜRKİYE, ISO 9001, ISO 14001

A.3 Linear position transducer (LPT)

➤ Trademark - Model: Opkon – RTL 200 D 5K

RTL

Lineer Potansiyometre

OPKON
Sense the motion

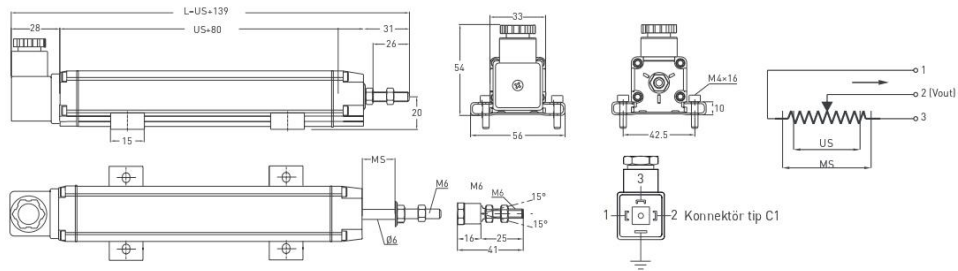
- 30 - 1000 mm ölçme boyu
- Yağ tahliye kanalları
- Özel teflon yatak sistemi
- $\pm 0,05$ linearite
- 5 kOhm : 30 - 600 mm
10 kOhm : 650 - 1000 mm



Teknik Özellikler

Ölçme boyu	30 - 1000 mm
Linearite	$\pm 0,05$ (>200 mm), $\pm 0,1$ (130-200mm), $\pm 0,2$ (75-129 mm), $\pm 0,5$ (<75 mm)
Tekrarlanabilirlik	< 0.01 mm
Çözünürlük	Sonsuz
Direnç	5 kOhm : 30 - 600 mm 10 kOhm : 650 - 1000 mm
Direnç toleransı	± 20
Yük direnci	100 kOhm min
Tavsiye edilen kontak akımı	< 1 μ A
Besleme voltajı	28 VDC maks.
Elektriksel bağlantı	4 kutuplu hidrolik tip konektör
Hız	< 5 m/s
Titreşim	EN 60068 - 2 - 6 5 - 2000 Hz 200 m/s ² (20g) 2s 30dk her eksen (x,y,z)
Şok	EN 60068-2-2:2007 500 m/s ² (50g) 11 ms. (x,y,z eksen)
Mekanik ömür	100 milyon hareket
Gövde ölçüleri	33 mm x 33 mm
Gövde malzemesi	Eloksallı alüminyum
Mil malzemesi	Paslanmaz çelik
Mil çapı	$\varnothing 6$ mm
Mekanik sabitleme	Hareketli ayaklar
IP koruma sınıfı	IP 65 - EN 60529
Çalışma sıcaklığı	-20°C ... +80°C
Saklama sıcaklığı	-30°C ... +90°C

Mekanik Özellikler



RTL (mm)	30	50	75	100	125	130	150	175	200	225	250	275	300	325	350	375	400	450	500	550	600	650	700	750	800	850	900	1000
US (Ölçme boyu)	30	50	75	100	125	130	150	175	200	225	250	275	300	325	350	375	400	450	500	550	600	650	700	750	800	850	900	1000
M5±0,5 (Mekanik boy)	34	54	79	104	129	134	154	179	204	229	254	279	304	329	354	379	404	454	504	554	604	654	704	754	804	854	904	1004
L (Toplam boy)	169	189	214	239	264	269	289	314	339	364	389	414	439	464	489	514	539	589	639	689	739	789	839	889	939	989	1039	1139

Sipariş Prosedürü

Model	Ölçme boyu (mm)	Linearite (%)	Direnç (kOhm)	Konnektör
RTL	500	D	5K	C1
RTL	30 - 1000 mm	A: $\pm 0,5$ (<75 mm), B: $\pm 0,2$ (75 - 129 mm), C: $\pm 0,1$ (130 - 200 mm), D: $\pm 0,05$ (>200 mm)	5K : 5 kOhm (30-600mm) 10K : 10 kOhm (650-1000mm)	C1 : 4 pinli konektör C5 : Konektör

Yukarıda verilen teknik datalar sadece bilgi amaçlıdır. OPKON haber vermeden her türlü değişiklik yapma hakkına sahiptir.

DS-RTL TR 15.05.2018

A.4 Load-cell

- Trademark - Model: Keli Sensing Technology - LFSCE-A



www.ttmteknoloji.com.tr

TTM

TEKNOLOJİ TASARIM MERKEZİ

Bilgisayar Yazılım Nakliyecilik Makine ve Kalıp Tic. Ltd. Şti.

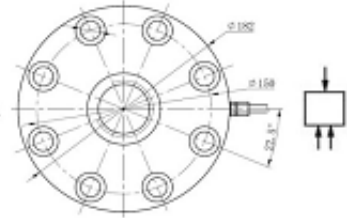
Keykubat Mah. Yarma Sok No: 17/A Karatay/KONYA

Tel: +90.332.3538491 - Fax: +90.332.3534303 - ttm@ttmteknoloji.com.tr

KELI LOAD CELL

Model: **LFSCE-A Load Cell**

Test makineleri, deneysel uygulamalar, aks baskül/kantarları
Test machines, experimental machines, axle-load scales etc.



LFSCE-A (20, 30 Ton)

TEKNİK ÖZELLİKLER TECHNICAL PARAMETERS		EXC + (Kırmızı, Red) EXC - (Siyah, Black)	SIG + (Yeşil, Green) SIG - (Beyaz, White)
Kapasite Rated capacities (Emax)	20, 30 Ton	Sıcaklık (Kompanse) Temperature range, compensated	-10°C ~ +40°C
Hassasiyet Sensitivity	3,0 ± 0,006 mv/V	Çalışma Sıcaklığı Temperature range, operating	-30°C ~ +70°C
Creep Error (30 min.) Total Error	± 0,05 %F.S. ± 0,3 %F.S	Maksimum Güvenli Yükleme Maximum safe overload	120 %F.S.
Sıfır Dengesi Zero Balance	± 1%F.S.	Doğru Tartım Limiti Ultimate overload	150 %F.S.
TCO (Temp. Effect on Min. Dead Load Output)	± 0,05 %F.S./10°C	Tavsiye Edilen Akım Excitation, recommend	10 ~ 12 VDC
TC SPAN (Temperature Effect on Sensitivity)	± 0,05 %F.S./10°C	Maksimum Akım Excitation, maximum	15 VDC
Giriş Direnci Input Impedance	760 ± 10 Ω	Koruma Sınıfı Protection Class	IP67
Çıkış Direnci Output Impedance	703 ± 2 Ω	Gövde Malzemesi Construction	Alloy Steel (A430 Çeliği)
İzolasyon Direnci Insulation Impedance	≥ 5000 MΩ	Kablo Çapı Cable Diameter: 6 mm	Kablo Uzunluğu Cable Length: 6 m.



www.ttmteknoloji.com.tr

TTM

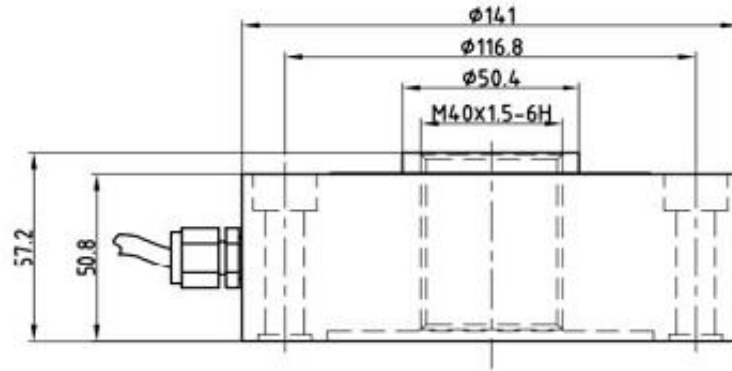
TEKNOLOJİ TASARIM MERKEZİ

Bilgisayar Yazılım Nakliyecilik Makine ve Kalıp Tic. Ltd. Şti.

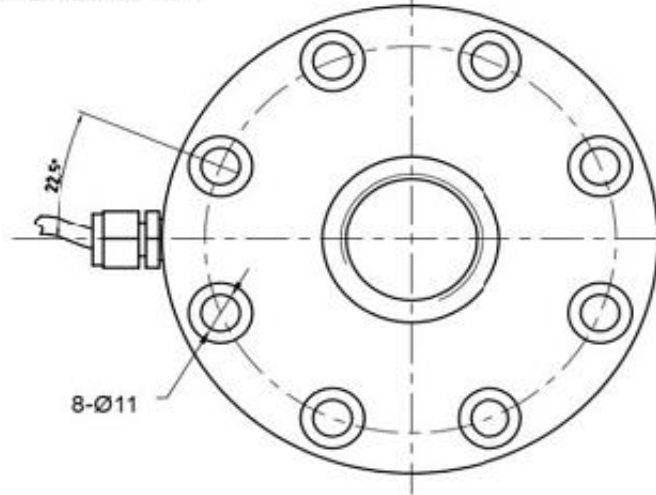
Keykubat Mah. Yarma Sok. No: 17/A Karatay/KONYA

Tel: +90.332.3538491 - Fax: +90.332.3534303 - ttm@ttmteknoloji.com.tr

Model: **LFSCE-A Load Cell**



LFSCE-A 20~30 TON



Appendix C

Reinforcement Preparation, Concrete Pouring and Material Testing Photos from the Conducted Experimental Study



Figure C.1 Steel reinforcements



Figure C.2 Reinforcements placed into the prismatic molds, before concrete pouring



Figure C.3 The beams after concrete pouring



Figure C.4 The beam specimens after removing the formworks and ready for testing



Figure C.5 Compression test of 150 mm x 150 mm x 150 mm standard cube sample



Figure C.6 Split tensile test of cylinder concrete sample having 100 mm diameter and 200 mm height

Curriculum Vitae

Name Surname : Marwan AL SAMAN

Date of Birth : 06/03/1994

Education:

- B.Sc. 2018, Civil Engineering, International University of Science and Technology
- M.Sc. 2023, Civil Engineering, İzmir Katip Çelebi University

Conference Papers:

- AL SAMAN, M. and ÇANKAYA, M. A. (2023, May 12-13). Plasticity Based Nonlinear Finite Element Analysis of Steel Fiber Reinforced Concrete Beams. 7th International Students Science Congress, İzmir, Türkiye.